Faculty of Physics and Astronomy
University of Heidelberg

Diploma Thesis

in Physics

submitted by

Frederik Matthias Spiegelhalder

born in Heidelberg,

August 2005.

Setting up a Lithium Magneto-Optical Trap as a Target for a Reaction Microscope

This diploma thesis has been carried out by
Frederik Matthias Spiegelhalder
at the
Max-Planck-Institut für Kernphysik, Heidelberg
under the supervision of
Prof. Joachim Ullrich
and Priv.-Doz. Dr. Alexander Dorn.

Für Eileen

Daß ich erkenne, was die Welt
Im Innersten zusammenhält

Johann Wolfgang von Goethe, Faust I

Zusammenfassung

Die vorliegende Diplomarbeit ist Teil eines größeren Projekts am Max-Planck-Institut für Kernphysik, bei dem erstmals magnetooptisch gefangene Atome als Target für ein Streuexperiment in einem Reaktionsmikroskop integriert werden sollen, um damit mehrere Reaktionsprodukte mit höchster Auflösung nachweisen zu können. Im Rahmen dieser Arbeit wurde dazu die magnetooptische Falle für Lithiumatome einschließlich des dazugehörigen Diodenlasersystems aufgebaut. Die Falle wurde zunächst unter Verwendung eines Farbstofflasers in Betrieb genommen und charakterisiert. Geladen aus dem Hintergrundgas, das mittels eines Dispensers mit Lithium angereichert wurde, konnten einige 10^6 Atome bei einer Dichte von etwa 10^9 Atomen/cm^3 bei Ladezeiten von wenigen Sekunden gespeichert werden. Zusätzlich ist eine Atomstrahlquelle mit Zeeman-Abbremser entworfen und aufgebaut worden, mittels derer höhere Atomzahlen und insbesondere kürzere Ladezeiten erreicht werden sollen. Diese Apparatur konnte allerdings noch nicht in Betrieb genommen werden. Um den gepulsten Betrieb der Falle, wie er für spätere Experimente erforderlich sein wird zu testen, wurden die Laserstrahlen schnell aus- und eingeschaltet und das Verhalten der gefangenen Atome untersucht. Dabei zeigte es sich, daß Abschaltzeiten von 1–2 ms mit 1000 Wiederholungen bei akzeptablen Verlustraten von bis zu 20 Prozent realisierbar sind, womit das Reaktionsmikroskop problemlos zu betreiben sein sollte.

Abstract

The present work is part of a larger project at the Max-Planck-Institut für Kernphysik that will use magneto-optically trapped atoms as a target in a reaction microscope to facilitate high precision scattering experiments. For this purpose, a lithium MOT and a diode laser system was designed and brought into operation within this thesis. The trap was tested and characterised using a dye-laser. Loaded from thermal background gas provided by a lithium dispenser, atom numbers of a few 10^6 at a density of about 10^9 atoms/cm^3 were achieved with loading times of a few seconds. In addition, for more efficient loading of the trap, a Zeeman slower was designed, simulated and assembled. Using the slow and cold atomic beam, faster loading rates and thus higher atom numbers and trap densities are expected, but not yet tested. In order to simulate the pulsed operation of the trap necessary for later experiments, the trapping laser beams were switched off and on very fast. Off times of up to 1–2 ms were found to be possible without loosing a significant fraction (less than 20 percent) of atoms even after 1000 cycles, demonstrating operation conditions well suited for the reaction microscope.

Table of Contents

Preface

Today's concept of the atomic structure has evolved through experiments as performed in 1909 by Hans Geiger and Ernest Marsden in Ernest Rutherford's laboratory and from theories in the early 20th century. The accumulated knowledge was contained in theoretical models such as the Bohr model of the atom which could predict certain experimental observations. Driven by increasing precision, the theoretical models were continuously improved. This development culminated in the most successful physical theory of today, namely quantum electrodynamics (QED) which emerged from quantum mechanics (Schrödinger equation) and relativistic quantum mechanics (Dirac equation).

While time-independent atomic structure, such as the electron binding energy or the g-factor, can be calculated with high precision, it is still very difficult to make predictions about dynamic, time-dependent processes which go beyond simple two-body reactions. Although the principles of the underlying interactions are known precisely, complex processes still cannot be described satisfactorily. Accordingly, one of the most fundamental reactions, namely single ionisation of hydrogen by impact of low energetic electrons, the dynamical three-particle quantum problem, was just recently claimed to be "solved" in a mathematical consistent way using supercomputers [Weh99], [Res99]. Not before 2003 ([Bra96], [Bra02], [Kad03]) were these numerical results proven to be accurate by formulating the correct ionisation amplitude unambiguously.

In spite of still unanswered questions concerning the single ionisation of helium with two active electrons, the emphasis of modern research is shifting to even more complicated atomic reactions such as double ionisation, multi-photon processes or capture reactions.

New technological developments, the reaction microscope being one such example, allow to perform kinematically complete experiments, probing the whole many-particle final state simultaneously for all relative angles and energies of the reaction partners. This is achieved by extracting the produced electrons and ions from the reaction volume with the help of electric and magnetic fields onto position sensitive detectors. From the time-of-flight information and the position on the detector, all energies and momenta can be determined as described in Section 1.2. Thus far, reaction microscopes are essentially solely used with gaseous targets realised by supersonic expansion in an atomic jet. As a new development, targets made up of magneto-optically trapped atoms

(MOT) were combined with recoil-ion momentum spectrometers as described by [Fle01], [Poe01], [Tur01], [Kno03] and [Bre03]. However, these experiments can only measure the recoiling ions and have not implement electron spectrometers. For kinematically complete measurements it is necessary to determine the momenta of all reaction partners in the final state. Thus, the presented set-up is the first one, where a MOT-target is aimed to be used to perform kinematically complete measurements.

The scope of this thesis was to set up a lithium magneto-optical trap as a target for a new reaction microscope that will allow the study of fully differential cross sections (FDCS) for single, double and triple ionisation of lithium by using a variety of possible projectiles such as electrons, protons, heavy ions, short laser pulses as well as energetic photons from synchrotron sources or from the future free-electron laser (the FEL at DESY, Hamburg for example). The experiments that will be possible with this new machine will close the gap between the measurements which are done with the simplest atomic systems (hydrogen and helium) and the more complex targets (i.e. argon, neon, xenon). Related to the MOT-target are many specific problems that have to be overcome, such as the incompatibility of the magnetic field from the MOT with the one used in the spectrometer. Therefore, the target has to be operated in a pulsed mode, meaning that the magnetic field of the MOT has to be switched off and on very quickly for data acquisition [Sch96]. To simulate the behaviour of the trapped atoms in a pulsed trap the trapping lasers were switched off and on and the fraction of atoms remaining in the trap was measured. Other important parameters such as atom number and target density were also measured in order to characterise the MOT as a possible target for collision experiments.

A detailed discussion of the set-up is provided in Section 1.3. Chapter 1 also gives an introduction to the reaction microscope and some facts and figures about lithium. A short theoretical introduction to the field of laser cooling and trapping relevant for this work, including the spontaneous light force and the optical dipole force is given in Chapter 2. In the following chapters the experimental set-up is presented. The vacuum chamber is explained in Chapter 3. Chapter 4 contains the description of the diode laser system and the dye-laser which were set up for the magneto-optical trap. In Chapter 5 the design and set-up of the Zeeman slower are presented. Some theoretical aspects of the atomic beam which will be used to load the MOT are described in Chapter 6. The results of the measurements on the MOT, characterising it as a target for a reaction microscope are provided in Chapter 7.

Chapter 1

Introduction

In this chapter some fundamental principles, ideas and properties of the presented experiment will be discussed. First, some characteristic data of the atom under study, namely lithium is provided. A short general introduction to electron and ion spectrometers as well as a description of the reaction microscope is given in Section 1.2. The planned set-up is introduced in Section 1.3.

1.1 Lithium

Lithium (from Greek λίθος, stone) was discovered by Johann Arfvedson in 1817. He found the new element within the minerals spodumene and lepidolite in a petalite ore, $LiAl(Si_2O_5)_2$, he was analysing from the island Utö in Sweden. In 1818 Christian Gmelin was the first to observe that lithium salts give a bright red colour in a flame. Both scientists tried and failed to isolate the element from its salts, however. The element was not isolated until W.T. Brande and Sir Humphrey Davy later used electrolysis on lithium oxide. Commercial production of lithium metal was achieved in 1923 by the German company Metallgesellschaft AG by using electrolysis of molten lithium chloride and potassium chloride.

Lithium is widely distributed but does not occur in nature in its free form. Because of its reactivity, it is always found bound with one or more other elements or compounds. It forms a minor part of almost all igneous rocks and is also found in many natural brines. Lithium is the third element in the periodic table and belongs to the alkali metals. It has one relatively loosely bound valence electron (Table 1.1) which it can give away to reach He configuration. It reacts with water, but not as vigorously as Na. When exposed to air it forms Li_2O and Li_3N.

Lithium is the lightest of all metals with a density only about half of that of water. There are two stable isotopes which are found in nature. Their natural abundances

are 7.59 % for fermionic ^{6}Li and 92.41 % for bosonic ^{7}Li. Since ^{6}Li and ^{7}Li have different atomic transitions and require slightly different laser frequencies, only the bosonic species is used in the presented experiment due to its higher abundance. ^{7}Li is one of the primordial elements produced in big bang nucleosynthesis.

Some fundamental physical properties of bulk lithium are listed in Table 1.1. The vapour pressure of lithium in the liquid phase is given by Equation 6.1 in Section 6.2. Important for this work are mainly the properties of atomic lithium. Some of these are listed in Table 1.2.

Table 1.1: Fundamental physical properties of bulk lithium

Property	**Symbol**	**Value**	**Unit**
Density (300 K)	ρ	0.534	g cm^{-3}
Melting point	T_m	453.69	K
Boiling point	T_b	1615	K
Heat of fusion	Q_f	2.99	kJ mol^{-1}
Heat of vaporisation	Q_v	134.7	kJ mol^{-1}
Atomic mass number	A	6.941	
Abundance on earth		20	ppm
1st ionisation potential		5.392	eV
2nd ionisation potential		76.638	eV
3rd ionisation potential		122.451	eV
Price		100	€/kg

Table 1.2: Fundamental atomic and properties of ^{7}Li

Property	**Symbol**	**Value**
Atomic number	Z	3
Neutron number	N	4
Nucleon number	$Z+N$	7
Nuclear spin	I	3/2
Relative atomic mass		7.016

The spectroscopic data of the optically allowed dipole $2^2S_{1/2} - 2^2P_{3/2}$ (D2) transition used for laser cooling together with the limiting values for velocity and temperature at the capture, Doppler and recoil limit, respectively are given in Table 1.3.

1.2 The Reaction Microscope

The dynamics of many-body quantum systems can be investigated inter alia in kinematically complete experiments as performed with various set-ups at the Max-Planck-Institut für Kernphysik (MPI-K) in Heidelberg. Here, atoms are ionised and the momenta

Table 1.3: Optical properties of the ^{7}Li D2 transition used for laser cooling [Met99]

Property	**Symbol**	**Value**	**Unit**
Wavelength	λ	670.962	nm
Wavenumber	$k/2\pi$	14 903.4	cm^{-1}
Frequency	ν	446.765	THz
Transition energy	$\hbar\omega_a$	1.848	eV
Lifetime	τ	26.87	ns
Natural linewidth	Γ	5.92	2π MHz
Saturation intensity	I_s	2.56	mW cm^{-1}
Capture velocity	v_c	3.97	m s^{-1}
Capture temperature	T_c	13.33	mK
Doppler velocity	v_D	41.04	cm s^{-1}
Doppler temperature	T_D	142.11	µK
Recoil velocity	v_r	8.474	cm s^{-1}
Recoil temperature	T_r	6.061	µK

of the fragments are measured using the so-called reaction microscope [Mos96]. In order to compare the results with theory, very simple systems are necessary. Therefore, first single and double ionisation experiments were performed with hydrogen and helium, being the simplest atoms available. In this section, the important concepts of recoil-ion momentum spectroscopy as well as of imaging electron-momentum spectrometers are discussed briefly and the working principle of the reaction microscope is presented.

The rapid and still ongoing development of **R**ecoil-**I**on **M**omentum **S**pectroscopy, RIMS, during the last decade can undoubtedly be viewed as an experimental breakthrough for the investigation of any kind of atomic reaction dynamics [Ull03]. State-of-the-art high-resolution recoil-ion momentum spectrometers evolved through numerous technical developments including the implementation of cold supersonic jet targets, the use of well defined electric extraction fields for recoil-ions as well as for electrons and the rapid progress in charged particle detection techniques. The most important ingredient among them being the use of supersonic jets to produce well localised and internally cold targets (**CO**ld **T**arget **R**ecoil-**I**on **M**omentum **S**pectroscopy, COLTRIMS). Thus, a recoil-ion momentum resolution far below 1 a.u.[1] is achieved, which would be impossible with room-temperature targets due to the thermal motion. Another decisive development was the invention of completely novel and extremely efficient electron imaging concepts. In combination with COLTRIMS they enabled the detection of recoil-ions and electrons in coincidence and opened up a whole area of kinematically complete atomic reaction studies.

[1] One atomic unit in momentum is the mean translational momentum of an electron bound in the ground state of a hydrogen atom, see Appendix B.

1.2.1 Ion Spectrometers

A recoil-ion spectrometer is a high precision device designed to measure recoil-momenta of ions corresponding to kinetic energies on the order of a few meV with μeV resolution. In general, the recoil-momentum range of interest depends on the reaction channel to be studied. From most atomic reactions the created target ions emerge with typical momenta of 1 a.u. or below.

In order to measure the magnitude and the direction of the recoil-ion momentum vector, an experimental arrangement is needed which performs an unambiguous mapping of these quantities onto experimentally accessible observables. The simplest device to fulfil the requirements of sufficient momentum resolution and large angular and momentum acceptance would be a position sensitive detector placed at some distance in a field free environment viewing the point like reaction volume. Then, simply from the position and time-of-flight (TOF) information of each detected ion, the trajectory can be reconstructed and the initial momentum vector can be calculated. The TOF has to be measured with respect to a trigger signal which uniquely defines the time of interaction of a projectile with a single target atom. To do so a pulsed beam of projectiles (synchrotron radiation, pulsed lasers, bunched electron or ion beams) has to be used. However, this simple TOF technique has some unacceptable drawbacks. The recoil-ion angular acceptance is limited and no direct information about the ionic charge is obtained. Moreover, flight times of very low-energy recoiling ions would be unacceptably long and ions close to zero momentum would not be detectable at all. Electric fringe fields in the mV and μV regime that are hardly avoidable would strongly disturb the low-energy ion trajectories. All of these difficulties are circumvented by applying a constant and weak, in most cases homogeneous electric field (extraction field) to push the ions (and the electrons) toward the detector. Among others, a very important advantage of field extraction is that the TOF yields information not only about the ion momentum but, in addition, it allows to determine the ion species because the TOF depends also on the ratio of ion mass over charge. Furthermore, the TOF becomes reasonably short — typically up to some 10 μs, and fringe fields are of minor importance such that neV resolution has become achievable.

In conclusion, a standard RIMS-spectrometer consists of a region with a homogeneous electric extraction field where recoil-ions emerging from an ideal point like source volume are accelerated. Afterwards, they pass a field-free drift region before they are detected by means of a position sensitive ion detector. The field-free drift region compensates the time jitter which arises from finite sized target extension along the extraction direction. This so called time-focussing geometry for spectrometers with one acceleration and one drift region is discussed in [Wil55].

All three components of the recoil-ion momentum vector are determined by a coincident measurement of the two position coordinates and the TOF for each ion. The longitudinal momentum of the recoil-ion (along the electric field axis) is directly related

to its time-of-flight. The two missing components perpendicular to the field vector can be determined from the position of impact on the ion detector. The achievable momentum resolution at a given momentum acceptance depends on the position resolution of the detector and, for more realistic situations, on the extension of the overlap region of the projectile and the target beams. In many situations the latter is dominating. Ultimately, the temperature of the atoms in the target limits the reachable momentum resolution.

1.2.2 Target Preparation

A prerequisite for high resolution recoil-ion momentum spectrometry is a cold atomic or molecular gas-target because in many cases, depending on the physical process to be studied, the recoil-ion momenta are on the order of or even smaller than the thermal momentum spread at room temperature (for example He: 1 a.u. = 2 meV, $\bar{E}(T$ = 300 K) = 25 meV). Moreover, a small target size is indispensable for momentum spectroscopy with imaging spectrometers. In almost all existing devices both requirements are realised with supersonic expansion of the target gas to form a well localised cold atomic beam.

Supersonic Jets

When a gas is pressed through a small nozzle into a reservoir at low pressure it is accelerated to supersonic speed at the exit of the nozzle and an atomic beam is formed as long as the pressure ratio P_0/P_1 (see Figure 1.1) is larger than about two [Sco88]. During this adiabatic expansion, the free enthalpy $H = 5/2k_BT_0$ (with the Boltzmann constant k_B and initial gas temperature T_0) of an ideal gas is converted into a directed motion at the expense of the internal temperature, thus, achieving cold atomic beams with temperatures on the order of a few hundred mK. Rare gases like helium and argon can easily be prepared in a supersonic jet and are used in a number of experiments (for example [Dor01a]).

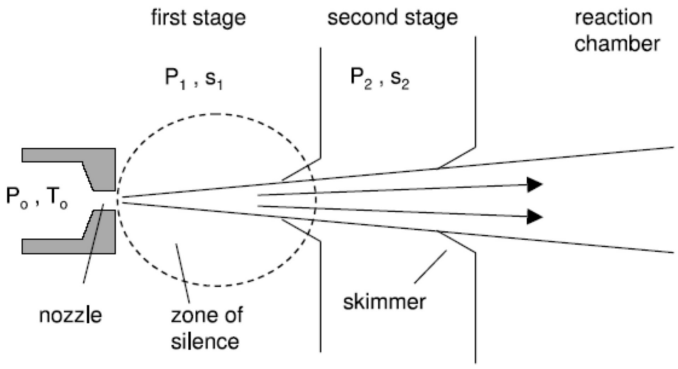

Figure 1.1: Illustration of a two-stage supersonic gas jet taken from [Ull03].

One or several stages with differential pumping are used to handle the enormous gas-load and to maintain a good vacuum in the reaction chamber. In order to extract a geometrically well defined supersonic beam, a small *skimmer* aperture is placed behind the nozzle and between the different pumping stages. A schematic representation of a two-stage supersonic gas jet with pumping speeds s_0 and s_1 is shown in Figure 1.1. At the nozzle exit a zone of supersonic flow bordered by a compression or shock-front is formed. A high quality gas-jet can be cut out if the edge of the skimmer immerses into this so-called *zone of silence*.

For most applications a dense and narrow atomic beam is required, which is crossed with a projectile beam in the interaction chamber. Without too much effort, supersonic gas beams with a particle density on the order of 10^{11} to 10^{12} cm^{-3} at a distance of about 10 cm away from the nozzle are reachable. It is obvious, that this number decreases with the inverse square of the distance between nozzle and interaction zone.

Atomic Traps (MOTRIMS)

A further significant reduction of the target temperature is achievable when laser-cooled atoms trapped in a magneto-optical trap (MOT) are used as a target. In the first pioneering experiment, Wolf and Helm [Wol00] have measured recoil-ion energies of photoionised Rb atoms extracted from a MOT with very high resolution. Basically, the same method has been used very recently (for example [Poe01] and [Tur01]) to study single electron capture reactions in keV ion collisions with atoms trapped in a MOT. In such experimental set-ups an unprecedented resolution in the recoil-ion momentum can been achieved by taking benefit of the sub-mK intrinsic temperature of the target. For recoiling Rb^+ ions produced in capture reactions with keV Cs^+ projectiles Flechard et al. [Fle01] have obtained a momentum resolution of Δp = 0.03 a.u., which means that the recoil-ion velocity has been measured with a sensitivity of below 1 m s^{-1}. Certainly, this value is not the ultimate resolution set by the gas cloud temperature of typically a few 100 µK which would correspond to a momentum resolution of Δp = 0.003 a.u. for lithium and Δp = 0.01 a.u. for rubidium.

With typical densities in the range of several 10^{10} cm^{-3} and radii of 1 mm or below, the atomic clouds trapped in MOTs are ideally suited as targets for RIMS (MOTRIMS) [Ngu04]. Whenever an ultimate momentum resolution is desirable like, e.g., in electron capture reactions where the recoil-ion momentum gives direct access to the electronic states populated in the projectile ion, a MOT target is superior to any gas jet. Another important aspect is that the palette of possible targets for RIMS is considerably widened. All alkali and alkaline earth atoms are easily trapped in a MOT, but they are hardly produced and cooled in a supersonic gas jet. These atoms are in some situations of particular interest because they represent single active electron targets and, therefore, have many features in common with atomic hydrogen, the simplest atomic target which is not directly accessible to COLTRIMS because efficient cooling methods are not at hand.

Besides, other interesting options are laser excited atoms and the possibility to probe the occupation of these excited states in a time-resolved manner via capture reactions monitored with RIMS [Kno03].

1.2.3 Electron Spectrometers

For ionisation processes the detection of the target ion only, does not yield sufficient information to characterise the reaction completely. For a reaction with n final state continuum particles, a kinematically complete experiment requires detection of (n-1) final state momentum vectors. The momentum of the remaining particle can be deduced using momentum conservation. Combined recoil-ion/electron momentum spectrometers have been developed within the last ten years which fulfil to a large extend these requirements and which enable kinematically complete studies of atomic collision reactions with up to five outgoing particles, e.g. triple ionisation of Ne in collisions with heavy ions [Sch00].

Particle imaging is done by accelerating electrons and ions in the same electric field into opposite directions onto two position sensitive detectors. Taking advantage of the fact that in particular the electron trajectories are easily modified by small magnetic fields, 4π solid angle acceptance is achieved. With proper combined electric and magnetic fields the motion is effectively confined in space. This way extremely versatile spectrometers have been constructed, the so-called reaction microscopes, allowing one to adjust the resolution and the acceptance in the electron and ion branch individually.

In this set-up a solenoidal magnetic field parallel to the electric field is superimposed [Mos94]. This magnetic field acts over the whole flight-path and forces electrons to move on spiral trajectories from the reaction volume to the detector. In practice the magnetic field is generated by a pair of large Helmholtz coils placed outside of the vacuum-chamber (Figure 1.2). Typical coil diameters range from 50 cm up to 2 m depending on the geometrical extension of the electron flight path. The set-up which is shown in Figure 1.2 basically consists of an electric extraction field with two subsequent drift paths and position sensitive detectors on either side. The extraction field is generated by means of potential rings in connection with a voltage divider or between two ceramic plates covered with a resistive layer [Mos96]. The target point is defined by the overlap of supersonic gas jet and particle beam.

Though the electron motion is more complicated due to the magnetic field, it is still possible to reconstruct both, the electron trajectory and initial momentum vector from the position information and the measured time-of-flight. For a homogeneous magnetic field parallel to the electric extraction field, the longitudinal motion (i.e. along the TOF-direction) of a charged particle is not changed. In the transverse direction (perpendicular to the field axis), however, the electrons travel along a circle with radius $R = p_\perp/(qB)$ where the time T for one turn is given by the inverse of the cyclotron frequency $\omega = q \cdot B/m = 2\pi/T$, with B being the magnetic field strength and m and q the electron mass

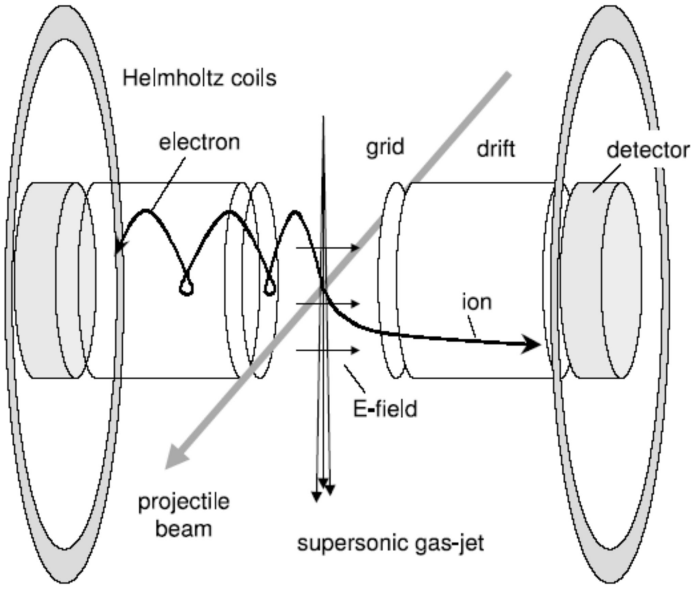

Figure 1.2: Schematics of a reaction microscope taken from [Ull03].

and charge, respectively.

1.3 Planned Set-Up

In this section the set-up planned to study ionisation processes with a target of magneto-optically trapped lithium atoms is presented. Lithium with three electrons is the next step to more complex target atoms after helium. It has a closed K-shell and one relatively loosely bound outer electron which makes it suitable to study a variety of ionisation processes. As a hydrogen-like system it can be used to compare single ionisation with the experiments done on hydrogen and determine the effects of the closed inner shell. Secondly, double ionisation with electrons coming from two different shells can be investigated and compared to the results obtained from the measurements on helium as done by [Dor01a] (for a detailed description of many-body quantum dynamics see [Ull03]). The ultimate goal however, would be to perform first measurements of the fully differential cross section (FDCS) for triple ionisation. For this purpose, the energies and momenta of all fragments (electrons and recoil-ion) will be recorded in coincidence. So far, only the total cross sections for single, double and triple ionisation of lithium by photon and electron impact have been measured (see Table 1.4).

The set-up which is presented here will use magneto-optically trapped lithium as a target for a reaction microscope (Figure 1.3). In contrast to rare gases like helium, lithium cannot be prepared as a supersonic gas jet. A thermal atomic beam would not allow sufficient ion momentum resolution because of its high thermal momentum

Table 1.4: Measured electron and photon impact double-to-single and triple-to-double ionisation ratios. [a] from [Hua03] [b] from [Weh98] for 3+/2+ and [Hua99] for 2+/1+

Process	$\sigma^{3+}/\sigma^{2+} \times 10^3$	$\sigma^{2+}/\sigma^{1+} \times 10^2$
Electron impact 1000 eV[a]	1.08 (0.85)	0.395(0.02)
Photon impact 424 eV[b]	1.8(0.6)	3.7(0.1)

spread. Yet, like all alkali metals Li can be conveniently laser cooled and trapped in a magneto-optical trap achieving a cold atomic cloud of up to 10^8–10^9 atoms at a Doppler temperature of 142 µK, thus, leading to an unequalled ion momentum resolution of $\Delta p \approx 0.003$ atomic units.

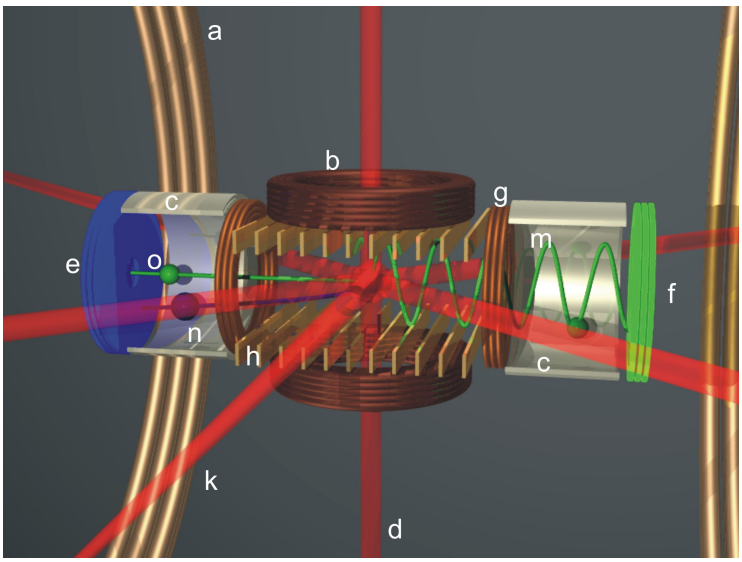

Figure 1.3: Schematic of experimental set-up. **a** Helmholtz coils (spectrometer), **b** MOT coils (intra-vacuum, water-cooled), **c** drift tubes, **d** trapping beams, **e** ion detector (MCP), **f** electron detector (MCP), **g** compensation coils, **h** extraction electrodes, **k** atomic beam, **m** electron trajectory, **n** ion trajectory, **o** projectile trajectory.

Both, the reaction microscope and the magneto-optical trap are standard tools in today's laboratories. To combine the two, several practical difficulties have to be overcome. As pointed out in [Sch96] the magnetic field of the trap (field gradient 10–20 G/cm) is not compatible with the homogeneous field ($B \approx 10$ G) required for imaging the charged fragments onto the detectors. Therefore, it is necessary to operate the lithium MOT in a pulsed mode, meaning that the MOT field is switched off periodically for data acquisition (as described in Chapter 3). However, since the time the MOT field can be off is limited to around 1 ms in order not to lose too many atoms while the cloud is expanding, the MOT field has to be switched off and on very fast.

For the purpose of achieving maximal use of time for measurements, all involved procedures have to be timed precisely. The first step (loading cycle) will be to load the MOT from a decelerated atomic beam. This will involve opening a shutter in front of the Li oven, switching on the magnetic fields of the MOT and Zeeman slower and turning on the deceleration and trapping laser beams. After about 3 s the trap should be loaded with a few 10^8 atoms.

The experimental cycle starts with ramping down the trapping and slower fields in less than 200 µs and switching off the laser beams. While the atomic cloud is expanding ballistically with a velocity on the order of 0.4 m s^{-1} (corresponding to a Doppler temperature of 142 µK) measurements can be performed. Within 800 µs the atoms will travel only a distance of roughly 0.3 mm and therefore most of the target atoms can be recaptured by switching on the MOT field and lasers in the next step for 2 ms. This experimental cycle can be repeated several hundred times before a significant number of target atoms is lost and the MOT has to be loaded again. Figure 1.4 shows the timing procedure schematically.

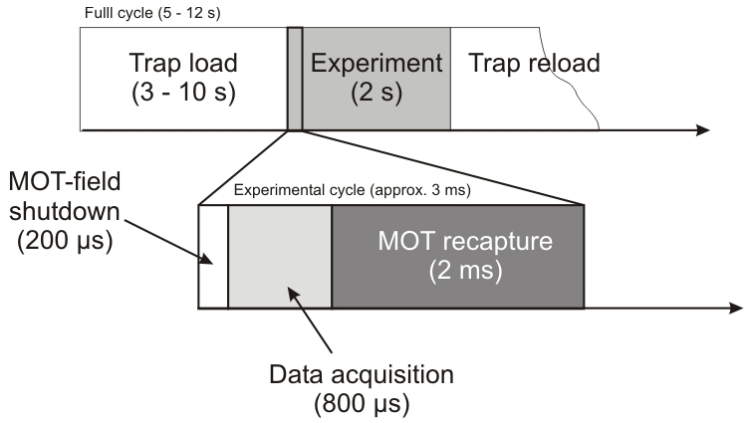

Figure 1.4: Timing sequence: With a full cycle of 5 s and 660 repetitions of the experimental cycle, the duty cycle for data acquisition will be 10 %.

1.3.1 Processes to be Studied

The presented set-up is suitable to study a great variety of phenomena and opens up the door to a new class of targets for the reaction microscope. One goal is to measure the fully differential cross section for triple ionisation of lithium by electron impact and for this purpose an electron gun is installed in the set-up.

Using the total cross sections from Table 1.4 the rates for triple ionisation by electron impact expected in a realistic experiment can be estimated. Given an electron gun that delivers 1000 eV electron pulses at a repetition rate of 500 kHz, the cathode current is set such that at every tenth pulse an electron is detected. In this way the chance for

multiple events is suppressed to ≤ 10 %. Taking into account false events and spourious background signals from secondary electrons, detection of Li^+ is expected with a rate of 10 kHz (empirically one always detects a factor five more electrons than ions). With the double-to-single and triple-to-double ratios from Table 1.4 this leads to detection of Li^{3+} in coincidence with one electron at a rate of 0.04 Hz. Detector efficiency of 50 % per electron leads to detection of Li^{3+} in coincidence with three electrons once every 100 s. By taking into consideration the duty cycle of 10 %, a full event of triple ionisation is detected every 1000 s (17 min), making stable operation of the experiment on the order of months crucial for gathering sufficient statistics.

In addition, it is planned to investigate ionisation by ion collisions. By making use of a new laser ion source (developed by D. Fischer and C. Höhr at the MPI-K), which can be easily flanged to the vacuum chamber, a great selection of projectiles is accessible. Due to the low ionisation potential of the 2s electron of only 5.4 eV the cold lithium cloud effectively represents a cold electron target and is thereby suitable for the study of capture reactions as performed by [Kno03] and [Ngu04] (MOTRIMS). Application of ultra-short femto second laser pulses enables experiments that study multi-photon ionisation and rescattering processes. Due to the high laser intensities achieved in such pulses, ionisation occurs at a high rate. Sufficient target densities are thus already obtained in the cold atomic beam from the Zeeman slower. It is hence possible to avoid the switching of MOT fields. Furthermore, a MOT offers the possibility of initial target state preparation as orientation of angular momenta by optical pumping or by laser-exciting target atoms. This will allow to probe the dependence of dynamical processes on internal atomic states. This idea can be extended to using spin polarised projectile electrons. These can be gained from a photo cathode that delivers very short and cold electron pulses [Orl04].

The set-up presented will provide a powerful tool for the study of quantum dynamics in diverse experiments. The completion of the set-up is anticipated eagerly and first experiments are awaited for late 2005. Because of the wide range of accessible phenomena to be investigated, a large profit to the understanding of the dynamics of many-body quantum systems is expected. Apart from the insight gained from the described apparatus it demonstrates the prototype of a new class of targets to be implemented into the reaction microscope. Especially alkali and alkaline earth metals can be trapped in a MOT with comparably little effort. In addition, it will be the first step to next generation experiments that will lead to the use of degenerate quantum gases as targets to probe the internal structure of ultra-cold atomic vapours. The effect of ionising an atom in the compound of a Bose-Einstein condensate (BEC) is unknown and under fervid discussion. For details about Bose-Einstein condensation of lithium see [Bra97] and references therein.

Chapter 2

Laser Cooling and Trapping

This chapter will briefly present the theoretical framework of the interactions between laser light and atoms needed to understand laser cooling. The two relevant forces here are the spontaneous light force or scattering force that comes from the momentum transfer of photons to an atom and the dipole force which originates from optical field gradients.

2.1 The Spontaneous Light Force

A two-level atom with velocity v in a resonant light field will continually absorb and spontaneously re-emit photons that carry momentum $\hbar k$ as shown in Figure 2.1.

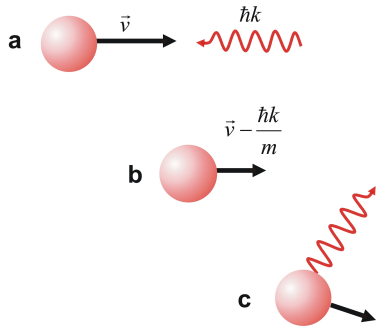

Figure 2.1: An atom with velocity v encounters a photon with momentum $\hbar k$ (a). After absorbing the photon, the atom is slowed by $\hbar k/m$ (b). After re-emission in a random direction (c), on average the atom is slower than in (a).

Since the photons that are scattered from the atom are always coming from the same direction and re-emission is isotropic, the net momentum transfer after many cycles is in direction of the incident laser beam. This momentum transfer leads to a force

$F_{sp} = \hbar k \gamma_p$ which depends on the total scattering rate of light from the laser field which is given by

$$\gamma_p = \frac{s_0 \gamma/2}{1 + s_0 + (2\delta/\gamma)^2}, \tag{2.1}$$

with the detuning δ of the laser field from the resonance frequency and s_0 the on-resonance saturation parameter which is defined by

$$s_0 = I/I_s \tag{2.2}$$

with the saturation intensity given by

$$I_s = \pi hc/3\lambda^3\tau. \tag{2.3}$$

with the laser wavelength λ and the lifetime τ of the excited state. The expression for the spontaneous light force can then be written as

$$F_{sp} = \frac{\hbar k \gamma}{2} \frac{s_0}{1 + s_0 + (2\delta/\gamma)^2}. \tag{2.4}$$

If two low-intensity beams of the same frequency, intensity and polarisation are directed opposite to each other (for example by retro-reflecting a single beam from a mirror), the net force is just the sum of the individual forces given by Equation 2.4. If the frequency of the laser beams is detuned to the red, a moving atom will always experience a force opposing its direction of motion because the light of the laser beam in direction of the atomic motion will be Doppler shifted away from resonance whereas the light from the opposing beam will be shifted towards resonance. Thus, the atom experiences a viscous damping force which is why this effect is also called optical molasses. A three-dimensional optical molasses can be obtained by using three intersecting orthogonal pairs of oppositely directed red-detuned laser beams [Hän75]. For the one-dimensional case the resulting force in an optical molasses is given by $\mathbf{F}_{OM} = \mathbf{F}_+ + \mathbf{F}_-$, where

$$\mathbf{F}_\pm = \pm \frac{\hbar \mathbf{k} \gamma}{2} \frac{s_0}{1 + s_0 + (2(\delta \mp \omega_D)/\gamma)^2} \tag{2.5}$$

with the Doppler shift ω_D. The sum of the two forces is then

$$\mathbf{F}_{OM} \cong \frac{8\hbar k^2 \delta s_0 \mathbf{v}}{\gamma(1 + s_0 + (2(\delta/\gamma)^2)^2} \equiv -\beta \mathbf{v}, \tag{2.6}$$

where terms of order $(kv/\gamma)^4$ and higher have been neglected. For a certain velocity range the force becomes linearly proportional to the velocity and can thus be described

as a damping force $F = \beta v$ with a damping constant β. This behaviour is shown in Figure 2.2.

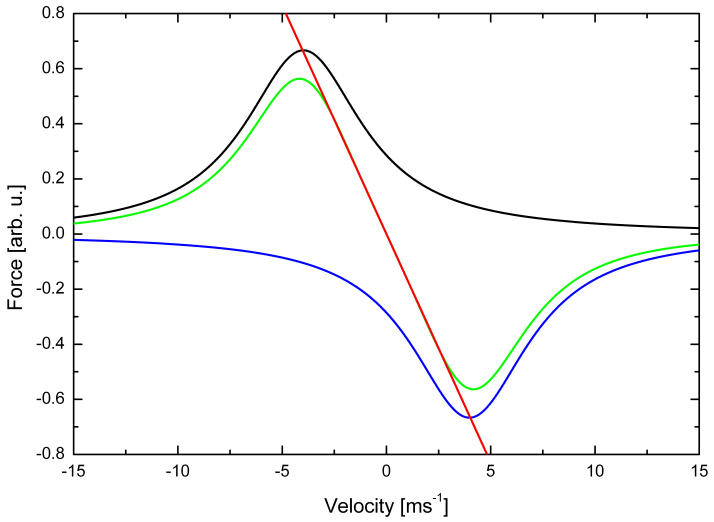

Figure 2.2: Velocity dependence of the spontaneous light force on a two-level atom placed in a one-dimensional optical molasses. The black and the blue curve show the force from each laser beam, respectively, the green curve is their sum. The red line shows how this force mimics a pure damping force over a certain velocity range.

2.2 Magneto-Optical Trapping

For the purpose of trapping atoms and keeping them localised, it is necessary to have a position dependent force. In an optical molasses the force is always pointed against the direction of motion. In order to obtain a force which is directed toward the centre of the trap, one has to apply a magnetic quadrupole field. A pair of magnetic coils in anti-Helmholtz configuration generates such a field gradient. Figure 2.3 shows the combination of the anti-Helmholtz coils and the six laser beams that form a three-dimensional optical molasses. In the centre of the trap where the lasers intersect, the magnetic field is zero and increases in all directions. Typical field gradients are on the order of 10–20 G/cm.

How this configuration of lasers and magnetic field generates a force that traps neutral atoms is illustrated in Figure 2.4 for the one-dimensional case with the simple atomic transition $J_g = 0 \rightarrow J_e = 1$. In this simplified picture, two counter-propagating lasers with opposite circular polarisation are overlapped with a magnetic field gradient. In the centre of the trap where the field is zero the atoms are out of resonance since the laser frequency is red-detuned by a few linewidths. In the outer regions of the trap, the magnetic field Zeeman shifts the atomic levels of the excited state. The $m_e = +1$

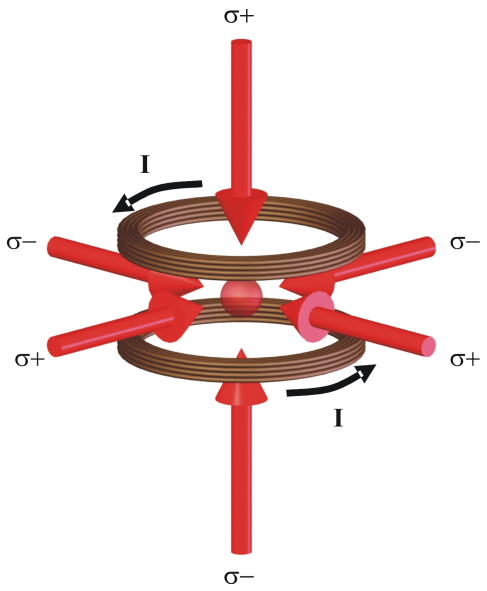

Figure 2.3: Schematic picture of a magneto-optical trap. Six laser beams intersect in the centre of the trap where the magnetic field from the anti-Helmholtz coils is zero.

state is shifted up for $B > 0$ whereas $m_e = -1$ is shifted down. At position z' in Figure 2.4, the magnetic field therefore tunes the $\Delta m = -1$ transition closer to resonance and the $\Delta m = +1$ transition further out of resonance. If the polarisation of the laser beam incident from the right is chosen to be σ^- and correspondingly σ^+ for the other beam, more light is scattered from the beam pointing toward the centre of the trap. Thus, atoms are always driven back towards the centre.

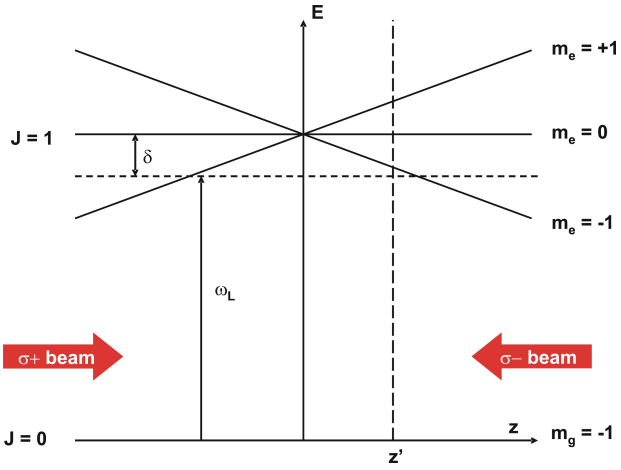

Figure 2.4: Simplified energy level diagram of a MOT in 1D.

The situation is analogous to the velocity damping in an optical molasses from the Doppler effect, but here it operates in position space, whereas for molasses it operates in

velocity space. Since the laser light is detuned below the atomic resonance in both cases, compression and cooling of the atoms is obtained simultaneously in a MOT [Met99].

2.3 The Dipole Force

In this section the second light force acting on neutral atoms is introduced. Although the presented set-up is operated without the concept of the dipole force it is described briefly because it might prove useful for future improvements of the experiment. A detailed description of optical dipole traps can be found in [Gri00].

When an atom is placed into laser light, the electric field $\mathbf{E}$ induces an atomic dipole moment $\mathbf{p}$. Electric field and dipole moment oscillate at the same driving frequency ω. In the complex notation $\mathbf{E} = \hat{\mathbf{e}} E_0(\mathbf{r}) e^{-i\omega t} + c.c.$ and $\mathbf{p} = \hat{\mathbf{e}} p_0(\mathbf{r}) e^{-i\omega t} + c.c.$, where $\hat{\mathbf{e}}$ is the unit polarization vector and E_0 and p_0 denote the amplitudes, respectively, which are simply related by

$$p_0 = \alpha E_0. \tag{2.7}$$

Here, α is the complex polarisability which depends on the driving frequency ω. The interaction potential U_{dip} of the induced dipole moment $\mathbf{p}$ in the driving field $\mathbf{E}$ is

$$U_{dip} = -\frac{1}{2} \langle \mathbf{p} \cdot \mathbf{E} \rangle = -\frac{1}{2\epsilon_0 c} Re(\alpha) I, \tag{2.8}$$

where the angular brackets stand for time averaging and the factor 1/2 takes into account that the dipole moment is an induced and not a permanent one. The potential energy of an atom in a field is therefore proportional to the intensity $I = 2\epsilon_0 c |E_0|^2$ and the real part of the polarisability, which describes the in-phase component of the dipole oscillation that is responsible for the dispersive properties of the interaction. Because U_{dip} is a conservative potential the *dipole force* is obtained by taking the gradient

$$\mathbf{F}_{dip} = -\nabla U_{dip}(\mathbf{r}) = -\frac{1}{2\epsilon_0 c} Re(\alpha) \nabla I(\mathbf{r}). \tag{2.9}$$

It is thus a conservative force, proportional to the intensity gradient of the driving field. A laser with high power, focussed to a small spot can easily achieve very high intensity gradients. Under the right conditions atoms are trapped in the focus of the laser beam. Such a purely optical trap might also prove useful as a target for a reaction microscope because no magnetic fields that would disturb the trajectories of charged fragments from ionisation processes are required. However, a dipole trap still requires a magneto-optical trap as a reservoir of cold atoms from which it can be loaded with the draw-back that this process is quite inefficient with a loading probability on the order of 1–10 %.

Chapter 3

Experimental Set-Up

The experimental set-up consists of two separate parts: the vacuum chamber and the laser system. The latter will be discussed in Chapter 4. The vacuum system is made up of the main vacuum chamber and the Zeeman slower. The Zeeman slower is presented in Chapter 5. Here only the aspects which are important for the vacuum system will be mentioned. A CAD-drawing of the vacuum system rendered from a SolidWorks file is shown in Figure 3.1.

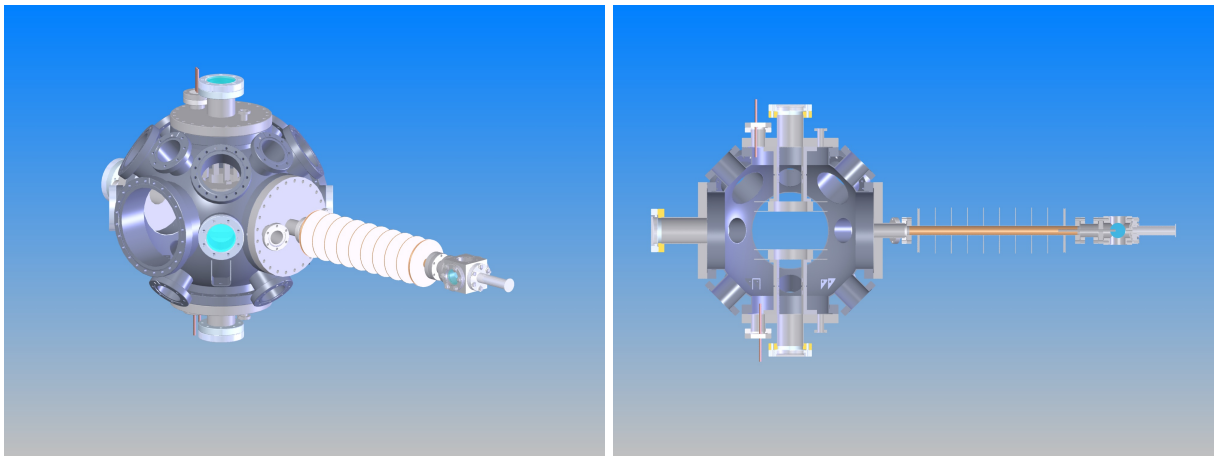

Figure 3.1: Drawing of the vacuum system with main chamber and Zeeman slower.

3.1 The Main Vacuum Chamber

The main vacuum chamber basically is a steel sphere of 40 cm diameter with six CF200, four CF100 and twelve welded CF63 flanges which allow for the connection of pumps, windows, gauges and other equipment such as the magnetic coils and the detector chambers. The size of the chamber was determined by the need to place the magnetic

coils for the magneto-optical trap as well as the extraction electrodes of the reaction microscope inside. Pictures of the vacuum chamber are shown in Figure 3.2.

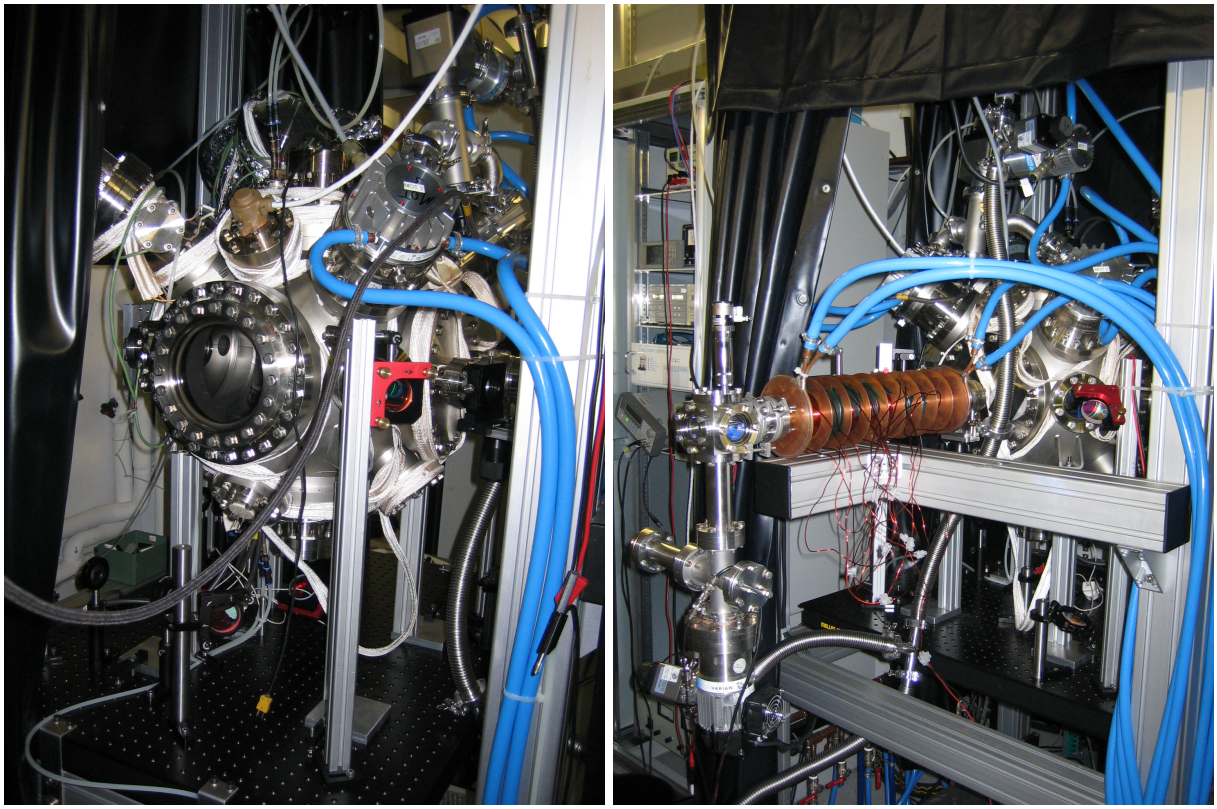

Figure 3.2: Images of the set-up taken with a digital camera.

The detector chambers which will house the multi-channel-plate (MCP) detectors were not connected to the system yet, since they were not necessary for setting up the magneto-optical trap for the first time. They will be added to the system in the future once all components of the spectrometer are completed. The two unused CF200 ports were therefore closed by a blank flange and a viewport respectively.

The remaining two CF200 ports in the horizontal plane are closed by two custom-made flanges that are shown in Figure 3.3.

To the on-axis ports of these clusters the Zeeman slower and the CF63 window are flanged as displayed in Figure 3.1. The off-axis CF40 ports are also closed with windows which are useful optical entrances for analysis of the MOT (i.e. CCD-cameras and photo diodes).

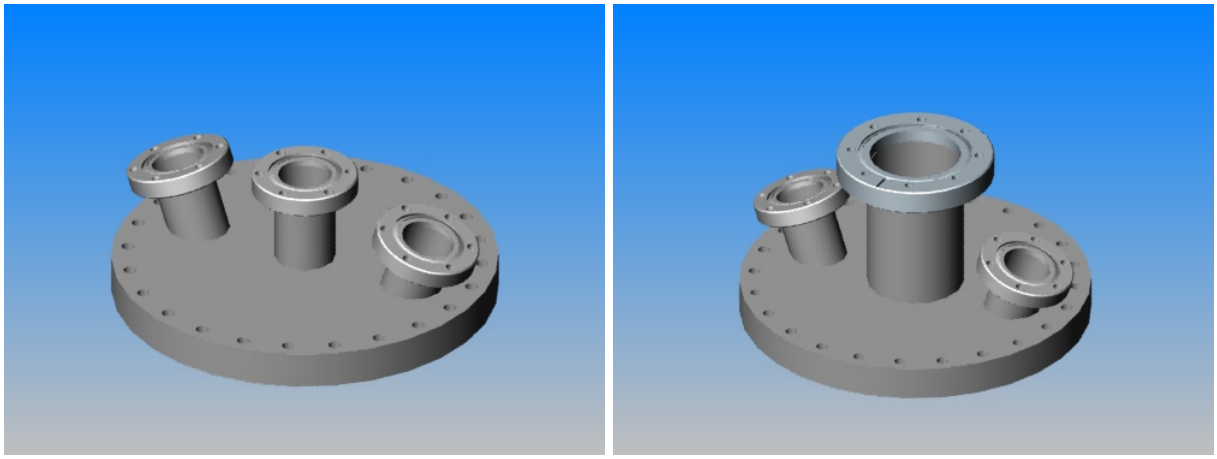

Figure 3.3: Flange clusters made in the mechanical workshop for connecting the Zeeman slower and additional viewports to the main chamber. Left: CF200 with 3 CF40 ports. Right: CF200 with 2 CF40 and a CF63 port.

3.1.1 The MOT Coils

As mentioned in Section 1.3, the magnetic field of the MOT has to be switched off during data acquisition. For fast switching of magnetic fields [Ded01] small inductivity is required. This is achieved by using a small number of windings n with small diameter D ($L \propto n^2, D^2$), by putting the pair of anti-Helmholtz coils close together and by taking care that there is no closed conducting surface within the coils where eddy currents could be induced.

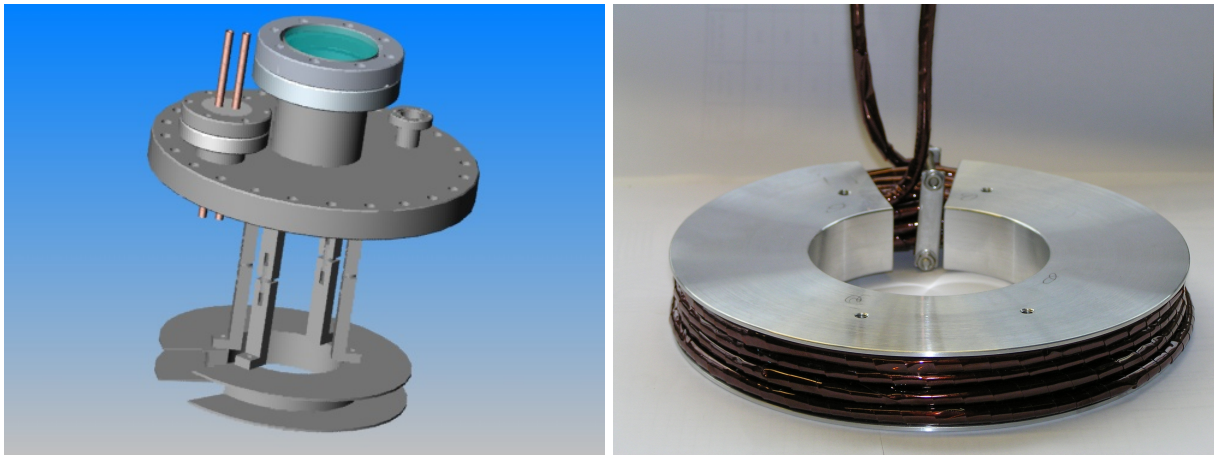

Figure 3.4: CAD drawing of the flange that carries the MOT coils. Displayed are the feed-throughs for water and current, the CF16 port for temperature control and the rim for the copper tube windings. A finished wound coil is shown on the right.

In this experimental set-up which is shown schematically in Figure 1.3 the MOT coils are made up of n = 24 windings of 5×1 mm copper tube isolated by KAPTON foil. The diameter of the coils is 12 cm and they are placed inside the vacuum chamber with a distance of 10 cm to each other. With an operational current of 60–100 A water-cooling is required. To account for the shift of the zero-field point of the MOT field by the spectrometer coils, a pair of compensation coils is added into the vacuum. The relatively large dimensions of the MOT coils are necessary to fit the reaction microscope's extraction electrodes in between. A picture and a CAD-image of the coils is shown in Figure 3.4.

3.2 Vacuum Pumps

A total of four pumps are directly connected via the CF100 ports to the main vacuum chamber: two 300 litre/s VARIAN turbo pumps, a titanium sublimation pump and a SAES getter pump. The pre-vacuum for the turbo pumps is generated by a VARIAN dry scroll pump that achieves a pressure of about 10^{-3} mbar and a 70 litre/s VARIAN turbo pump at which's end the vacuum is at 10^{-6} mbar. After two weeks of bake-out at up to 250 ℃ and application of the sublimation and getter pumps the pressure in the main chamber was down to $3{\cdot}10^{-10}$ mbar.

Chapter 4

The Laser System

For laser cooling and trapping of lithium atoms, a narrow-bandwidth laser source with a wavelength of 671 nm and optical power of about 200 mW is needed. Several laser sources are available that operate at the lithium wavelength such as laser diodes ([Hof96], [Ger98]), dye-lasers and solid state lasers. The first aim of this diploma work was to design, explore advantages and disadvantages of and to finally set up a high-power diode laser system which is described in the following Section 4.1. However, because an operating dye-laser system was available on short notice, offering more stable and easier operation conditions, it was used in order to quickly set up the magneto-optical trap and to perform first measurements on it within the given time constraints. The dye-laser is described in Section 4.2.

The Grotrian diagram for lithium is depicted in Figure 4.1. Indicated in this picture are the D2 transitions used for laser cooling. The $2^2S_{1/2}(F = 2) - 2^2P_{3/2}(F' = 3)$ transition is a closed transition and, therefore, most suitable for laser cooling. However, with a natural linewidth Γ = 2π·5.92 MHz and with typical laser bandwidths of a few MHz the hyperfine structure of the excited state cannot be resolved. A fortiori, the simultaneous excitation to other hyperfine states is possible which leads to decay to the $F = 1$ ground state. Atoms in this hyperfine ground state do not interact with the cooling laser anymore and have to be repumped by a second laser frequency which is 803.5 MHz higher. In the case of lithium this coupling of the ground states is quite strong and, thus, the repumping transition needs approximately 50 % of the total laser power.

4.1 The Diode Laser System

With the development of powerful laser diodes in the infra-red and optical regime, very stable and cheap laser systems can be realised that can be used in the atomic physics laboratory [Wie91]. Single-mode cw laser diodes are commercially available with free-

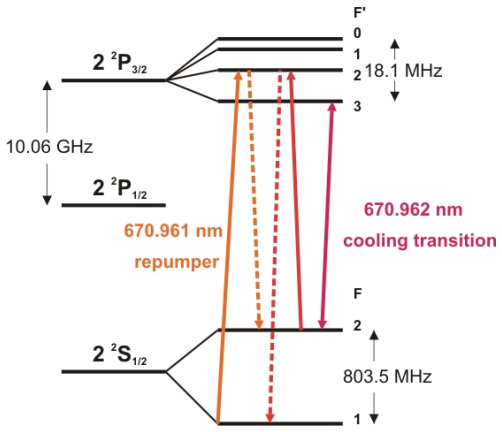

Figure 4.1: Energy level diagram of ^{7}Li. The nuclear spin of ^{7}Li is $I = 3/2$.

running (i.e. without feedback or injection locking) powers of up to about 200 mW depending on the wavelength. Especially in the infra-red, high powers are achieved at wavelengths of around 780 nm, used for laser cooling and spectroscopy of Rb, K and Cs.

The working principle of a laser diode is presented in many publications and text books (for example [Dem96]). Here, only a short explanation will be given to understand the basic features. The active medium of a laser diode is a p-n-junction formed by two doped gallium-arsenide layers. The junction is forward-biased so that electrons and holes recombine and emit light that can be amplified when passing the p-n-junction. The end facets of the semiconductor structure have to be optically flat with one end mirrored and one end partially reflective. Because of the high refractive index of GaAs ($n \approx 3.5$ at λ = 850 nm) the reflectivity becomes

$$R = \left(\frac{n-1}{n+1}\right) \approx 0.3$$

and, therefore, the end facets can be left without reflective coating. On the contrary, most laser diodes are coated with an anti-reflective layer for more efficient feedback into the diode from an external cavity.

The length of the junction must be precisely related to the wavelength of the light to be emitted. At small forward currents incoherent light is emitted just like from an LED (light emitting diode). At higher currents photons moving parallel to the junction can stimulate emission and initiate laser action. Typical threshold currents of laser diodes are on the order of a few 10 mA. Typical operating currents are a 100–200 mA giving optical outputs of about 30–50 mW. Laser diodes are thus very efficient at transforming electrical to optical power.

The standard set-up to obtain a compact, economic and versatile diode laser system based on commercial laser diodes, which is optically stabilised by means of feedback

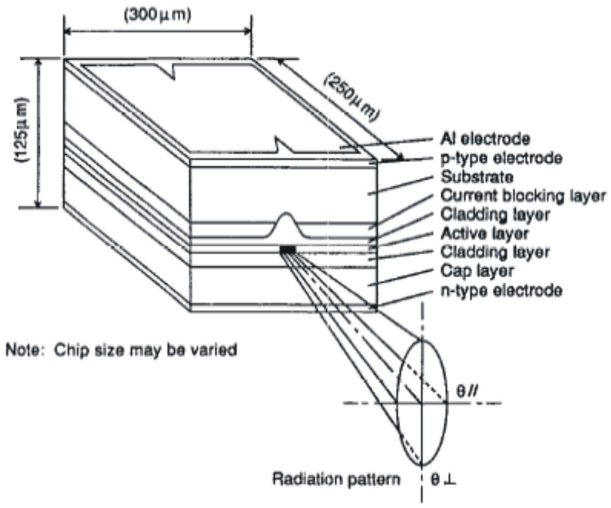

Figure 4.2: Illustration of the different layers of a laser diode. The rectangular shape of the gain region leads to the oval shape of the beam (picture from [Wie91]).

from a diffraction grating is described in [Ric95] and called external cavity diode laser (ECDL). Here, the collimated beam from a laser diode is directed onto a diffraction grating. The angle of the blazed grating with respect to the beam is such that the first order reflection is sent back into the laser diode and generates feedback. The zero-order reflection is used as the output beam. This set-up is called *Littrow* configuration and depicted in Figure 4.3. To prevent beam walk of the output when tuning the grating, an additional mirror can be used to have a fixed output beam [Haw01]. This configuration is shown in Figure 4.4.

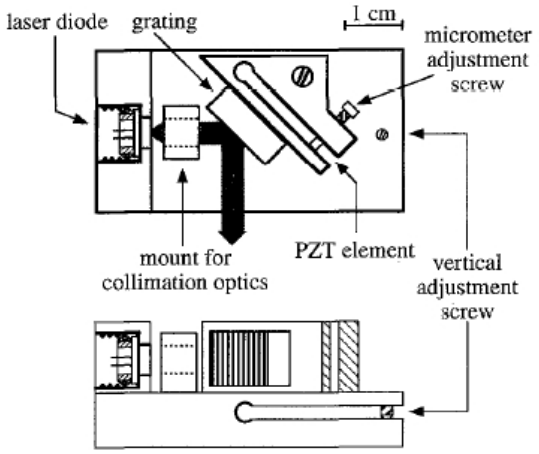

Figure 4.3: Schematics of the mechanical set-up of an external cavity diode laser in Littrow configuration (from [Ric95]).

The grating serves as a frequency-selective element and by slightly changing the angle, the frequency of the laser diode can be tuned within a range of some nm. By changing the temperature of the laser diode the wavelength can also be tuned by a few nm. This works simply due to the fact that the size of the resonator is changed. For this purpose the housing of the diode is usually made of one piece of metal (brass) which is mounted on a Peltier element that also stabilises the temperature. Besides temperature and grating angle, also the current through the diode has influence on the frequency. The final output frequency is then basically determined by the overlap of the internal (free spectral range (FSR) $\approx$ 600 GHz) and external (FSR $\approx$ 3 GHz) cavity modes with the gain profile of the active region and some loss factors that arise from imperfections of the resonators. Some basic principles of the external cavity diode laser are explained in [Boe96], [Hof01], [Ric95] and [Wie91].

4.1.1 Injection Locking

At the wavelength needed for laser cooling of lithium atoms (671 nm) no high-power single-mode laser diodes are available on the market. The highest free-running power of commercially available diodes is around 30 mW. One possible solution is to use pairs of master and slave lasers and to apply injection locking schemes such as described in [Sch94] and [Sch98]. To achieve high powers above 100 mW it is also possible to use high-power broad-area laser diodes as slaves ([Boe96], [Boe97], [Pra98] and [Shv00]). Broad-area laser diodes are like normal laser diodes with a larger area of the active region, which emit several spatially separated modes when running free. They provide optical output powers of about 500 mW for red light. One principal goal of the present work was to set up a high-power diode laser system that employs injection locking from a single-mode master diode laser into broad-area laser diodes [Pra98] in order to achieve the light intensity needed for the MOT operation.

When the light of a narrow-bandwidth grating-stabilised master laser is injected into the broad-area laser at a small angle, it gets amplified in the active medium and leaves the broad-area diode laser (BAL) at the specular reflection angle, if the injected light enters the chip with matching mode characteristics. That means that the seeding beam has to have the same polarisation, direction and divergence as the outgoing mode. The active layer of the slave laser then serves as a second resonator and also has to fulfil the resonance condition for the injected wavelength which can be regulated by adjusting the temperature.

The master laser in this set-up is a TOPTICA DL100L. This is a grating-stabilised diode laser system mounted in Littrow configuration with fixed direction output beam [Haw01]. The output power of the free-running laser diode is 35 mW at 80 mA, its threshold current is 35 mA. The central wavelength is 675 nm. A blazed grating (2200 l/mm) reflects the first order back into the diode and forms an external cavity. Small corrections to the angle of the grating give a coarse tuning range from 670–677 nm. The

zero-order reflection is used as the output beam. The grating is mounted on a PZT so that the length of the cavity can be adjusted, thus giving a fine tuning range of 20 GHz (mode hop free). At an operating current of 59 mA and 20 ℃ the output is 15.5 mW. A collimator (f = 4.5 mm) is mounted in front of the laser diode.

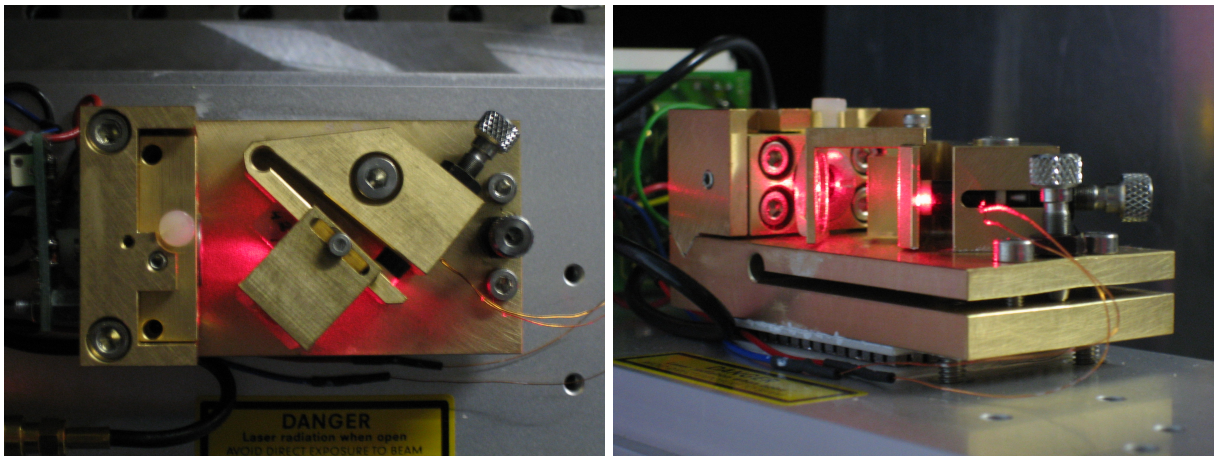

Figure 4.4: Picture of the TOPTICA DL100L's interior. The laser is mounted in Littrow configuration with fixed direction output beam.

The output of the master is used to seed a COHERENT S-76-500C-100-H broad-area high-power laser diode mounted in a high-heat load package with a free-running output power of about 500 mW at approximately 900 mA and 25 ℃. The threshold current is about 420 mA. For better temperature stabilisation the diode package is mounted to air cooled laser diode mounts (NEWPORT 760-H). Indium foil between the back of the high-heat package and the heat exchanger ensures proper thermal conduction. The BAL is driven and temperature controlled by a ILX LIGHTWAVE LDC-3700B laser diode controller.

Laser diodes emit very divergent light beams. This is due to the small dimensions of the diode's active region — typically on the order of 100 µm × 400 µm for single-mode diodes (see Figure 4.2). In the case of BALs the active region is much larger (100 µm × 1000 µm width × length). The thickness is about the same as for single-mode diodes (1 µm). For the master laser the divergence of the free diode is 24 ° perpendicular and 8 ° parallel to the active layer. For the slave laser 31 ° perpendicular and 5.5 ° parallel. The polarization is usually parallel to the active layer.

The slave laser's output is diffraction limited in the y-direction[1]. A collimator (MELLES GRIOT 06GLC001, numerical aperture 0.61, f = 6.5 mm) is placed in front of the diode so that the output is collimated in the y-direction. At currents slightly above threshold two or more spatial modes are visible. With higher currents their number increases. The bandwidth of the free diode is on the order of 1–2 nm.

[1]The z-direction is that of laser beam propagation, x and y span the perpendicular plane, where x is in the horizontal and y in the vertical direction.

In order to keep the laser beams in the plane parallel to the laser table, the BAL is mounted with the active layer parallel to the table. The spatial modes of the BAL are thus vertical lines parallel to each other when observed on a screen in the x-y-plane. However, since the master laser is mounted perpendicular to that, its polarisation has to be turned by 90° using a half-wave plate. Also, to match the spatial modes of the BAL, the profile of the master beam is shaped to that of the BAL by an anamorphic prism pair (APP). The profiles of the master before and after beam shaping and that of the BAL, measured with a CCD camera are shown in Figure 4.5. After passing through the APP, the profile of the master beam is very similar to that of the BAL.

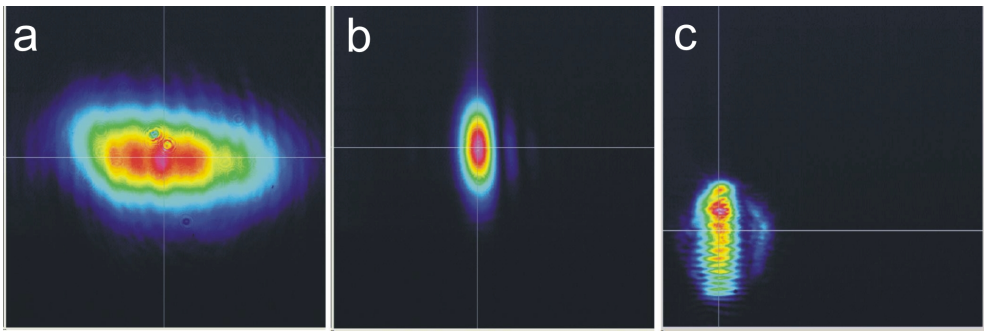

Figure 4.5: Profiles of master beam before (a) and after (b) beam shaping and the profile of the BAL's mode which is coupled out after the collimator (c) taken with a CCD camera.

As is illustrated in Figure 4.7, after beam shaping the master laser passes through an aperture that exactly fits the size of the beam and a cylindrical lens with f = 80 mm in order to enter the BAL under a small angle. The alignment procedure works as follows: without the cylindrical lens and the BAL's collimator the master beam is directed perpendicular onto the front facet of the BAL. The collimator is placed back again so that the output of the BAL is collimated in the y-direction and overlaps with the master beam. Then the cylindrical lens is placed such that it forms a telescope with the collimator. A schematic picture that shows the details of the coupling of the master beam into the slave diode facet is displayed in Figure 4.6.

When the cylindrical lens is moved along the x-direction, feedback can be observed on the backside of the pinhole because the amplified beam exits the BAL at specular reflection so that it can be coupled out by a mirror as shown in Figure 4.7.

A picture of the actual set-up is shown in Figure 4.8. The path of the laser from the master to the slave is indicated by the red line.

Although the quality of the alignment can easily be verified by eye, it helps a lot to use a power meter for fine-tuning. Another good way to check for optimum injection is to use a CCD camera to measure the intensity profile of the amplified beam. In Figure 4.20 three dimensional intensity distributions are shown for no injection locking, bad alignment of the seeding beam and for successful injection.

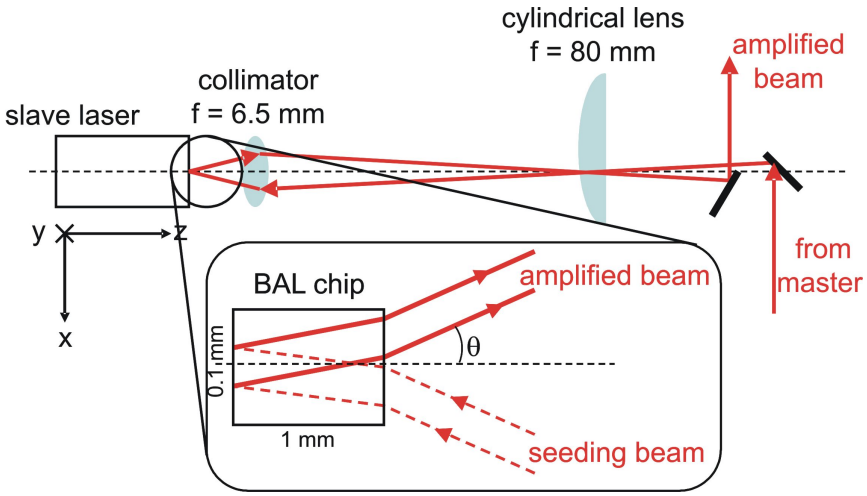

Figure 4.6: Set-up for injection locking. The cylinder lens is slightly displaced in the x-direction from the optical axis z to achieve injection of light under a small angle θ relative to the optical axis.

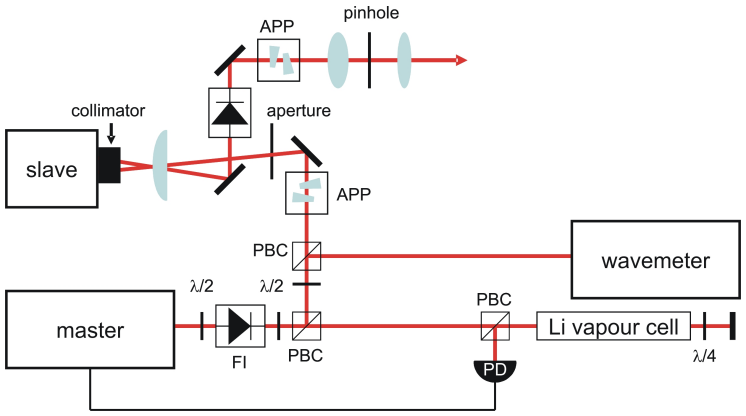

Figure 4.7: Set-up for injection locking. PBC: polarising beam-splitter, λ/2: half-wave plate, λ/4: quarter-wave plate, PD: photo diode, APP: anamorphic prism pair, FI: Faraday Isolator.

4.1.2 Frequency Stabilisation

In order to achieve laser cooling of atoms the bandwidth of the laser has to be smaller than the natural linewidth of the atomic transition and the laser frequency has to be stabilised to the transition frequency of the atoms. As discussed before the needed wavelength for laser cooling of lithium is 670.962 nm. Due to the hyperfine splitting of the ground state two frequencies are necessary. Therefore, the frequency of the master laser is locked to the crossover of the two hyperfine transitions and the two transition frequencies are generated by shifting the frequency by plus and minus 400 MHz using acousto-optic modulators (AOM).

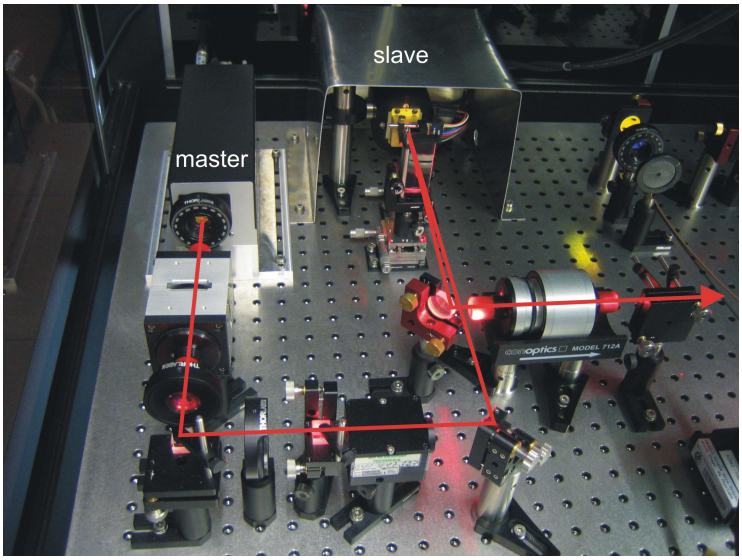

Figure 4.8: Picture of the set-up for injection locking from the master laser into the slave.

The frequency lock itself is done by applying the Pound-Drever-Hall method [Bla01] which is also known as FM-spectroscopy (frequency modulation). The basic idea of this method is to convert a frequency modulation (FM) of a laser beam into an amplitude modulation (AM) by interaction with a medium. The optical set-up is exactly the same as for saturation spectroscopy [Dem81]. The laser beam is directed through a lithium vapour cell and retro-reflected onto itself, thus, having an overlapping pump- and probe-beam. After coming back through the cell the probe-beam is directed onto a fast photo diode. The set-up is also shown in Figure 4.7. The vapour cell consists of a 500 mm long stainless-steel vacuum tube with CF16 windows at the ends. A piece of metallic lithium inside the cell is heated to approximately 250 ℃ by a bifilar heating-wire which is wound around the middle section of the tube. The cell is evacuated to a pressure of smaller than 10^{-2} mbar.

Using this set-up the spectra of the ^{7}Li D1 and D2 lines as well as the ^{6}Li D2 lines could be measured. They are shown in Figure 4.9 and were taken by simultaneously scanning the grating angle and the current of the laser diode which gives a wider mode-hop free tuning range. The relative frequencies are listed in Table 4.1. Since the spectrum also shows the D2 lines of ^{6}Li, the magneto-optical trap could also be set to trap the fermionic lithium isotope.

From the crossover line of the ^{7}Li D2 transitions an error signal has to be generated to be able to lock the laser. This is done by applying a 20 MHz modulation on the current of the laser diode. This generates side-bands to the carrier frequency which are visible in the transmission signal from a Fabry-Perot interferometer shown in Figure 4.10.

The signal from the fast photo diode is now fed into the Pound-Drever-Hall detector (PDD 110), which is a part of the TOPTICA diode laser controller. The PDD 110 deter-

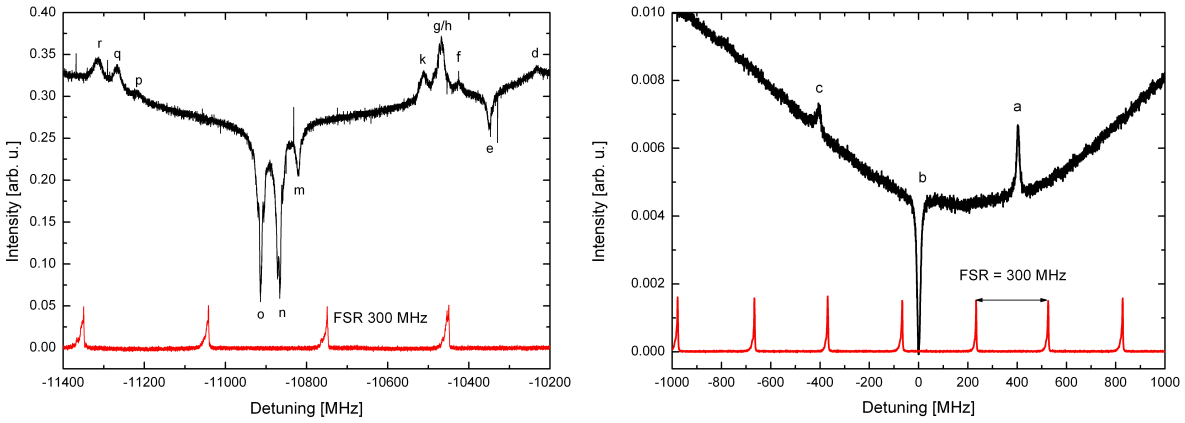

Figure 4.9: Spectra of the ^{7}Li D1 and ^{6}Li D2 line (left) and of the ^{7}Li D2 line (right). The laser is locked to the crossover peak (b) of the ^{7}Li D2 line. The other lines are identified in Table 4.1.

Table 4.1: Relative frequencies of the ($^6_3$Li, I = 1) and ($^7_3$Li, I = 3/2) transitions. The measured spectra are shown in Figure 4.9

ID	Line	Transition	F_g	F_e	Relative frequency [MHz]
a	^{7}Li D2	$2^2S_{1/2} - 2^2P_{3/2}$	1	0, 1, 2	+401.8
b	^{7}Li D2	crossover (a-c)			0
c	^{7}Li D2	$2^2S_{1/2} - 2^2P_{3/2}$	2	1, 2, 3	-401.8
d	^{6}Li D2	$2^2S_{1/2} - 2^2P_{3/2}$	3/2	1/2, 3/2, 5/2	-10234
e	^{6}Li D2	crossover (d-h)			-10358
f	^{7}Li D1	$2^2S_{1/2} - 2^2P_{1/2}$	2	1	-10425
g	^{7}Li D1	crossover (f-k)			-10468
h	^{6}Li D2	$2^2S_{1/2} - 2^2P_{3/2}$	1/2	1/2, 3/2	-10483
k	^{7}Li D1	$2^2S_{1/2} - 2^2P_{1/2}$	2	2	-10513
m	^{7}Li D1	crossover (p-f)			-10820
n	^{7}Li D1	crossover (r-f, p-k)			-10866
o	^{7}Li D1	crossover (r-k)			-10914
p	^{7}Li D1	$2^2S_{1/2} - 2^2P_{1/2}$	1	1	-11217
q	^{7}Li D1	crossover (p-r)			-11267
r	^{7}Li D1	$2^2S_{1/2} - 2^2P_{1/2}$	1	2	-11317

mines the phase delay (dispersion) of the modulated laser light while passing through the vapour cell, by comparing the phases of carrier and side-band. It thus generates the Pound-Drever-Hall error signal. Due to the law of Kramers and Kronig [Lan84], maximum absorption is equal to zero dispersion. By the aid of a PID-regulator (PID 110), the error signal can be used to lock the laser to the frequency of maximum absorption in the vapour cell. Neglecting amplitude modulation, a current modulated laser diode emits the following electric field [Top02]

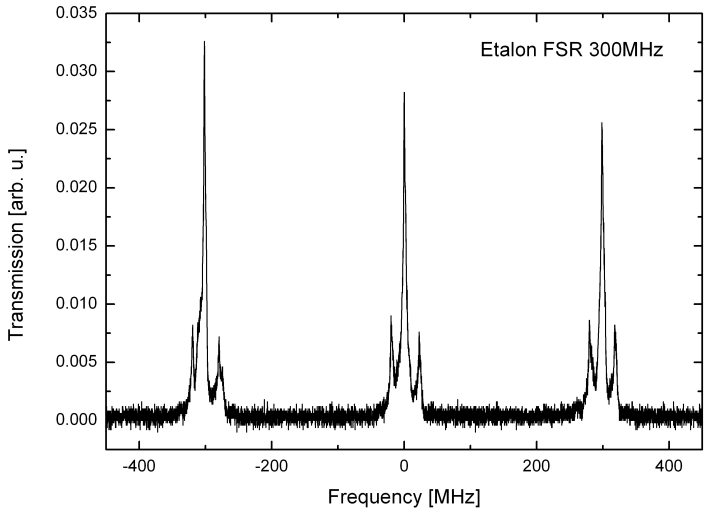

Figure 4.10: Transmission signal from a 300 MHz FSR Fabry-Perot etalon with the side-bands of the 20 MHz modulation.

$$E_{FM}(t) = \frac{E_0}{2} \exp[i\omega_0 t + M \sin \omega_m t] + c.c. \tag{4.1}$$

where ω_0 denotes the emission frequency of the unmodulated laser light and ω_m is the modulation frequency. M is the so-called phase modulation index. Using a series expansion into Bessel function $J_k(x)$ one obtains

$$E_{FM}(t) = \frac{E_0}{2} \sum_{k=-\infty}^{\infty} J_k(M) e^{i(\omega_0 + k\omega_m)t} + c.c. \tag{4.2}$$

The modulation yields a large number of new frequency components, so-called side-bands of the carrier frequency ω_0, each with a frequency distance of ω_m to the next. For M = 1 the relative intensities $I_k = |a_k|^2 / |a_0|^2$ of the kth side-bands can be calculated as [Top02]

$$I_0 = 1,\ I_{\pm 1} = 0.33072,\ I_{\pm 2} = 0.02255,\ I_{\pm 3} = 0.00065.$$

Thus, the second side-band may be already neglected for most applications. The electric field after passing through the vapour cell is

$$E_T(t) = \frac{E_0}{2} \sum_{k=-\infty}^{\infty} J_k(M) T_k e^{i(\omega_0 + k\omega_m)t} + c.c. \tag{4.3}$$

where the transmission coefficients

$$T_k = \exp(-\delta_k - i\phi_k)$$

describe both absorption $\delta_k = \alpha_k I/2$ and phase delay $\phi_k = n_k I\omega_k/c$ in the vapour. The index k indicates that the particular value has to be calculated for the frequency $\omega_0 + k\omega_m$. A fast photo diode with a bandwidth broader than the modulation frequency ω_m detects all frequency components with DC and $1{\cdot}\omega_m$ of the transmitted intensity

$$I_T(t) = \frac{c\epsilon_0}{2} |E_T(t)|^2 .$$

In the approximation of slowly varying absorption and phase delay and for a small phase modulation index M, the contributions of the $I_T(t)$ signal measured by the photo detector can be calculated as

$$I_T(t) \approx e^{-2\delta_0} M[1 + (\delta_{-1} - \delta_1)\cos(\omega_m t) + (\phi_1 + \phi_{-1} - 2\phi_0)\sin\omega_m t]. \tag{4.4}$$

The detected signal contains the in-phase contribution $\phi_1 + \phi_{-1} - 2\phi_0$ and the quadrature contribution $\delta_{-1} - \delta_1$. Experimentally, the two components can be separated by mixing the detected AM signal with the modulation signal as a reference with variable phase difference. This is done in the phase detector of the PDD 110. In this device the frequency components with $1 \cdot \omega_m$ are mixed with $\sin(\omega_m t)$ and converted into a DC signal by the aid of a low pass filter. This DC signal is the desired error signal. In Figure 4.11 the set-up of the modules for frequency stabilisation is shown schematically.

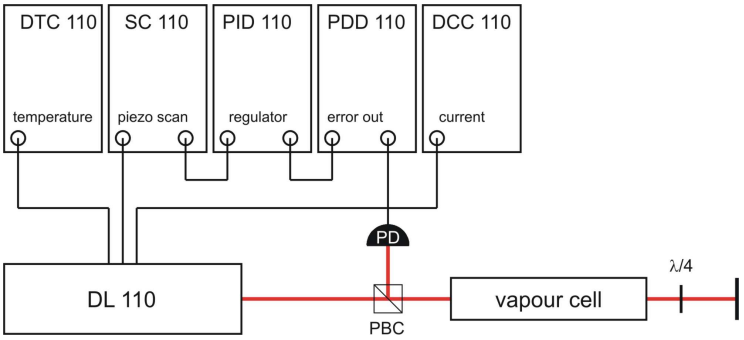

Figure 4.11: Connection of the frequency stabilisation modules.

The spectroscopy signal and the resulting error signal together with the transmission through a Fabry-Perot interferometer is shown in Figure 4.12.

Using this error signal the PID-regulator module of the diode laser controller compensates drifts of the carrier frequency via an internal connection to the scan control SC 110 which controls the piezo-electric elements to which the diffraction grating is connected. Fast frequency variations are compensated by directly feeding the error signal output from the PDD 110 to the FET connector of the diode laser. Except for heavy shocks or

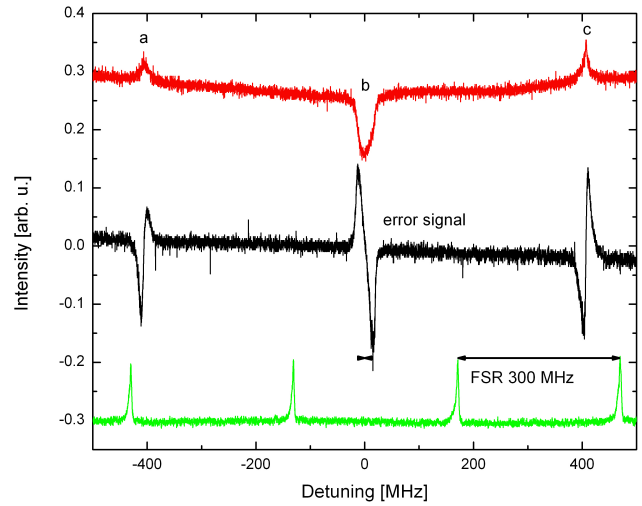

Figure 4.12: Oscilloscope signals from the photo diode (red), the Pound-Drever detector (black) and the transmission etalon (green).

vibrations caused for instance by letting an Allen key fall onto the optical bench, the frequency lock is stable for many hours. In Figure 4.13 the regulation signal is plotted as a function of time for 100 s.

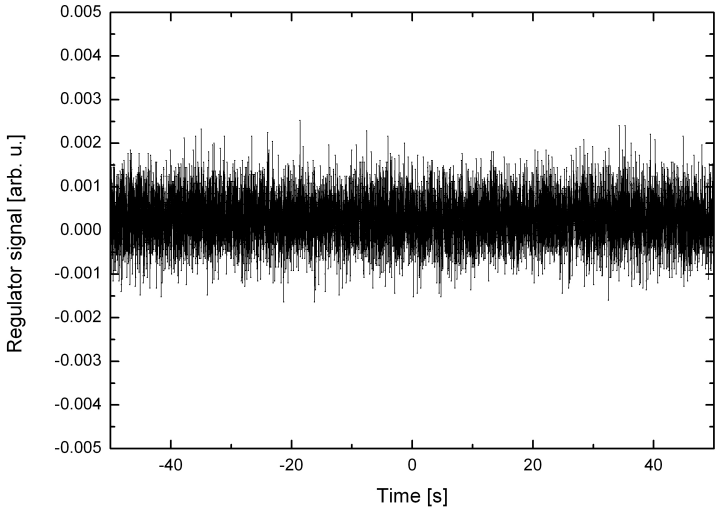

Figure 4.13: Regulation signal from the PID-controller (PID 110).

4.1.3 Characterisation of the Diode Laser System

A first simple measurement shows the dependence of the optical output power of the master laser on the forward current through the laser diode. The result is shown in

Figure 4.14. Lasing sets in when a threshold current of 33 mA is reached. At an operating current of 60 mA the output power is at about 15 mW.

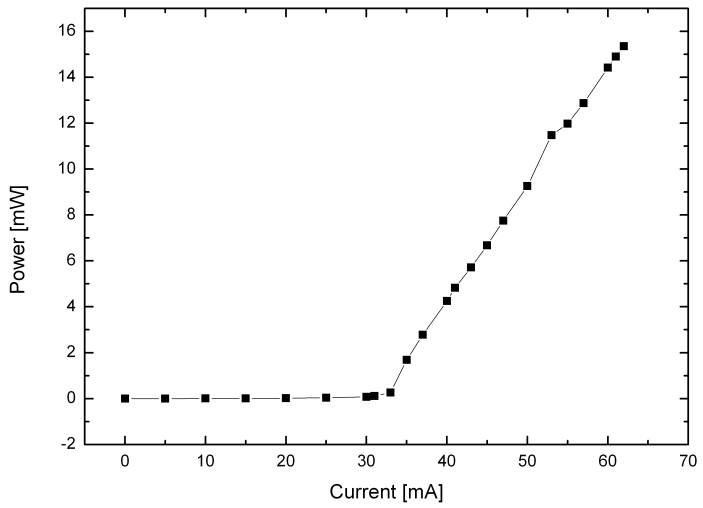

Figure 4.14: Output power versus applied forward current through the laser diode of the master laser measured with a power meter. The threshold current is at 33 mA.

In order to measure the spectral characteristics of the master laser and to verify whether it runs single- or multi-mode, its light was directed into a standard Fabry-Perot interferometer with a free spectral range of 300 MHz. Figure 4.15 shows measurements with the laser in single- and multi-mode. If the diode laser is adjusted correctly, it is very easy to handle and does not lase multi-mode when normal operation conditions (i.e. temperature and current) are applied.

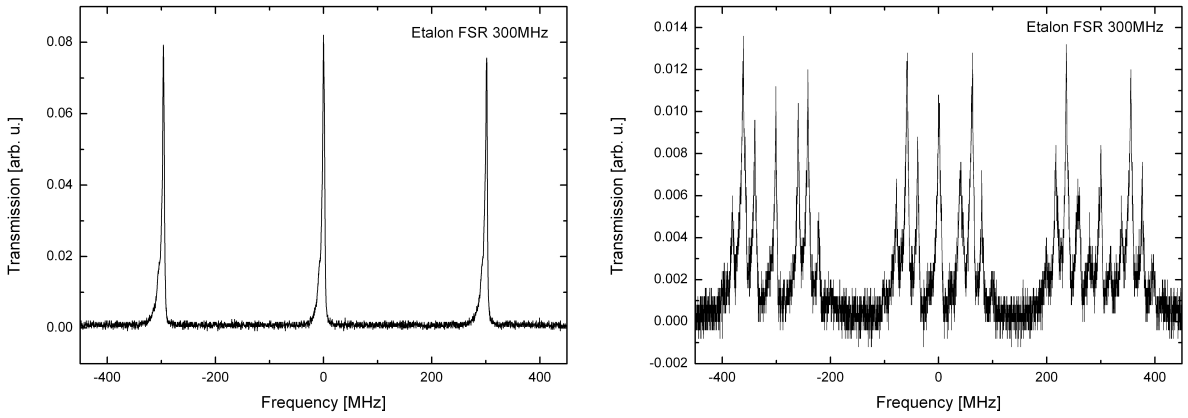

Figure 4.15: Transmission through a Fabry-Perot etalon with the master laser in single- (left) and multi-mode (right).

After securing that the master laser is operating stable and single-mode at the desired wavelength, the conditions for successful injection locking are studied. Since the broad-

area diode laser serves as an amplification medium for the master laser, the amount of locked output power should depend on the injected laser power. The dependence was measured by varying the power of the seeding beam by making use of a polarising beam-splitter (PBS) and a half-wave plate. Figure 4.16 shows the dependence of the output power from the slave laser on the amount of injected power from the master laser. If the injected power from the master laser is zero, only the remaining free-running power from the observed mode is visible.

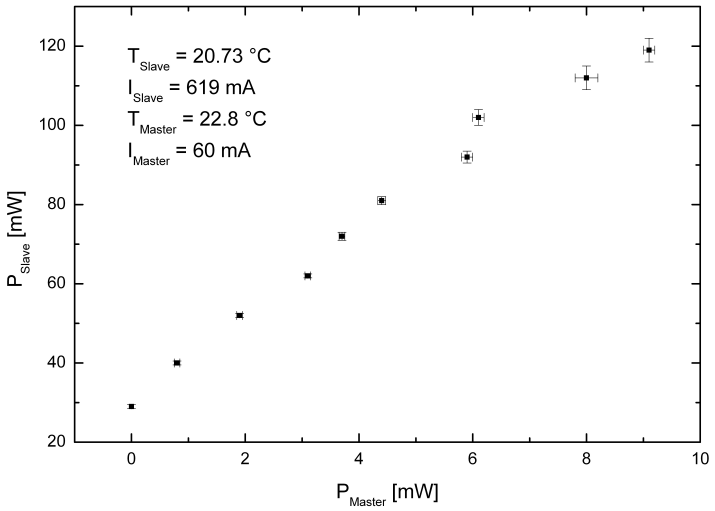

Figure 4.16: Dependence of locked output power from the slave diode on the amount of injected laser power from the master.

Figure 4.16 was obtained for fixed temperature and current of the slave and master diode, respectively. In order to illustrate that the injected wavelength has to fulfil the resonance condition inside the BAL chip for effective injection locking, another measurement was made where only the temperature of the slave diode was varied in small steps. As anticipated, the output power of the slave changes periodically, becoming maximum each time the length of the active medium is an integer number of half wavelengths. This behaviour is clearly visible in Figure 4.17.

The current through a laser diode also affects its temperature. Therefore, a similar behaviour as seen in Figure 4.17 should be obtained if only the current through the slave diode is varied. The result of this measurement is displayed in Figure 4.18 and, indeed, it shows similar minima and maxima as Figure 4.17.

As a result from the proceeding measurements it can be concluded that for efficient injection locking it is desirable to have as much seeding power as possible. Furthermore, the current and temperature of the broad-area diode laser has to be optimised to maximum output into the locked mode. In order to verify that the increase of power really is converted into the amplified mode, one can simply block the seeding beam. When doing so, the power into the observed mode decreases significantly, usually to about 10–20 %.

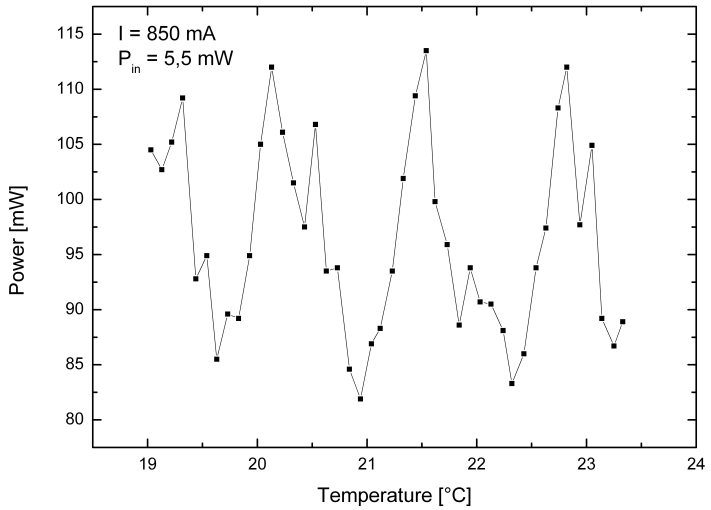

Figure 4.17: Dependence of the output from the injection locked slave diode on the temperature. The periodical variations illustrate where the resonance condition is fulfilled.

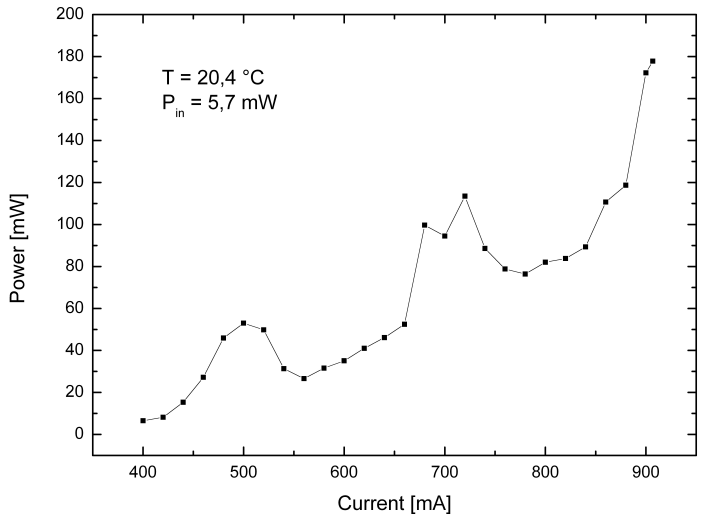

Figure 4.18: Injection locked output power from the slave diode versus applied forward current to the slave. All other parameters are fixed.

To make sure that the spectral characteristics of the master laser are actually transferred to the slave diode, the transmission of the slave's output through a Fabry-Perot interferometer (1.5 GHz FSR) was measured. As displayed in Figure 4.19, the slave spectrum shows a central narrow peak as well as the side-bands which are modulated to the master. When the seeding beam of the master is blocked the narrow peak disappears. Without injection locking the spectrum of the slave diode is very broad (a few nm bandwidth) and cannot be measured with a 1.5 GHz etalon.

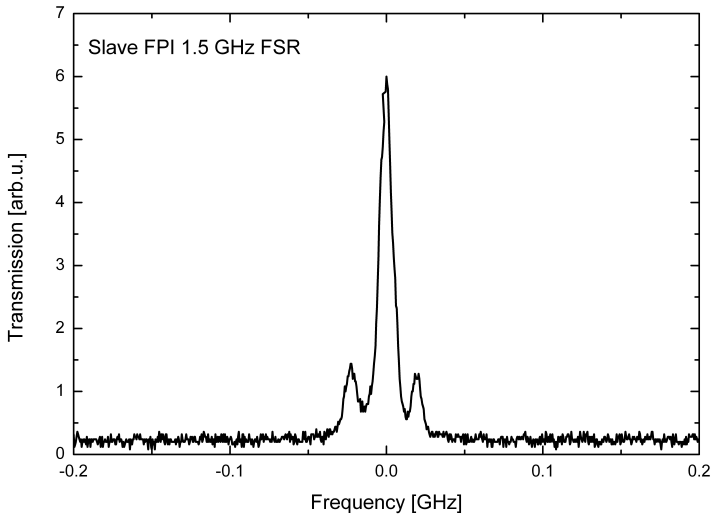

Figure 4.19: Transmission signal of the slave's output through a 1.5 GHz FSR Fabry-Perot etalon showing the 20 MHz side-bands from the master.

The most critical parameter which has to be optimised for injection locking is the alignment of the seeding beam. This can be done by adjusting the mirror which reflects the master beam into the broad-area diode laser and by displacing the cylindrical lens transversal to the beam. Figure 4.20 shows how the locked output depends on proper alignment of the seeding beam. The best way to find the optimum alignment is to start from a BAL current slightly below threshold. When the seeding beam is adjusted such that it couples correctly into the active medium of the BAL, it gets amplified and the output mode "flashes". This procedure is repeated with increasing BAL current until a maximum is reached at about 650 mA in the case of this set-up, giving a locked output power of about 130 mW at an injection power of about 13 mW, thus achieving a gain factor of 10. Especially the vertical adjustment of the seeding beam is very critical and stable injection locking requires good mechanical stability of all optical components. Therefore, the optical path between the master and the slave should be kept as small as possible. Also of great importance is a very stable mounting of the slave laser itself as well as its collimator and the cylindrical lens.

The now available output power of about 130 mW is delivered by a beam which is still very divergent in the x-direction. In order to shape this beam to a Gaussian-like profile it first passes an anamorphic prism pair and is then focussed by a f = 30 mm lens onto a 100 µm pinhole which works as a spatial mode filter. After the pinhole the beam is collimated by a f = 50 mm lens and about 50 mW of laser power is left. Since this is too low to operate both, the magneto-optical trap and the Zeeman slower, a second set-up of master and slave lasers which is identical to the first one is used. Thus, for each frequency which is needed for laser cooling, one master-slave system is available. With both master lasers locked to the crossover resonance which is centred between the two Lamb dips (see Figure 4.9) of the Li D2 line, the two needed frequencies

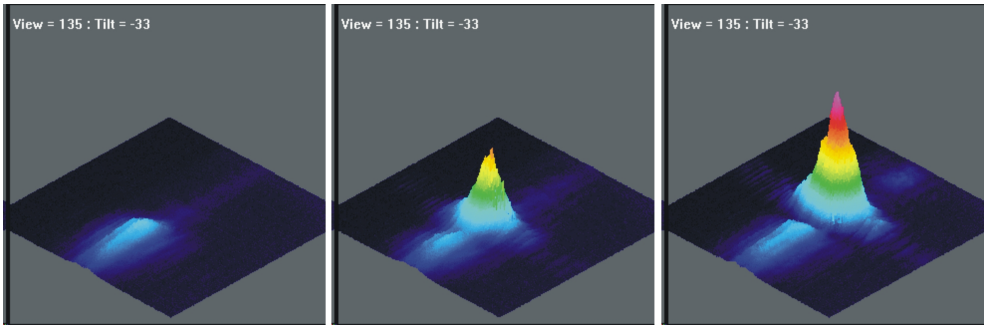

Figure 4.20: CCD camera pictures of the injection locked slave output for no, bad and good alignment of the seeding laser beam.

(trapping laser and repumper) are generated by shifting the individual BAL frequencies by $(\Delta - \delta)$ and $(-\Delta - \delta)$, respectively, using acousto-optic modulators (AOMs). Here Δ is half the hyperfine splitting of the Li ground state (401.7 MHz) and δ is the detuning of the magneto-optical trap (a few linewidths Γ = 2π·5.92 MHz). After generating the two frequencies, both lasers are overlapped at a 50:50 beam-splitter giving two beams that contain the cooling laser and the repumper. The transmission efficiency of the AOMs is about 65 % at maximum (double-pass), thus leaving about 30 mW fo optical power for the MOT and the Zeeman slower for each frequency. The detuning of the Zeeman slower laser is generated by yet another AOM that shifts the frequency by about -100 MHz (double-pass). The described part of the set-up that containes the AOMs is shown in Figure 4.21.

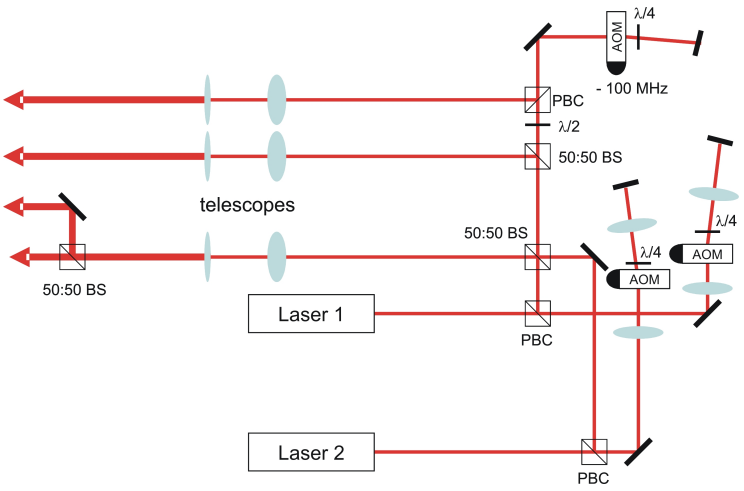

Figure 4.21: Schematic picture of the frequency generating part of the diode laser set-up.

In summary, the possible use of a frequency stabilised compact and cost efficient master-slave diode laser system was successfully demonstrated providing just sufficient laser power for Zeeman slowing and magneto-optical trap ping of lithium atoms. The pre-

sented prototype set-up turned out to provide insufficient mechanical stability, however, leading to unsatisfactory results regarding the long-term stability of injection locking. After about 30 minutes the locked output of the slave was reduced by 50 % and the alignment had to be readjusted. Thus, future improvements of the set-up are in progress, providing a more sophisticated mounting of the BAL and the collimating optics. Meanwhile, in order to quickly progress in realising the MOT and to perform all tests necessary to prove its future use as a target in a reaction microscope, a dye-laser was used instead to provide all laser beams.

4.2 The Dye-Laser System

Dye-lasers use large molecules of organic dyes which are solved in a liquid as an active medium. These molecules have many vibrational and rotational levels in the electronic ground (singulett S_0) and excited state S_1. From the interaction with the solvent, these levels are broadened so much that the width becomes larger than the average energy difference of the levels, so that a broad continuum of states is generated.

The pumping light source excites the molecules from the ground state $|1\rangle$ into many vibrational-rotational levels in the S_1 state. Relaxation into the lowest levels $|2\rangle$ of the S_1 state occurs on a very small time scale of 10^{-10}–10^{-12} s due to collisions with the solvent. From there they can decay into many vibrational-rotational levels $|3\rangle$ of the ground state by fluorescence. Because the higher levels of the S_0 state are not populated at room temperature, population inversion between the state $|2\rangle$ and the levels $|3\rangle$ can be achieved if sufficient pumping power is supplied. Hence, the active medium of a dye-laser is a four-level-system [Dem96] as illustrated in 4.22.

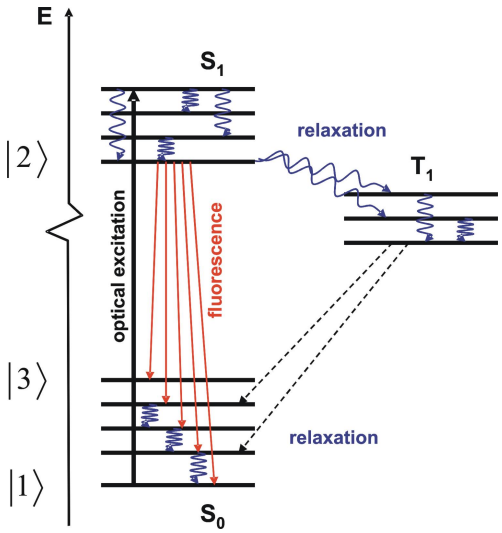

Figure 4.22: Level scheme of a laser dye molecule.

The dye-laser can operate on any wavelength for which the lasing condition is fulfilled. The actual lasing frequency can be set by wavelength selective elements such as a etalons within the resonator and can be tuned by variation of the transmission maxima of the filters over the amplification profile of the laser dye. This can be done for instance by tilting the etalons which are inside the resonator. The tuning range depends on the laser dye which is used. Figure 4.23 shows the tuning ranges of several different laser dyes.

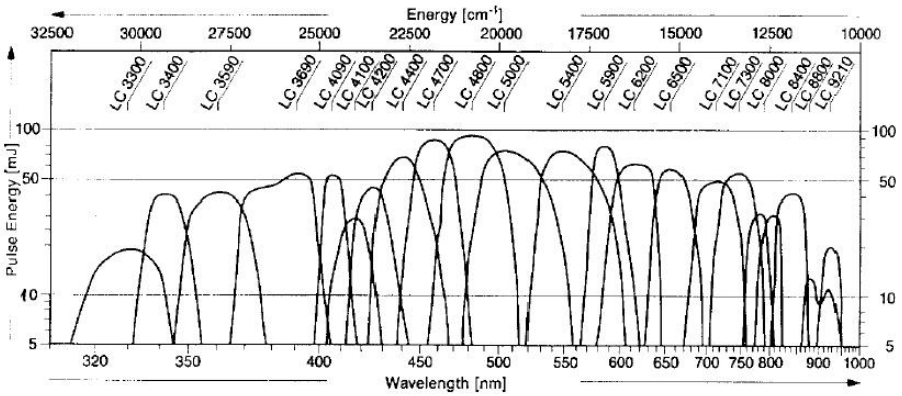

Figure 4.23: Tuning curve for excimer laser pumped dye-lasers. LC 6500 is DCM, LC7100 is Pyridine 1 and LC5900 is Rhodamine 6G.

The dye-laser system used in this work consists of a SPECTRA PHYSICS Millenia pump laser, which is a diode laser pumped Nd:YAG laser that supplies optical pumping power of up to 10 W, frequency doubled to 532 nm (green), and a COHERENT 699 ring dye-laser. At 671 nm (red) the dye of choice is for example DCM (4-dicyanomethylene-2-methyl-6-p-dimethylaminostyryl-4H-pyran). The chemical structure is of DCM displayed in Figure 4.24.

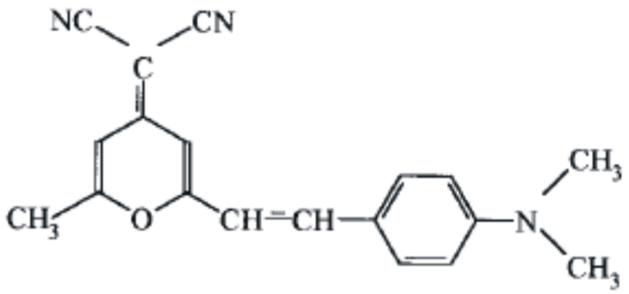

Figure 4.24: Chemical structure of the DCM molecule 4-dicyanomethylene-2-methyl-6-p-dimethylaminostyryl-4H-pyran.

A schematic picture of the working principle of the COHERENT 699 ring dye-laser is shown in Figure 4.25. The pump laser beam is focussed onto the dye-jet bye a concave

mirror. The laser cavity is formed by a set of mirrors which are used to calibrate the resonator. A set of etalons serve as frequency selective elements and make sure that the laser runs on a single mode. Part of the output beam is split off and coupled into a reference cavity to which the laser is locked.

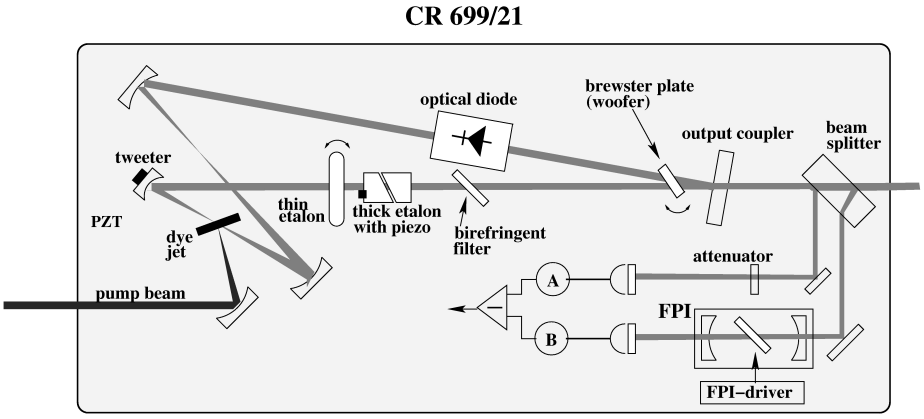

Figure 4.25: Schematic picture of the COHERENT 699 ring dye-laser.

With a pumping power of 8 W an optical output power of 400 mW can be achieved at 671 nm and stable operation over several hours is usual without readjusting the mirrors of the dye-laser resonator. Since the lifetime of the dye, among others, depends on the pumping power, the output of the pump laser is reduced to 6 W if less power from the dye-laser is sufficient for the experiment. At 6 W pumping power an output of about 300 mW is possible which is sufficient to operate the MOT.

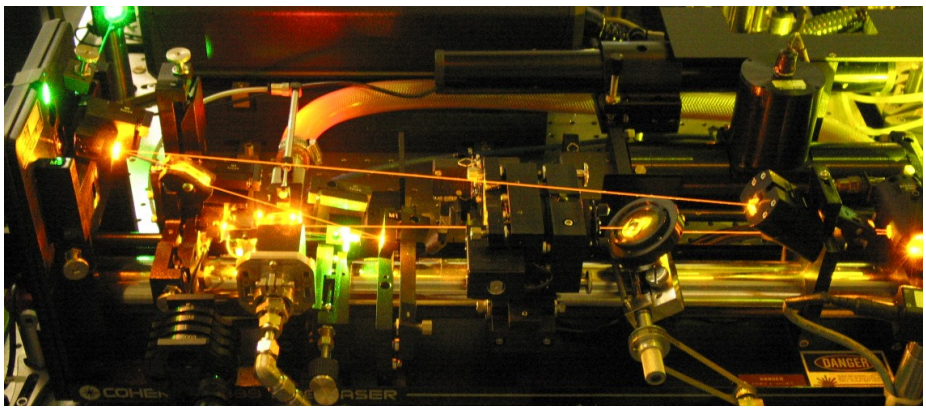

Figure 4.26: Photograph of the COHERENT ring dye-laser.

The main advantages of the dye- with respect to the diode laser system are its high power and excellent beam characteristics. The output is a TEM_{00} mode with a diameter of about 2–3 mm. After a few hours of operation the dye-laser operates very stable once

it is well aligned and it can be run for days with only some small adjustments from time to time. A picture of the COHERENT 699 ring dye-laser is shown in Figure 4.26.

The full set-up of the laser system is displayed schematically in Figure 4.27. About 1 mW of power is split off by a polarising beam-splitter (PBS) into the lithium spectroscopy cell for frequency stabilisation. The rest is divided at another PBC into two beams which are shifted by the AOMs by $(\Delta - \delta)$ and $(-\Delta - \delta)$, respectively. Here, as before, Δ is half the hyperfine splitting of the Li ground state (401.7 MHz) and δ is the detuning for the magneto-optical trap (a few linewidths Γ = 2π·5.92 MHz). The two beams are then overlapped at a 50:50 beam-splitter (BS) to form two beams which contain both frequencies. These beams are further split into four beams of equal intensity, where three are used for the three retro-reflected trapping beams (directions x, y and z). The fourth beam is shifted by another AOM by -100 MHz for the Zeeman slower. The three MOT beams are widened to a diameter of 2 cm by telescopes (f_1 = 50 mm and f_2 = 500 mm).

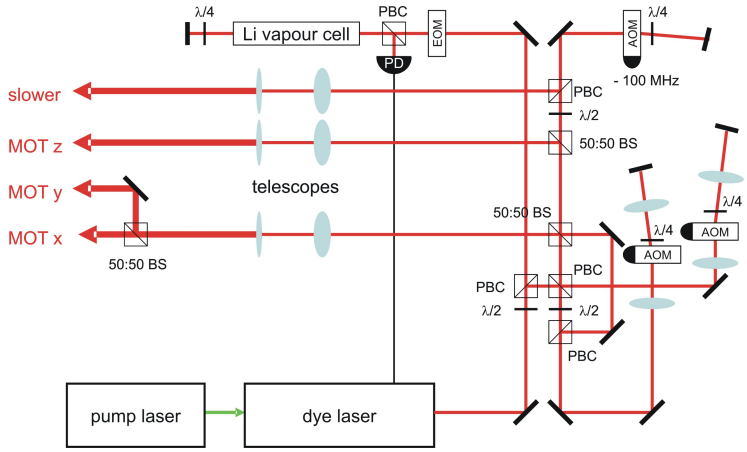

Figure 4.27: Schematic set-up of the dye laser system. BS: beam-splitter, PBC: polarising beam-splitter, λ/2: half-wave plate, λ/4: quarter-wave plate, PD: photo diode, AOM: acousto-optic modulator, EOM: electro-optic modulator.

4.2.1 Frequency Stabilisation

The frequency stabilisation of the dye-laser consists of an internal and an external component. Internally the dye-laser is locked to a single mode of a Fabry-Perot cavity preventing fast variations of the laser frequency. The external frequency stabilisation to the crossover line of the ^{7}Li D2 transition is done in a similar fashion as for the diode laser (by FM-spectroscopy). The most important difference is that the frequency modulation is not created internally but by an electro-optic modulator (EOM) which is placed in front of the spectroscopy cell. The modulation frequency lies between 10 and 20 MHz. The principle of FM-spectroscopy has already been explained in Section 4.1.2.

4.3 Conclusion and Outlook

Since the output power of the here-developed diode laser system was at the lower end for stable MOT operation, and moreover, due to the extraordinary sensibility of the prototype laser to mechanical instabilities, all further experiments were done with the dye-laser, in order to progress quickly with all tests for the MOT within the reaction microscope. In general diode lasers have the advantage of easy handling, high stability and low costs, whereas the dye-laser provides high output power with the minor drawback of having to change the dye every few weeks or months. In summary, on the basis of present commercial diode laser technology, the dye-laser seems to be the favoured solution for the next future.

Alternatively to the here-explored use of multi-mode high-power broad-area diode lasers, injection locking, very similar to grating feedback, also works with single-mode laser diodes. Here however, the light which is fed into the laser diode comes from yet another grating-stabilised diode laser. Such schemes are used in various experiments for magneto-optical trapping of lithium (for example: [Sch94], [Sch96], [Sch97], [Sch98]). Again there, low-cost diode laser systems have the advantage of very stable and easy operation, but the achieved optical power is limited by the output power of the seeded laser diodes which is about 30 mW. Since the single-mode systems provide better beam characteristics and considering that after beam shaping the BAL arrangement presently delivers about 50 mW, the single-mode system certainly represents a competitive low-cost alternative.

Another possibility to amplify light from a diode laser is to use a tapered amplifier (TA). These semi-conductor chips, presently only available for the infra-red, combine the "best of both worlds", namely laser diodes designed for single-mode operation and broad-area emitters. Usually, the power of a single-mode diode is limited by Catastrophic Optical Mirror Damage (COMD) whilst the higher power of a broad-area emitter has the drawback of multiple transverse mode operation. This can be circumvented by using a special lateral geometry, where a single-mode channel ensures operation at the fundamental transverse mode. Furthermore, the power density on the output facet is greatly reduced by diffraction of the beam within a subsequent tapered gain section. TA chips for 671 nm are currently under development and can be expected to become available in the future.

Other possible laser sources at 671 nm are systems that make use of non-linear effects in crystals such as PPKTPs (Periodically Poled KTP crystals). Currently, a collaboration between Gabriele Ferrari at LEOS, Florence, and the University of Innsbruck is developing a laser system which generates 671 nm light from a 1006.5 nm pump laser source as shown in Figure 4.28. In this set-up two PPKTP crystals are used to generate the lithium wavelength. In the first crystal (1) a 1006.5 nm photon is down-converted by a parametric process into two 2013 nm photons. In the second crystal (2) a 1006.5 nm photon combines with a 2013 nm photon to a 671 nm photon. Possible sources for 1006.5 nm would be fibre-amplified diodes, diodes combined with a tapered amplifier or disc lasers.

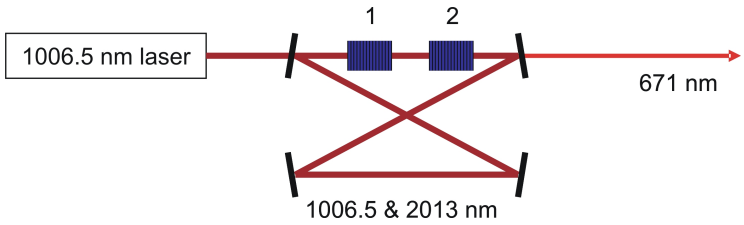

Figure 4.28: Alternative laser source at 671 nm: 1.5 frequency multiplication of a 1006.5 nm laser.

Chapter 5

The Zeeman Slower

In order to load a magneto-optical trap (MOT), it is necessary to have a source of cold atoms, where cold means that they have a velocity smaller than the capture velocity of the MOT which is usually on the order of a few tens of meters per second. All atoms that meet this requirement will be trapped in the MOT once they enter the trapping region. The simplest way to provide a source of lithium atoms is to heat a piece of lithium in an oven or to use a lithium dispenser. The fraction of atoms that can be trapped depends on the temperature of the source and is given by the Maxwell distribution. For typical oven temperatures of 300–400 ℃ the peak of the Maxwell distribution is around 1500 m s^{-1} and, therefore, only a small fraction of the evaporated lithium atoms in the low velocity tail of the distribution can be trapped. Increasing the source temperature certainly yields a higher absolute number of atoms in the low temperature tail as well, but, at the same time, the increasing number of hot atoms will lead to much higher loss rates in the MOT from collisions. Therefore, it would be highly desirable to first cool down the hot evaporated atoms and then being able to trap a large fraction of them.

Several schemes to slow down atomic beams (for example [Pro85], [Rii90], [Ket92] and [And94]) have been published in various articles. The technique which is most commonly used today is the so-called Zeeman slower [Phi82]. Here, an atomic beam from an oven is met by a counter-propagating laser beam which is red detuned. A spatially decreasing magnetic field along the atomic beam propagation is used to compensate for the decreasing Doppler shift (velocity) of the slowed-down atoms by a decreasing Zeeman effect, thus keeping the atoms in resonance over a certain distance by changing the atomic resonance frequency ω_a. The length of the slower and the detuning of the laser beam will determine the maximum velocity of atoms to be decelerated and the final velocity after slowing down. Another possibility to follow the decreasing Doppler shift during the deceleration of the atoms would be to change the laser frequency ω_L accordingly. However, this "chirp" method can only deliver bunches of cooled atoms, whereas the Zeeman method delivers a continuous beam.

5.1 Theory of Zeeman Slowing

In this section the theoretical background for the Zeeman-compensated deceleration of an atomic beam is presented briefly. A more detailed discussion can be found in [Met94], [Met99] and [Phi82].

5.1.1 Equation of Motion

To effectively cool and decelerate atoms, the largest possible stopping force has to be maintained over a substantial part of the slowing distance. This is an important condition for the design of the slower and helps keeping the length small, thus reducing the radial divergence of the atomic beam. From Equation 2.4 follows for strong saturation $s \gg 1$ that the maximum scattering force is

$$F_{max} = \frac{\hbar k \gamma}{2} = \frac{\hbar k}{2\tau}. \tag{5.1}$$

Therefore, the maximum deceleration for a particle of mass m is $a_{max} = F_{max}/m$. Using the equations of motion for constant deceleration

$$z(t) = v_0 t - \frac{1}{2} a t^2 \text{ and } v_z(t) = v_0 - at.$$

the relation between velocity and distance can be derived as

$$v_z(z) = v_0 \sqrt{1 - \frac{z}{z_0}} \tag{5.2}$$

with $z_0 = \frac{v_0^2}{2a}$ being the length of the slowing distance and v_0 the maximum velocity that can be slowed down, i.e. the maximum velocity for atoms being in resonance at the beginning of the slower. Atoms with velocities $v > v_0$ are not affected.

5.1.2 Magnetic Field Gradient

In this section the magnetic field gradient of the Zeeman slower will be determined. Because the velocity of the atoms is changing along the slowing distance, also the Doppler shift and, thus, the necessary Zeeman shift will change. Therefore, the magnetic field has to vary with the velocity of the slowing atoms. In other words, the Zeeman shift $-\Delta\mu B$ has to compensate the Doppler shift $\mathbf{k}\cdot\mathbf{v}$[1] at all times. The equation $-\Delta\mu B = kv$

[1] Since $\mathbf{k}$ and $\mathbf{v}$ are parallel the vector notation will from now on be left away.

is called resonance condition, with $\Delta\mu$ denoting the difference of the magnetic moments of the excited state μ^e and the ground state μ^g.

In order not to slow down the atoms to zero velocity, which would lead to strong radial divergence of the atomic beam and to prevent interaction of the slowing laser with the trapped atoms in the MOT, a detuning of $\delta = \omega - \omega_L$ is added. The modified resonance condition thus becomes

$$kv = -\Delta\mu B + \delta. \tag{5.3}$$

In order to determine the magnetic field gradient of the Zeeman slower, first the Zeeman shifts of the atomic levels have to be calculated. This will be done for the relevant cooling transition of lithium, the D_2 line which is the closed transition between the $2^2S_{1/2}(F = 2),\ m_F = +2$ hyperfine ground state and the $2^2P_{3/2}(F' = 3),\ m_F = +3$ excited state as mentioned in Section 4.

Since already for small magnetic fields of a few Gauss the progression of the excited state is described by the Paschen-Back effect, this state will be described by spin quantum numbers $m_J = +3/2$ and $m_I = +3/2$. The term with the nuclear magnetic moment can be neglected because $\mu_B/\mu_K \approx 1880$, thus leading to the energy shift

$$E_{PB} = -\mu^e \cdot B = \frac{\mu_B}{\hbar} m_J^e g_J^e B$$

where μ_B denotes the Bohr magneton, m_J^e the magnetic quantum number and g_J^e the Landé factor of the excited state. The shift of the ground state level is described for small magnetic fields by the Zeeman effect

$$E_{ZE} = -\mu^g \cdot B = \frac{\mu_B}{\hbar} m_F^g g_F^g B$$

with the ground state magnetic quantum number m_F^g and Landé factor g_F^g. Therefore, the energy shift ΔE of the atomic transition scales linearly with the magnetic field B. For weak fields up to 200 G

$$\Delta E(B) = E_{PB} - E_{ZE} = \frac{\mu_B}{\hbar}(m_J^e g_J^e - m_F^g g_F^g)B = \frac{\mu_B}{\hbar} B. \tag{5.4}$$

Here, the values of the magnetic quantum numbers and Landé factors of the excited and ground state are $m_J^e = 3/2$, $g_J^e = 4/3$, $m_F^g = 2$ and $g_F^g = 1/2$.

For magnetic field strengths of several 100 G, where the transition between the weak and the strong field behaviour takes place, the shift E_{BR} of the ground state energy is described by the Breit-Rabi formula [MK97]

$$E_{BR}(F = I + 1/2, m_F) = \frac{m_F g_K \mu_K B}{\hbar} - \frac{A}{4} + \frac{\Delta E_0}{2}\sqrt{1 + \frac{4m_F}{2I+1}x + x^2}, \tag{5.5}$$

with $x \approx \frac{2\mu_B B}{\hbar \Delta E_0}$, the interval factor $A = 2.79\mu_K B_{e^-}/(\hbar I J)$ (approx. 440 MHz for lithium) and the magnetic field B_{e^-} generated by the electrons at the nucleus. $\Delta E_0 = A(I + 1/2)$ is the energy difference of the hyperfine structure terms at zero external field, I the nuclear spin, m_F the magnetic quantum number of the HFS ground state and g_K and m_K are the nuclear Landé and nuclear magnetic quantum numbers, respectively.

Again, the first term of the Breit-Rabi formula can be neglected due to $\mu_B/\mu_K \approx 1880$. For lithium the nuclear spin is $I = 3/2$ and $m_F = 2$. Therefore the 3rd term in Equation 5.5 can be written as

$$\frac{\Delta E_0}{2}\sqrt{1 + \frac{4m_F}{2I+1}x + x^2} = A\sqrt{1 + 2x + x^2} = A(1 + x) = A + \frac{\mu_B}{\hbar}B.$$

Thus, the simplified Breit-Rabi formula becomes

$$E_{BR}(F = 2, m_F = 2) \approx \frac{3}{4}A + \frac{\mu_B}{\hbar}B.$$

The relative energy shift of the ground state scales linearly with the magnetic field B. Using this result the same dependence on the magnetic field is obtained for the energy shift of the atomic transition in case of strong fields

$$\Delta E(B) = E_{PB} - E_{BR} = \frac{\mu_B}{\hbar}(m_J^e g_J^e - 1)B = \frac{\mu_B}{\hbar}B \tag{5.6}$$

with $(m_J^e g_J^e - 1) = 1$. The resonance condition can then be written as

$$kv = \frac{\mu_B}{\hbar}B + \delta. \tag{5.7}$$

With Equation 5.2 the expression for the required magnetic field gradient is

$$B_z(z) = B_{off} + B_0\sqrt{1 - \frac{z}{z_0}} \tag{5.8}$$

$$\text{with } B_{off} = \frac{\hbar\delta}{\mu_B} \text{ and } B_0 = \frac{\hbar k}{\mu_B}v_0. \tag{5.9}$$

The magnetic field therefore has a square root shaped profile, which is shown in Figure 5.1. An offset field B_{off} is necessary because of the detuning of the slowing laser.

The deceleration a and, therefore also, the force F on the atom depends on the absolute magnetic field strength $B(z)$, the field gradient $\partial B(z)/\partial z$ and the detuning δ. This can be shown by calculating the deceleration of an atom in direction of z from the resonance condition 5.7.

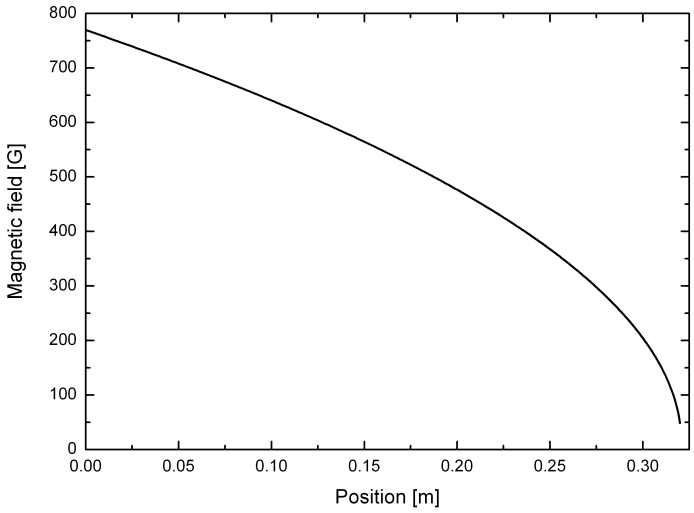

Figure 5.1: The magnetic field needed to slow and cool down atoms in a Zeeman slower. The field is calculated from Equation 5.8 with a detuning δ = 100 MHz, a maximum initial velocity v_0 = 712 m s^{-1} and a slowing distance z_0 = 0.32 m.

$$\begin{aligned} a &= \frac{dv_z}{dt} = \frac{\partial v_z}{\partial z}\frac{\partial z}{\partial t} \\ &= \frac{\mu_B}{\hbar k}\frac{\partial B}{\partial z}v_z \qquad \text{with } v_z = \frac{\partial z}{\partial t} \\ &= \left(\frac{\mu_B}{\hbar k}\right)^2 \frac{\partial B}{\partial z}B + \frac{\mu_B}{\hbar k^2}\frac{\partial B}{\partial z}\delta. \end{aligned} \tag{5.10}$$

From this equation it can be seen that the slower can be designed only for *one* atomic transition. Other transitions have different magnetic quantum numbers and Landé factors and, therefore, require different field gradients. Experimentally, this means that the atoms in the $2^2S_{1/2}, (F = 1)$ ground state are not decelerated [Eng97].

5.2 Design and Simulation

In this subsection the design parameters of a Zeeman slower will be discussed and the chosen design in the presented experiment will be justified. Some features of the design are chosen for physical, some for practical reasons and some for both.

5.2.1 Length

The important parameters that can be chosen and which will determine the design of the slower are basically the maximum velocity v_0 to be slowed and the final velocity v_f with which the atoms will leave the slower. Together with the given deceleration they will define the length of the slowing distance via the relation

$$L = \frac{v_0^2 - v_f^2}{2a}. \tag{5.11}$$

The deceleration $a = \eta \cdot a_{max}$ is assumed to be the maximum deceleration times a design parameter $\eta \approx 0.5$ which accounts for irregularities in the slowing field and allows for less deceleration than theoretically possible. Equation 5.11 may lead to the idea that, in principle, all atoms could be slowed down to trappable velocities if only the length of the slower is increased. However, this is not entirely true because slowing will only work in one dimension and will not affect the radial velocity v_r of the atoms. Therefore, it is desirable to build the slower short enough so that not too many atoms will be lost by colliding with the walls or just by drifting out of the MOT radius after leaving the slowing distance. Also it is practical to have a short slower design because it will save material and space in the laboratory.

One way to assess a reasonable length of the slower is to calculate the maximum radial velocity v_r^{max} at which the slowed atoms will still reach the trapping region of the MOT, assuming that this v_r^{max} is smaller than the capture velocity of the magneto-optical trap. That this assumption holds can be shown by estimating the value of v_r^{max}. For a capture radius of r_{cap} = 1 cm and a time $t \geq 0.03$ s, the maximum radial velocity v_r^{max} becomes 0.3 m s^{-1} which is smaller than the capture velocity. From v_r^{max} the rate of trappable atoms can be calculated and evaluated as a function of the length of the slower.

From simple kinematics it follows that the maximal radial velocity is

$$v_r^{max} = \frac{r_{cap}}{t_{OS} + t_{ZS} + t_{MOT}}, \tag{5.12}$$

where t_i are the trajectory times the atoms need to travel from the (O)ven to the (S)lower, inside the (Z)eeman (S)lower and from the end of the slower to the (MOT). Each of these times depend on the atoms' velocity and the distance they have to travel at that velocity. Specifically,

$$t_{OS} = \frac{d_{OS}}{v_0},\ t_{ZS} = \frac{v_0 - v_f}{a},\ t_{MOT} = \frac{d_{MOT}}{v_f},$$

where d_{OS} is the distance of the lithium oven to the slower and d_{MOT} is the distance from the slower to the trapping region. In the presented set-up d_{OS} = 157.4 mm and

d_{MOT} = 333 mm. Since the atoms will be much faster before the slower ($\bar{v}(T$ = 700 K)$\approx$ 1455 m s^{-1})), d_{OS} will not contribute substantially to the divergence of the atomic beam whereas d_{MOT} will have great influence since the longitudinal velocity will be very small ($v_f \approx$ 10 m s^{-1}).

The resulting expression for v_r^{max} then becomes

$$v_r^{max} = \frac{r_{cap}}{\frac{d_{OS}}{\sqrt{v_f^2+2aL}} + \frac{\sqrt{v_f^2+2aL}-v_f}{a} + \frac{d_{MOT}}{v_f}}, \tag{5.13}$$

where the $\sqrt{v_f^2 + 2aL}$ terms are simply v_0 obtained by rearranging 5.11.

With the expressions for v_r^{max} and v_0 in terms of L and the flux $\dot{N}$ of atoms calculated in Chapter 6, the MOT loading rate (i.e. the rate of slow atoms at the MOT) can be obtained as a function of the slower length L:

$$R = \dot{N}\left(1 - \exp\left[\frac{-v_0^2}{v_p^2}\right]\right)\left(1 - \exp\left(\frac{-v_{r_{max}}^2}{v_p^2}\right]\right), \tag{5.14}$$

where $v_p = \sqrt{(2k_BT/M)}$ is the most probable thermal velocity. In Figure 5.2 the dependence of the loading rate on the slower length for d_{OS} = 157.4 mm and d_{MOT} = 333 mm and the dependence on the distance from the end of the slower to the MOT for a slower length L = 0.32 m is shown. The atom flux was $\dot{N}$ = 1.045·10^{15} s^{-1} at an oven temperature of 700 K and a capture radius of 1 cm.

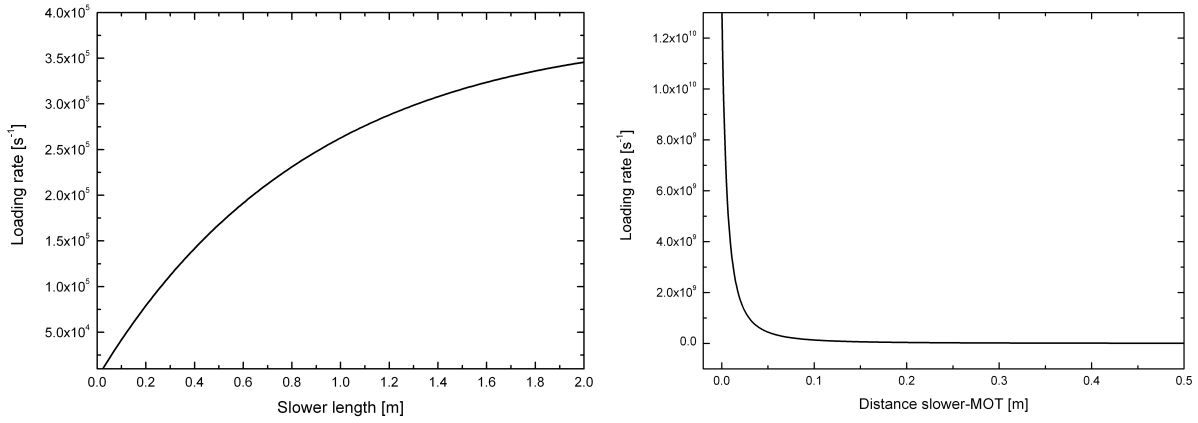

Figure 5.2: Left: trap loading rate R as a function of slower length L with d_{OS} = 157.4 mm and d_{MOT} = 333 mm. Reasonable loading rates can already be obtained for $L \leq$ 1 m. Right: trap loading rate as a function of the distance from the end of the slower to the MOT for L = 0.32 m. The rate could be increased dramatically for shorter distances from the slower to the MOT.

Figure 5.2 shows that the loading rate drops with smaller values of L. However, even for $L \approx 0.3$ m the loading rate is only about a factor three smaller than for L = 2 m. Therefore, it seems feasible to choose a compact design for the slower while still obtaining adequate loading rates. A significant increase of the loading rate could be achieved by shortening the distance from the slower to the MOT. However, this is only possible by having a slower that is partially inside the vacuum chamber which is not possible for the present design but should be considered if the loading rate has to be increased.

5.2.2 Magnetic Field Coils

As explained in Section 5.1.2 the Zeeman slower needs a decreasing magnetic field which is of a square root shape. The technical realisation can be accomplished in two different ways. Either by coiling the copper wire onto the supporting beam tube with a decreasing number of windings according to the desired field gradient or by using a number of individual sections to which different currents are applied such that the sum of the fields is approximately the desired one.

The advantage of the first method is that only one power supply is needed and that the resulting field can be very close to the theoretical one, depending on the accuracy of the winding. However, this is not easy to realise since it is very difficult to wind a single wire according to the desired field gradient. Furthermore, with increasing length of wire to be wound, a single error or material defect would mean that the whole taper has to be built again.

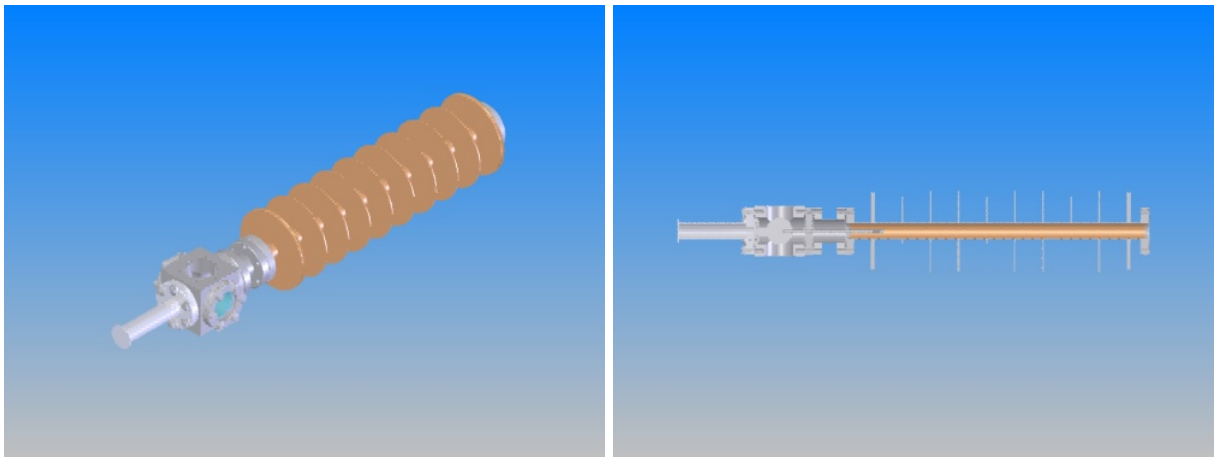

Figure 5.3: CAD-drawing of the Zeeman slower generated with SolidWorks.

The chosen method for this experiment is to emulate a decreasing field by using nine 4 cm long sections of 1.6 mm copper wire coils separated by 2 mm copper discs for air cooling. At both ends the copper discs are 6 mm think and water cooled. The body

is made of a 25×1 mm copper tube with high heat conductivity. The overall length including the cooling discs measures to 388 mm. In the following the longitudinal dimension of the slower will be called z, where z = 0 mm will be just after the first cooling disc. The nine coils are numbered from 0 to 8. Figure 5.3 shows a 3D CAD-image of the slower with the oven. A photograph of the assembled slower is shown in Figure 5.4. The workshop drawing of the slower (Figure C.1) can be found in Appendix C.

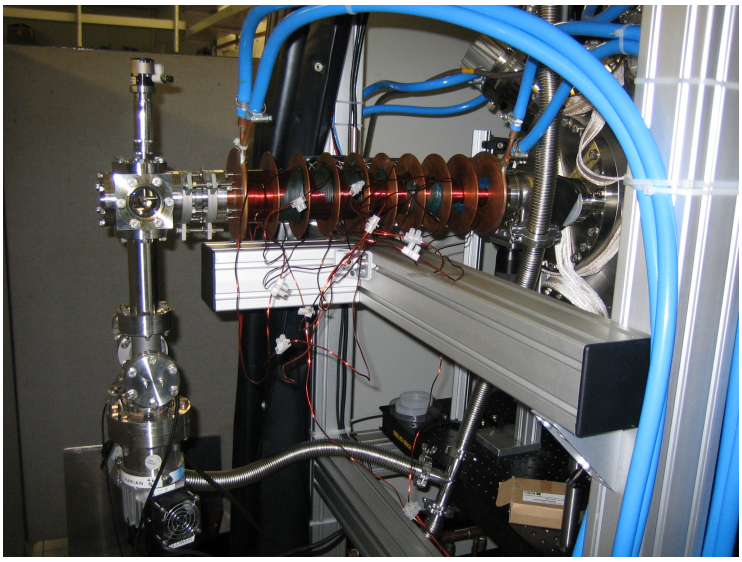

Figure 5.4: Photograph of the Zeeman slower. The atomic oven is not yet connected to the CF35 cube.

In order to develop the layout of the slower and to determine the currents needed for each coil, simulations were performed using the software package MATHEMATICA [Har03]. In the simulation the field of an individual coil is approximated as the sum of single loops of wire, each with different positions z and radii r. The sum magnetic field is evaluated by increasing r and z by the thickness of the wire (1.6 mm), respectively. The field of a single loop can be calculated from the law of Biot-Savart

$$B_z = \frac{\mu_0}{4\pi} \frac{2\pi r^2 I}{(z^2 + r^2)^{3/2}}, \tag{5.15}$$

where μ_0 is the permeability of free space, r is the radius of the current loop, I the current and z the longitudinal coordinate.

The sum of the fields is then adapted to the magnetic field shown in Figure 5.1 by a non-linear regression with the currents as the fit parameter. The result of this procedure is shown in Figure 5.5.

The field which results from the sum of the nine coils comes very close to the ideal square root shaped field gradient. Small variations result from the gaps between each

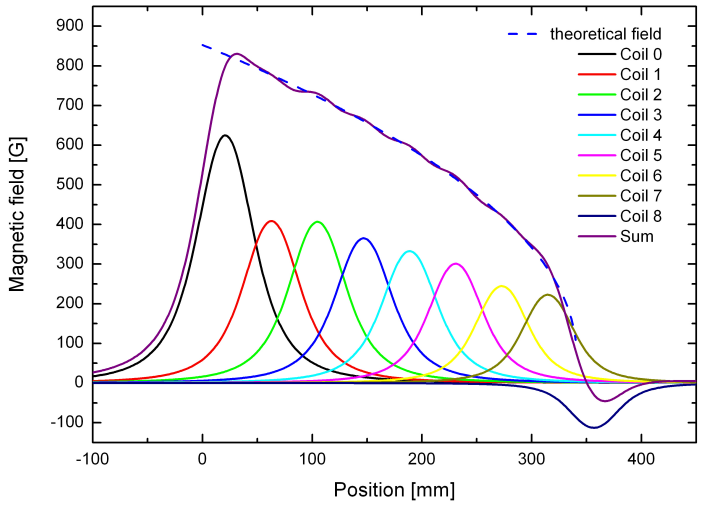

Figure 5.5: Simulated fields of the nine coils and comparison of the sum field to the theoretical field gradient.

section where the cooling discs are located and the fact that the number of windings per length of the slower changes not continuously but in nine steps. However, these small variations are accounted for by the introduction of the design parameter η.

The parameters of the nine coils and the resulting best-fit currents are summarised in Table 5.1. Table 5.2 summarises the dimensions of the Zeeman slower.

Table 5.1: Number of windings and currents of the simulated coils

Coil	Number of windings (z)	Number of windings (r)	Current [A]
0	23	15	10.14
1	23	15	6.52
2	23	15	6.49
3	23	15	5.81
4	23	13	5.88
5	23	11	6.11
6	23	9	5.72
7	23	7	6.66
8	23	5	-0.53

5.3 Performance

In this section the performance of the slower is presented. First, the experimentally determined magnetic field produced by the nine coils is compared to the simulation.

Table 5.2: Some dimensions and numbers of the Zeeman slower

Name	Value
Number of sections	9
Length of sections	40 mm
Outer tube diameter	25 mm
Inner tube diameter	23 mm
Diameter of wire	1.6 mm
Air cooling discs	8
Water cooled discs	2
Diameter of cooling discs	120 mm

Direct measurements of the changed velocity distribution in the atomic beam were not performed. However, from the change of the MOT loading rate the effect of the slower can be investigated qualitatively in the future. A detailed description of how the velocity distribution of a Zeeman slowed atomic beam can be measured is given in [Mol97].

5.3.1 Measurement of the Field

The magnetic field created by the coils is measured separately for each section with an axial hall probe which can be positioned with an accuracy of about 1 mm. All measurements are done for a current of 10 A. A first measurement (Figure 5.6) shows that the axial magnetic field indeed has a linear dependence on the current such that the measurements done at 10 A can be scaled to the ideal currents determined by the simulation. The resulting total field can then be obtained by summing up the individual fields multiplied by the correct current.

The measured fields of all nine coils with a current of 10 A are shown in Figure 5.7. Also shown are the results obtained from the MATHEMATICA simulation which are scaled to meet the peaks of the experimental values for better comparison. Obviously, the measured fields differ significantly from the simulated ones near the edges of the profiles where the fields are quite small. A scaling factor of 1.4 for simulated fields at a current of 10 A is used to match the measurements.

Since the width and, therefore, the area below the curves of the real fields is smaller, the values for the optimum currents from the simulation would not give the right total field. In order to find the best values to be applied to the real coils, the measured fields are fitted (ORIGIN) with Voigt profiles which describe the measurements very well. In Figure 5.8 the measured fields and the Voigt fits are shown for all coils.

The Voigt fits gave the parameters of the curves which are the Gaussian width w_G, the Lorentzian width w_L, the position of the centre x_C, the offset y_0 and the area A. These fit parameters were used in the second step where the sum of the nine coils was fitted with a multiple Voigt profile. The script and the function that approximates the Voigt profile

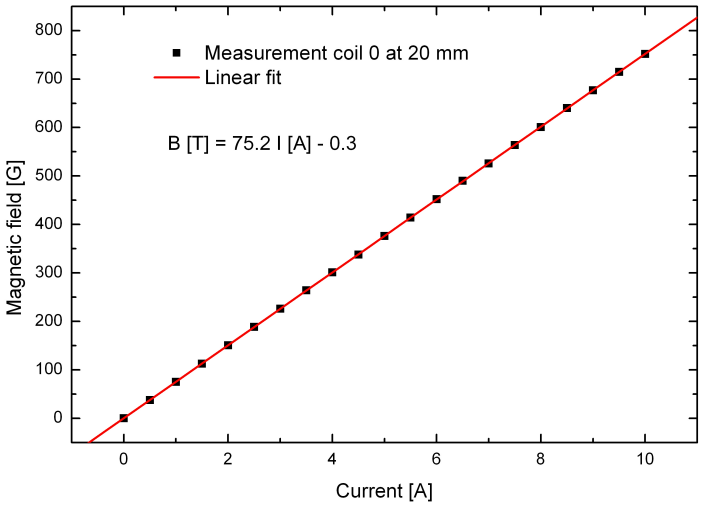

Figure 5.6: Test of linearity of the axial magnetic field generated by one section.

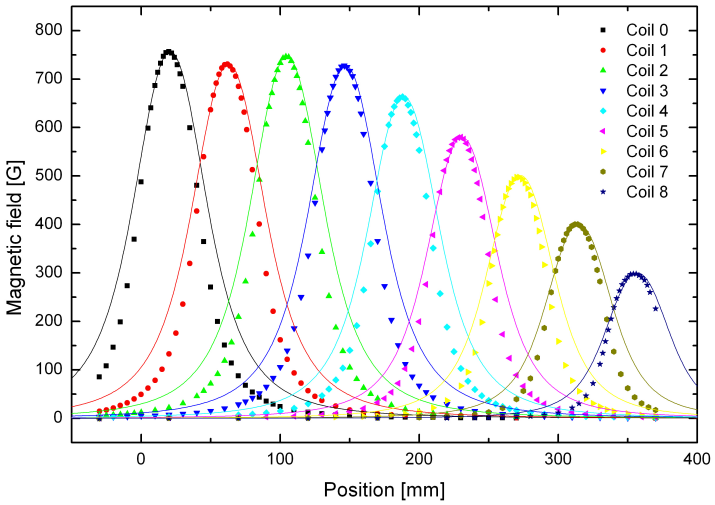

Figure 5.7: Measured fields (dots) and simulated fields (solid curves) of the nine coils at 10 A. Significant differences can be found at the edges of the field profiles.

were kindly provided by Antonio Javier González Martínez [Gon05] based on [Hum79] and [Sch02]. The result of the multiple Voigt fit is shown in Figure 5.9 and compared to the sum of the single Voigt profiles from Figure 5.8.

The resulting parameters from this fit were used for the next step were the best currents were found by only varying a current factor to the area A. This way a multiple Voigt profile with the characteristics of the real coils was fitted to the ideal magnetic field gradient. The result of this last step is displayed in Figure 5.10.

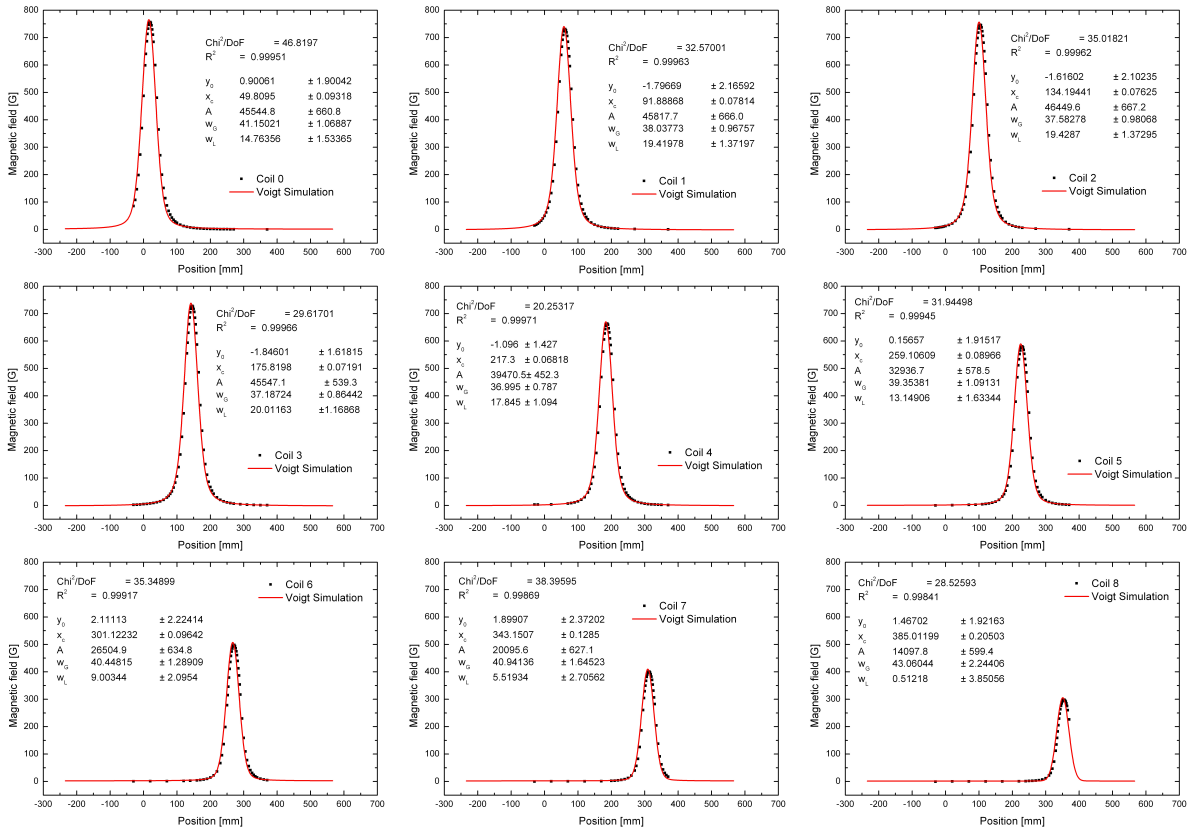

Figure 5.8: Measured fields of the nine coils fitted by Voigt profiles.

From this fit the currents for best approximation to the theoretical field followed as

$$
\begin{aligned}
I_0 &= 9.68 \text{ A} \\
I_1 &= 7.46 \text{ A} \\
I_2 &= 6.98 \text{ A} \\
I_3 &= 6.47 \text{ A} \\
I_4 &= 6.50 \text{ A} \\
I_5 &= 6.77 \text{ A} \\
I_6 &= 6.42 \text{ A} \\
I_7 &= 6.65 \text{ A} \\
I_8 &= -2.11 \text{ A}
\end{aligned}
\tag{5.16}
$$

These currents are still theoretical values that follow from the fitting procedure. They will serve as the starting point for further optimisation once the Zeeman slower is in use.

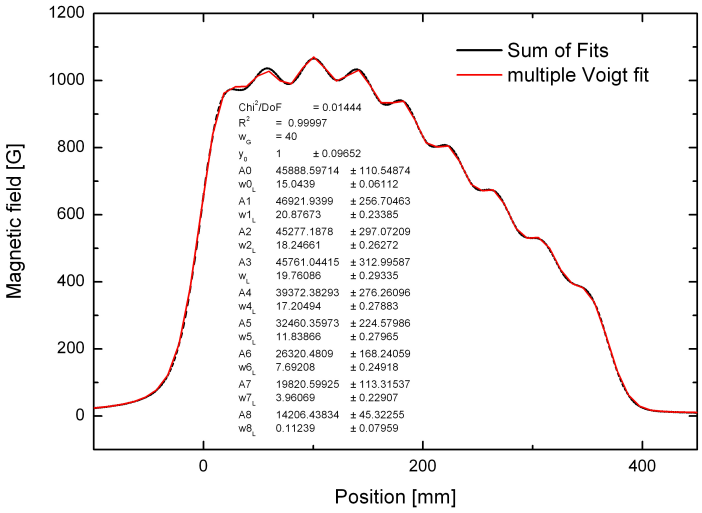

Figure 5.9: Multiple Voigt fit to the sum of the single Voigt profiles.

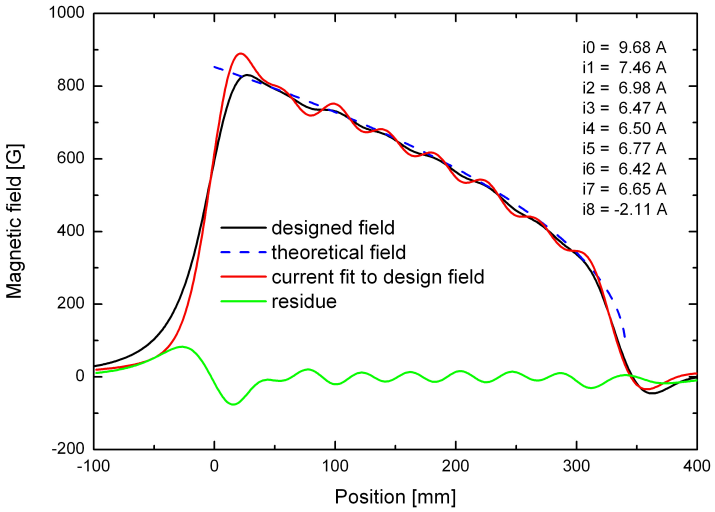

Figure 5.10: Final fit of multiple Voigt profiles to determine the currents needed to achieve the best possible magnetic field gradient.

Then, the currents of the nine coils can still be changed individually, optimising for best loading rate of the magneto-optical trap.

Figure 5.10 shows that the variations of the final field are significantly greater than those from the simulated one. The reason for this is of course that the actual field profiles from the individual coils are narrower than the simulated fields. If these variations disturb the slowing process and if the design parameter η was chosen small enough will be verified once the slower is used to load the trap.

Chapter 6

Properties of the Atomic Beam

In this chapter the properties of a lithium atomic beam coming from an oven will be presented. The calculations will allow to assess the number and velocities of atoms that will leave the oven and the flux of atoms that will reach the trapping region inside the vacuum chamber.

6.1 Lithium Oven

The source of the atomic beam is a simple lithium oven that is made up of a steel tube which is welded to a CF35 flange and that can be heated by a current through a bifilar wire that is wound around the steel tube. Screwed to the oven is a heated nozzle with an aperture of 1 mm. This oven assembly which is shown in Figure 6.1 is then flanged to a CF35 cube using special CABURN nickel gaskets that can endure high temperatures up to 400 ℃. The technical drawing C.2 of the oven can be found in Appendix C.

Opposite the oven a 146 mm differential pumping tube with 4 mm aperture attached to a double sided CF35 flange is mounted to the cube and is followed by an adjustable bellow which then is mounted to the Zeeman slower. To the bottom port of the cube a CF35 4-way cross is mounted which connects to a VARIAN turbo pump, a vacuum gauge and the electric feed-through for the nozzle heating. From the top port a magnetic rotary feed-through which is pneumatically actuated is mounted to the cube and serves as a shutter for the atomic beam. To the remaining two horizontal openings of the cube viewports are mounted that allow to monitor the alignment of the slowing laser to the oven nozzle and to check the status of the shutter.

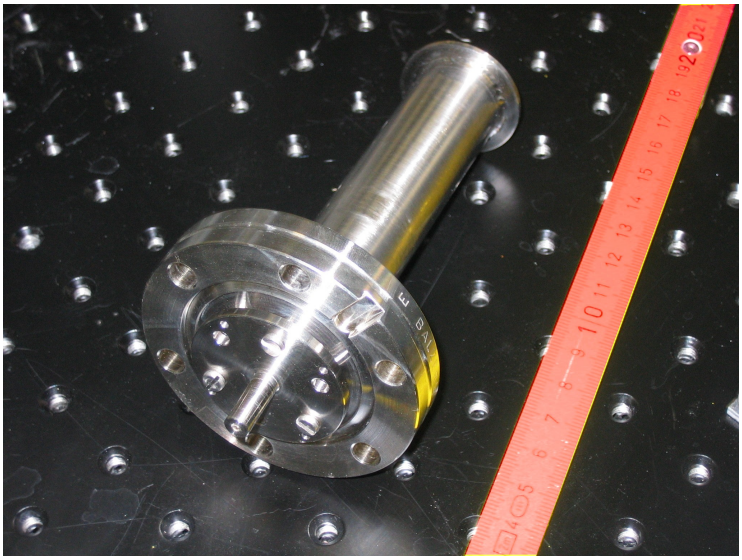

Figure 6.1: Image of the lithium oven with the mounted nozzle without heating.

6.2 Vapour Pressure

Inside the oven a piece of solid lithium is evaporated at a temperature of approximately 500–700 K (melting point of lithium: 453.69 K). These high temperatures are necessary due to the low vapour pressure of lithium. A formula to calculate the vapour pressure of alkali metals (in mm Hg = Torr) is given in [Nes63]

$$\lg p_v = A - \frac{B}{T} + CT + D \lg T, \tag{6.1}$$

where the coefficients for lithium are

$$\begin{aligned} A &= 10.3454 \\ B &= 8345.574 \\ C &= -0.0000884 \\ D &= -0.68106 \end{aligned}$$

The vapour pressure of lithium at 700 K therefore is p_v(700 K) = 0.0002652 Torr = 0.0003536 mbar (1 Torr = 1.333 mbar). Figure 6.2 shows the vapour pressure of lithium.

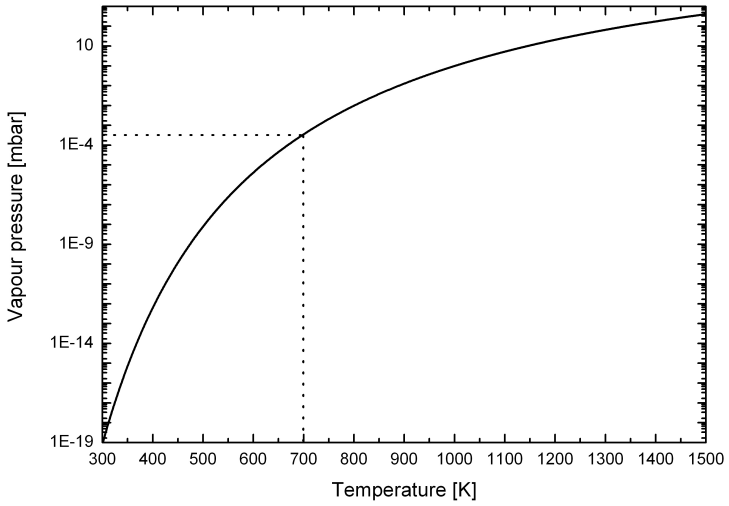

Figure 6.2: Vapour pressure of lithium calculated from Equation 6.1. At 700 K the vapour pressure of lithium is $3.54{\cdot}10^{-4}$ mbar.

6.3 Atom Flux

Using the ideal gas law for a Maxwell-Boltzmann distributed atomic vapour the number density of atoms is

$$n_0 = \frac{p_v}{k_B T} = 7.243 \cdot 10^{22} \frac{p_v[mbar]}{T[K]} \text{ atoms/m}^3. \tag{6.2}$$

At a temperature of 700 K this gives n_0 = $3.658{\cdot}10^{18}$ atoms/m^3. From the number density of atoms and the collisional cross section of lithium σ_c = $7.6{\cdot}10^{-16}$ cm^2 [Väl77] the mean free path λ_A of the atoms can be derived using [Väl77]

$$\lambda_A = \frac{1}{\sqrt{2}\sigma_c n_0}. \tag{6.3}$$

Again, for a temperature of 700 K this gives λ_A = 2.453 m which is much bigger than the length l = 15 mm of the nozzle (Knudsen number $K = \lambda_A/l \gg 1$ [Sco88]). This means that only wall collisions occur and the atomic flow is free. The channel (nozzle) is said to be transparent and its geometry determines the atomic flow properties. In contrast to a thin-walled orifice, a channel of length l increases the probability for the atoms to leave the oven in forward direction. The dependence of the beam profile on $\beta = 2r/l$ where r is the radius of the nozzle's aperture can be found in [Sco88]. For a nozzle of length l = 15 mm and aperture r = 0.5 mm the value of β is 0.13 and, therefore, the atomic beam is collimated to $\leq 5°$. Since the angle $\theta = \arctan(r_{cap}/L_{tot})$ = 0.652°, with the capture

radius r_{cap} and total distance from oven to the trap l_{tot}, into which atoms can be emitted and still reach the trapping region (Figure 6.4) is much smaller than 5° the nozzle does not affect the flux at the capture region, but decreases the number of "useless" atoms emitted into the vacuum chamber at larger angles.

The total flux of atoms evaporated from a sample of lithium inside the oven is given by [Sco88]

$$\Phi = \frac{1}{4} n_0 \bar{v}. \tag{6.4}$$

With an average thermal velocity $\bar{v} = \sqrt{8k_B T/(\pi M)}$ of 1455 m s^{-1} at T = 700 K the total Flux is Φ = 1.331·10^{21} atoms m^{-2}s^{-1}. The flux Φ is not to be confused with the angle ϕ. The number of atoms per second leaving the oven through an opening with an aperture area of A_s = 0.7854 mm^2 is

$$\dot{N} = \Phi A_s = \frac{1}{4} n_0 \bar{v} A_s = 1.045 \cdot 10^{15} \text{ atoms/s}. \tag{6.5}$$

This number gives a theoretical oven lifetime of 1359 years when filled with 5 g of lithium.

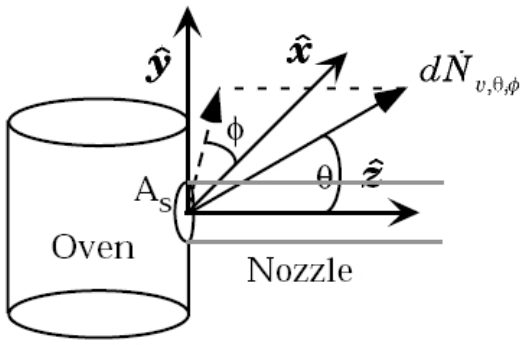

Figure 6.3: Number of atoms leaving the oven at speed v and direction (θ, ϕ) taken from [Sav98].

Figure 6.3 schematically shows how the atoms are leaving the oven. To calculate which fraction of $\dot{N}$ is emitted into the MOT region, the formula [Sco88]

$$d\dot{N}_{v,\theta,\phi} = \frac{n_0 A_s}{\pi^{3/2} v_p^3} v e^{-v^2/v_p^2} \cos\theta v^2 \sin\theta dv d\theta d\phi \tag{6.6}$$

has to be integrated. Here, v_p denotes the most probable thermal velocity and v_r the radial velocity of the atoms. To match the symmetry of the problem Equation 6.6 is transformed to cylindrical coordinates and integrated over ϕ

$$d\dot{N}_{v_r,v_z} = \frac{2n_0 A_s}{\pi^{1/2} v_p^3} v_r e^{-v_r^2/v_p^2} v_z e^{-v_z^2/v_p^2} dv_r dv_z \tag{6.7}$$

In order to integrate this expression the appropriate limits have to be considered. To get the number of atoms per second at the MOT with trappable velocities, the maximal velocity v_0 which can be slowed by the Zeeman slower has to be taken into account. Therefore, Equation 6.7 has to be integrated in the range $0 \leq v_z \leq v_0$. The limit of v_r depends on the capture velocity of the MOT (given by Equation 5.12) and on the geometric collimation limit. The atoms' trajectories are schematically plotted in Figure 6.4.

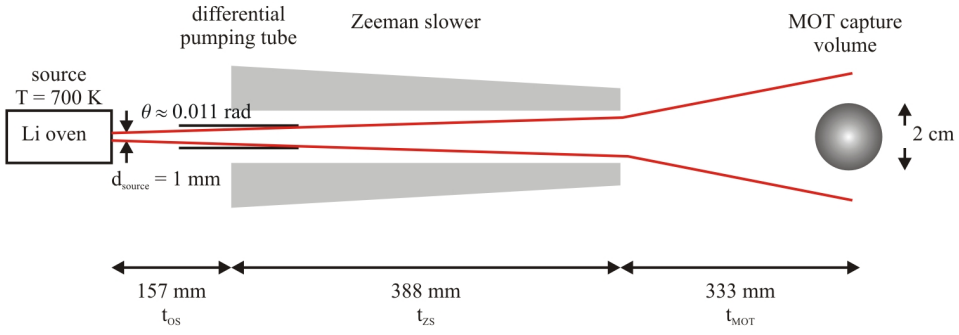

Figure 6.4: Atom trajectories from the oven to the trapping region for the slower geometry of the present set-up.

Integration of 6.7 gives Equation 5.14 which is used in Section 5.2.1 to calculate the rate of trappable atoms at the MOT

$$R = \dot{N} \left(1 - \exp\left[\frac{-v_0^2}{v_p^2}\right]\right) \left(1 - \exp\left(\frac{-v_{r_{max}}^2}{v_p^2}\right]\right).$$

6.4 Atomic Beam Broadening

In this section the mechanisms of atomic beam broadening will be discussed and the flux of atoms is calculated using a different approach than in the previous section.

6.4.1 Flux of Atoms from the Oven

The number of atoms $d\Phi_0$, that are emitted at an angle ϑ to the normal of the opening of the oven into a solid angle $d\Omega$ per second is given by [Ram56]

$$d\Phi_0 = \left(\frac{d\Omega}{4\pi}\right) n_0 \bar{v} A_s \cos\vartheta. \tag{6.8}$$

With $d\Omega = 2\pi \sin\vartheta d\vartheta$ and $A_s = \pi r_s^2$ the total flux of atoms of temperature T emitted into a cone with the opening angle θ is

$$\Phi_0 = \int_0^{\vartheta=\theta} d\Phi_0 = \sqrt{\frac{2\pi}{M k_B T}} \frac{r_s^2}{2} p_v(T) \sin^2\theta. \tag{6.9}$$

For an aperture of radius r_s = 0.5 mm and a temperature of T = 700 K the total flux into an angle θ = 11.39 mrad is Φ_0 = 1.356·10^{11} atoms/s. The velocity distribution of the emitted atoms is described by a modified Maxwell-Boltzmann distribution [Ram56]

$$f_{beam}(v) = 2\left(\frac{M}{2k_B T}\right) v^3 \exp\left[-\frac{Mv^2}{2k_B T}\right], \tag{6.10}$$

where v denotes the velocity of the atoms in direction of beam propagation. Figure 6.5 shows the modified Maxwell-Boltzmann distribution for T = 700 K.

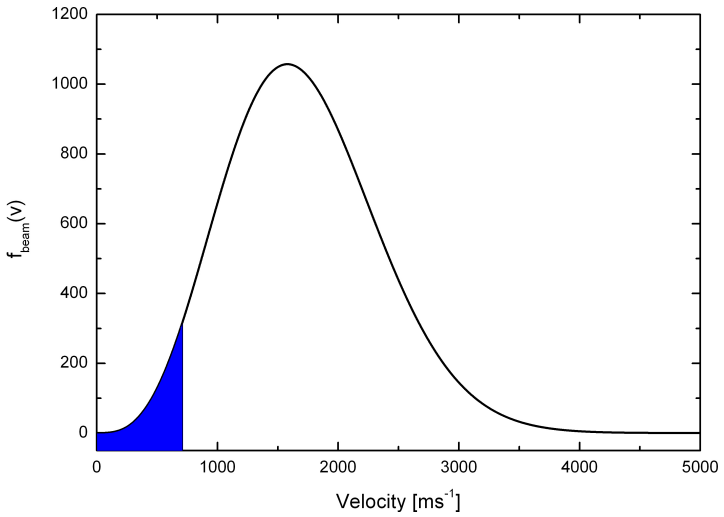

Figure 6.5: Modified Maxwell-Boltzmann distribution for T = 700 K. Marked blue is the area of velocities $v \leq 712$ m s^{-1}.

6.4.2 Loss Factors

The flux of trappable atoms is smaller than the total flux Φ_0 of atoms emitted from the oven. Three loss factors have to be considered:

1. **Isotope factor** ξ_1: The lithium in the oven contains the natural composition of ^{6}Li (7.59 %) and ^{7}Li (92.41 %). Only the bosonic isotope ^{7}Li will be trapped in the MOT. Therefore, the value of ξ_1 = 0.9241.

2. **Fraction of slowed atoms** ξ_2: Due to the fact that only atoms with maximum velocity v_0 are decelerated by the Zeeman slower, the fraction of atoms ξ_2 that can be trapped in the MOT is

$$\xi_2 = \frac{\int_0^{v_0} f_{beam}(v)dv}{\int_0^{\infty} f_{beam}(v)dv} = e^{-v_0^2/v_p^2}\left(-\frac{v_0^2}{v_p^2} - 1\right) + 1. \tag{6.11}$$

   For v_0 = 712 m s^{-1}, Equation 6.11 gives a value of ξ_2 = 0.03802.

3. **Beam broadening** ξ_3: Not all atoms with trappable velocities are actually captured in the MOT. Only those that pass within the capture radius can be trapped. This gives another geometrical loss factor

$$\xi_3 = \frac{flux\ of\ slowed\ atoms\ passing\ the\ capture\ region}{total\ flux\ of\ slowed\ atoms}. \tag{6.12}$$

   As will be shown, this will be the dominant loss factor. As mentioned before, the reason for this is that the atoms leave the slower with low axial velocities whereas the radial velocity stays unchanged by slower which leads to a strong beam divergence.

The total flux of trappable atoms is thus given by

$$\Phi_{trap} = \Phi_0 \cdot \xi_1 \cdot \xi_2 \cdot \xi_3. \tag{6.13}$$

Beam Broadening ξ_3**.** The fraction ξ_3 of trappable atoms that pass the capture radius of the MOT is evaluated by calculating the transversal broadening of the atomic beam. The main reason for this broadening beyond the geometrically defined divergence is just the increased time-of-flight of the atoms due to the reduced velocity. Another process that leads to transversal diffusion is spontaneous emission inside the slower.

First, the intensity profile of a velocity class v_i with $0 \leq v_i \leq v_0$ at the plane through the MOT orthogonal to the beam is considered. The total intensity distribution of the atomic beam in the MOT plane is given by the integral over all velocity classes $\leq v_0$. Finally, ξ_3 is calculated as the fraction of this integral to the total intensity distribution of all atoms.

Intensity Profile for Velocity v_i. The intensity profile in the MOT plane transverse to the propagation of the atomic beam with velocity v_i can be described as a Gaussian distribution

$$I_i(x) = \frac{1}{\sqrt{2\pi}\sigma_{MOT,i}} \exp\left[\frac{-x^2}{2\sigma_{MOT,i}^2}\right]$$

with the transversal coordinate x and the width $\sigma_{MOT,i}$ that is composed of

$$\sigma_{MOT,i} = \sqrt{\sigma_{slower,i}^2 + \Delta_{MOT,i}^2} \tag{6.14}$$

$$\sigma_{slower,i} = \sqrt{(\sigma_{geo} + \sigma_{TOF,i})^2 + \sigma_{em,i}^2}. \tag{6.15}$$

Here,

- σ_{geo} is the geometrical width of the unslowed atomic beam at the end of the slower, which is determined by the collimation and apertures of the beam line

$$\sigma_{geo} = \frac{1}{2\sqrt{2}}(2r_s + 2\theta(d_{OS} + L));$$

- $\sigma_{TOF,i}$ is the beam broadening at the end of the slower due to the increased time-of-flight which increases the effective divergence of the atomic beam

$$\sigma_{TOF,i} = \frac{\theta}{2\sqrt{2}}\left(\frac{(v_i - v_f)^2}{a}\right);$$

- $\sigma_{em,i}$ is the additional beam broadening at the end of the slower due to transversal diffusion of the atoms caused by spontaneous emission processes

$$\sigma_{em,i} = \frac{2}{3a}\sqrt{\frac{\hbar k}{M}}(v_i - v_f)^{3/2};$$

- $\sigma_{slower,i}$ is the total width of the beam at the end of the slower

$$\begin{aligned}\sigma_{slower,i} &= \sqrt{(\sigma_{geo} + \sigma_{TOF,i})^2 + \sigma_{em,i}^2} \\ &= \left(\left[\frac{1}{2\sqrt{2}}\left(2r_s + 2\theta\left(d_{OS} + L + \frac{(v_i - v_f)^2}{2a}\right)\right)\right]^2\right. \\ &\quad \left. + \left[\frac{2}{3a}\sqrt{\frac{\hbar k}{M}}(v_i - v_f)^{3/2}\right]^2\right)^{1/2};\end{aligned}$$

- $\Delta_{MOT,i}$ is the additional broadening of the beam between the end of the slower and the MOT plane due to the increased divergence

$$\Delta_{MOT,i} = \left(\theta v_i + \sqrt{\frac{\hbar k (v_i - v_f)}{M}} \right) \cdot \frac{d_{MOT}}{v_f};$$

- and $\sigma_{MOT,i}$ is the total width of the atomic beam profile in the MOT plane

$$\begin{aligned} \sigma_{MOT,i} &= \sqrt{\sigma_{slower,i}^2 + \Delta_{MOT,i}^2} \\ &= \left(\left[\frac{1}{2\sqrt{2}} \left(2r_s + 2\theta \left(d_{OS} + L + \frac{(v_i - v_f)^2}{2a} \right) \right) \right]^2 \right. \\ &\quad + \left[\frac{2}{3a} \sqrt{\frac{\hbar k}{M}} (v_i - v_f)^{3/2} \right]^2 \\ &\quad \left. + \left[\left(\theta v_i + \sqrt{\frac{\hbar k (v_i - v_f)}{M}} \right) \cdot \frac{d_{MOT}}{v_f} \right]^2 \right)^{1/2}. \end{aligned}$$

Assuming that the terms in 6.14 are independent from each other, they can be summed up quadratically.

In order to visualise the contributions of the different broadening parameters, graphs of σ_{slower} and σ_{MOT} for different final velocities v_f are plotted in Figure 6.6 as a function of the velocity class v_i. Obviously, the broadening inside the Zeeman slower is very small compared to the broadening of the atomic beam after it is slowed down to v_f. The total broadening can thus significantly be reduced by choosing a larger final velocity since then the atoms need less time to travel from the end of the slower to the trapping region. This behaviour is also illustrated in Figure 6.6.

Total Intensity Distribution. The total intensity distribution of the atomic beam at the MOT plane is given by the integral over the distributions I_i of all slowed velocity classes $0 \leq v_i \leq v_0$ that are weighed with the distribution 6.10:

$$\begin{aligned} I(x) &= \int_0^{v_0} f_{beam}(v_i) I_i(x) dv_i \\ &= \int_0^{v_0} \frac{2v_i^3}{\sigma_{MOT,i}\sqrt{2\pi}} \left(\frac{M}{2k_B T} \right) \exp\left[\frac{-M v_i^2}{2k_B T} \right] \exp\left[\frac{-x^2}{2\sigma_{MOT,i}^2} \right] dv_i \end{aligned}$$

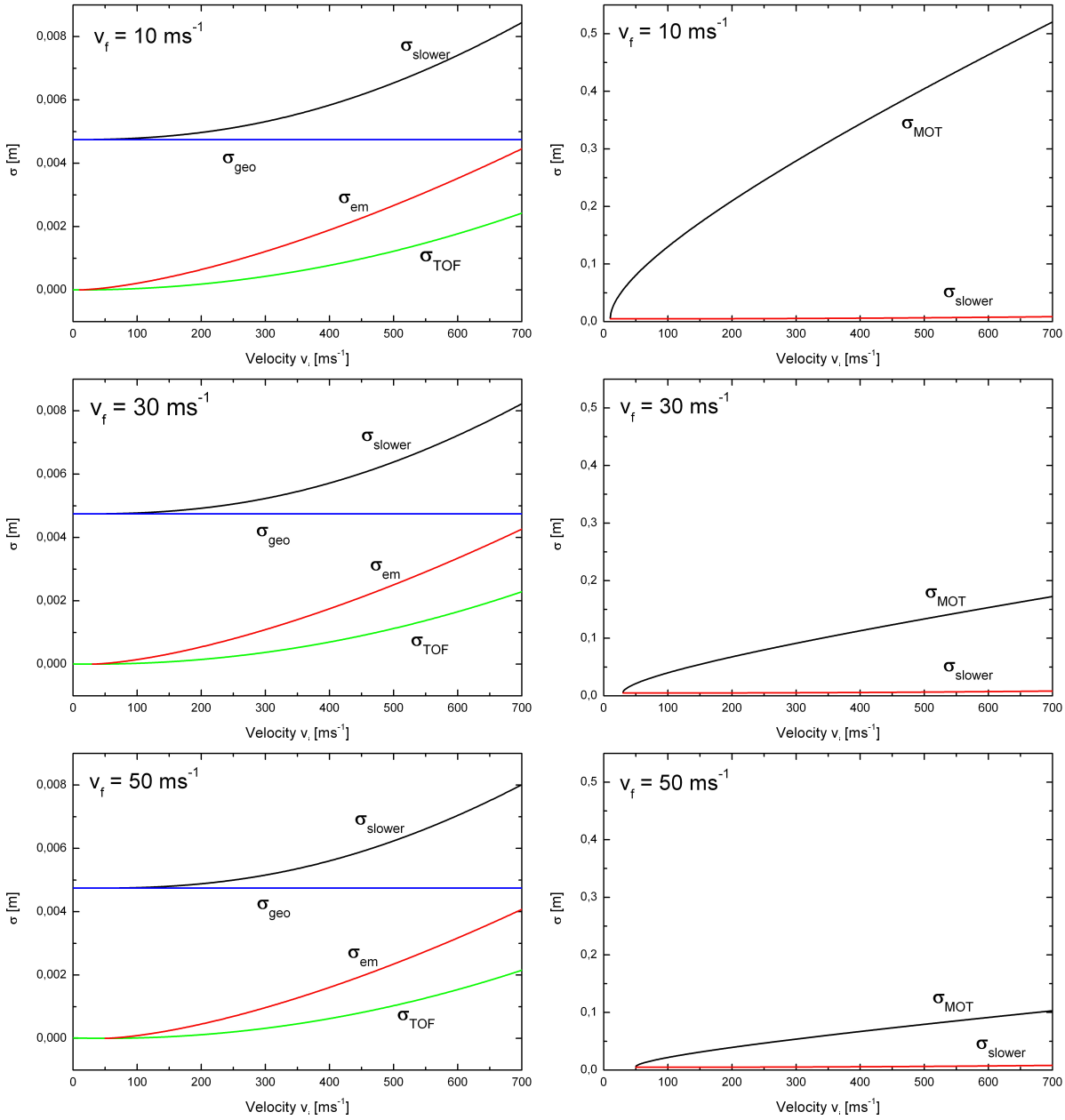

Figure 6.6: Beam broadening at the end of the slower (left) and at the MOT (right) as a function of the velocity group v_i for three different final velocities v_f. The broadening Δ_{MOT} contributes most to the total width $\sigma_{MOT,i}$ at the trapping region and depends strongly on v_f. Since σ_{slower} is very small, the curves of Δ_{MOT} and $\sigma_{MOT,i}$ almost overlap and, therefore, Δ_{MOT} is not plotted in the diagrams.

Flux Through MOT Capture Region. Due to the radial symmetry of the problem, $I(x)$ can be expressed as a radial symmetric function $I(r)$ with the radial coordinate $r > 0$. The fraction ξ_3 of the flux through the capture region of the MOT with a radius r_{cap} is

then given by

$$\xi_3 = \frac{\int_0^{r_{cap}} I(r)dr}{\int_0^{\infty} I(r)dr}.$$

Numerical integration using MATHEMATICA gives a value of 0.02789 for ξ_3. It is therefore the dominant loss factor. With all loss factors given, the resulting flux of trappable atoms calculated from Equation 6.13 is Φ_{trap} = 1.328·10^8 atoms/s.

6.4.3 Results and Discussion

In this subsection some results predicted by the theoretical model of the atomic beam are presented and discussed. In Table 6.1 the values which are used for the calculations and the calculated numbers are summarised.

Most important is the flux of trappable atoms Φ_{trap} through the capture region of the MOT in the order of 10^8 atoms/s. Considering that typical numbers in a MOT are between of a few 10^8 and 10^9 atoms, the calculated flux would be sufficient to achieve reasonable loading rates of a few seconds. Therefore, the conclusion from the theoretical model is that the designed atomic beam machine will meet the requirements for efficient loading of the trap.

Table 6.1: Parameters used for the calculations of the atomic beam broadening. Temperature dependant values are given for T = 700 K

Name	**Symbol**	**Value**	**Unit**
Distance slower-MOT	d_{MOT}	333	mm
Distance oven-slower	d_{OS}	157.4	mm
Length of slower	L	388	mm
Total distance oven-MOT	L_{tot}	878.4	mm
Oven temperature	T	700	K
Maximum slowed velocity	v_0	712	m s^{-1}
Velocity after slower	v_f	10	m s^{-1}
Radius of nozzle aperture	r_s	0.5	mm
Area of nozzle aperture	A_s	0.7854	mm^2
Collisional cross section	σ_c	7.6	10^{-16} cm^2
Capture radius	r_{cap}	1	mm
Vapour pressure	p_V	0.3536	10^{-3} mbar
Number density	n_0	3.658	10^{18} m^{-3}
Mean free path	λ_A	2.453	m
Average thermal velocity	$\bar{v}$	1455	m s^{-1}
Most probable thermal velocity	v_p	1290	m s^{-1}
Total atom flux from oven	Φ	1.331	10^{21} $m^{-2}s^{-1}$
Flux into opening angle θ	Φ_0	1.356	10^{11} s^{-1}
Trappable flux at MOT	Φ_{trap}	1.328	10^8 s^{-1}
Flux of atoms through nozzle	$\dot{N}$	1.045	10^{15} s^{-1}
Relative abundance of ^{7}Li	ξ_1	92.41	%
Fraction of slowed atoms	ξ_2	3.802	%
Slowed atoms in MOT region	ξ_3	2.789	%
Effective deceleration	a	790046	m s^{-2}
Initial beam divergence	θ	11.39	mrad
Geometrical beam width	σ_{geo}	4.204	mm
Beam width at end of slower	$\sigma_{slower,i}$		
Broad. from spont. emission	$\sigma_{em,i}$		
Broad. from time-of-flight	$\sigma_{TOF,i}$		
Beam width at MOT	$\sigma_{MOT,i}$		

Chapter 7

The Magneto-Optical Trap

With the development of laser cooling in the last decades, powerful tools for atomic physics became available. The idea to trap particles and even atoms or molecules by radiation pressure was published as early as 1970 by [Ash70]. Doppler cooling was first suggested by T. W. Hänsch and A. L. Schawlow [Hän75] in 1975 for neutral atoms and independently by D. Wineland and H. Dehmelt [Win75] for trapped ions. From these first proposals the concepts of optical molasses and the Zeeman shift spontaneous force optical trap (ZOT) or magneto-optical trap (MOT) [Raa87] was developed by several groups leading to the Nobel Price for Stephen Chu [Chu98], William D. Phillips [Phi98] and Claude N. Cohen-Tannoudji [CT98] in 1997 *for development of methods to cool and trap atoms with laser light*. The theoretical principles of the MOT were derived in Chapter 2. The experimental results which were obtained with the described set-up are presented in the following section.

7.1 Characterising the MOT

In this section the first measurements performed on the MOT are presented and discussed. Since the MOT was designed as a target for ionisation experiments, the results will be considered with emphasis on the suitability of the trap as a target. All results presented in this work were obtained with a MOT that was realised using the dye-laser system described in Chapter 4.

7.1.1 Loading the Trap

As mentioned in Chapter 5 a magneto-optical trap can be loaded either from a (slow) atomic beam coming from a Zeeman slower or from a thermal background gas [Mon90], the latter being less efficient and giving smaller lifetimes due to collisions with the background. For first experiments, a lithium dispenser was used for the purpose of loading

the trap. The threshold current for evaporation of lithium vapour from the dispenser is around I_{dis} = 5.5 A giving a temperature of about 500 ℃. In Figure 7.1 pictures of the MOT and a first trapped atom cloud are shown. These pictures, as well as all further measurements, were taken with a current of 55 A through the MOT coils which was the maximum current available from the power supply. The detuning of the trapping laser was set to 20 MHz which corresponds to roughly 4 linewidths.

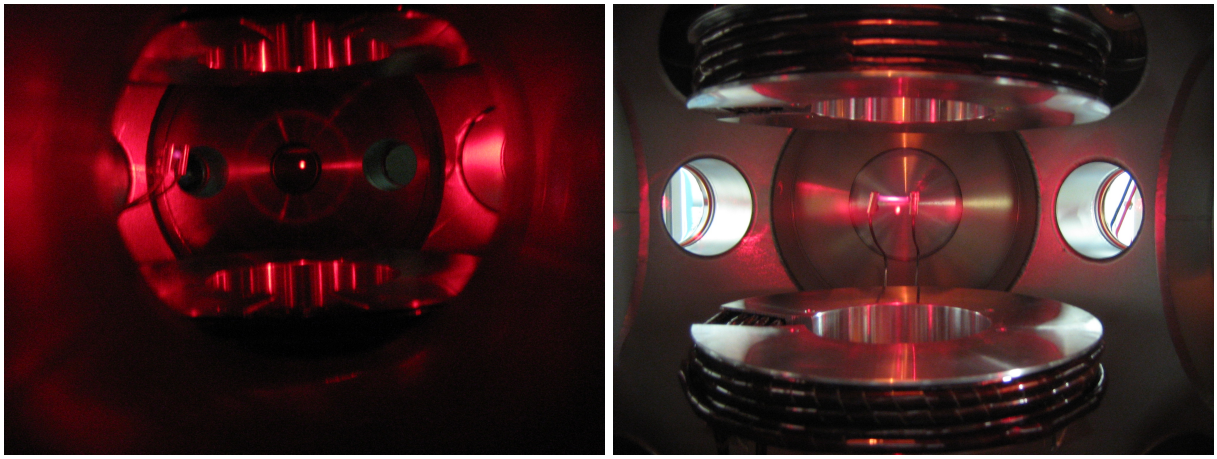

Figure 7.1: Pictures of the MOT taken with a digital camera. Also the Li dispenser, the MOT coils and the windows for the trapping laser can be seen. Around the MOT, fluorescence from the lithium vapour is visible.

With increasing current through the dispenser, the temperature and, thus, the rate of evaporation is increased. This leads to faster loading of the trap and higher final atom numbers until a equilibrium sets in at about 7 A, where the higher loading rate is met by higher losses caused by collisions with hot Li atoms from the dispenser. The loading curves of the MOT for different dispenser currents shown in Figure 7.2 were measured with a photo diode. For better comparison of the final atom number in the trap, the background fluorescence which can be seen in the left part of Figure 7.2 was subtracted in the right hand plot. Although the total number of atoms (which is proportional to the total fluorescence) saturates at about 7 A, the loading time still decreases for higher current, reaching about 3 s only at 8 A. Here, a small decrease of the total fluorescence can be seen, which is, however, within the statistical variations (noise) and, thus, provides no real evidence.

For the purpose of comparison of the loading times and final atom numbers for different dispenser currents I_d, the measured values from Figure 7.2 are plotted versus I_d as displayed in Figure 7.3.

Due to the fact that the lifetime of the dispenser depends on the applied current, further measurements were done with a current of 6.5 A. Here, the loading rate is already short enough and a reasonable number of atoms is trapped.

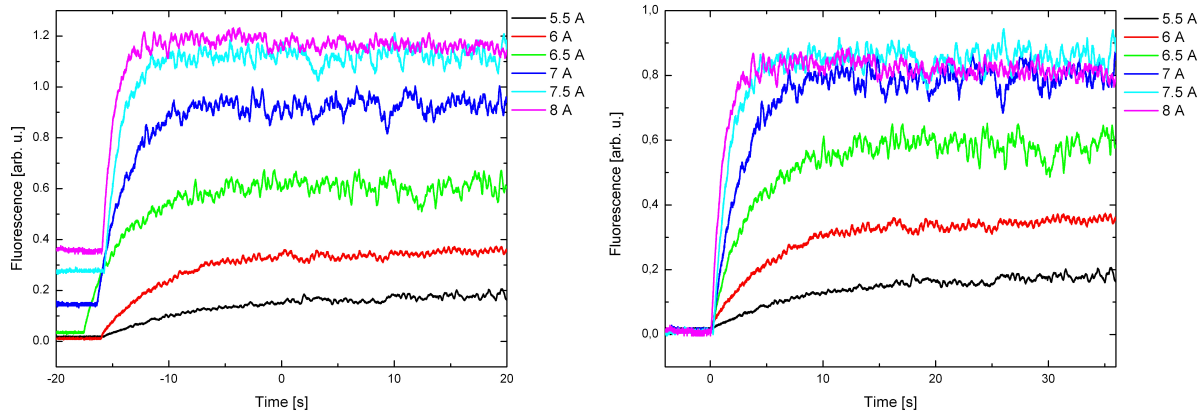

Figure 7.2: Number of atoms (total fluorescence) in the MOT as a function of loading time for different dispenser currents. In the right hand plot the offset from the background fluorescence (left part of the figure) is subtracted for better comparison and the starting points of the loading procedure are set to $t = 0$ s. These measurements were taken with a detuning of 20 MHz and an optical power of 30 mW per beam.

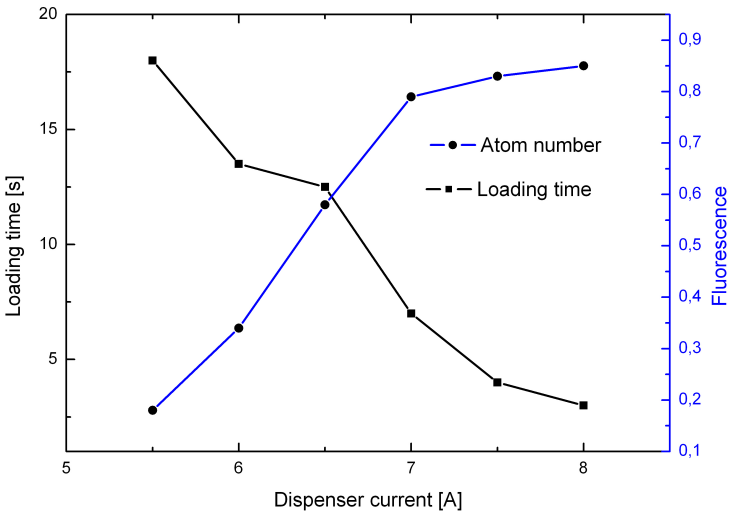

Figure 7.3: Loading time and fluorescence plotted against the dispenser current.

The dependence of the number of trapped atoms and the loading rate on the laser power was measured with fixed dispenser current. The power of each laser beam was varied with a half-wave plate and a PBC. The resulting loading curves are plotted in Figure 7.4. For a laser power smaller than 20 mW per beam, the maximum number of trapped atoms is significantly decreased. With the present beam diameter of 2 cm the saturation intensity of I_s = 2.56 mW/cm^2 is reached at a power of 8 mW. However, for effective laser cooling and trapping the saturation parameter $s_0 = I/I_s$ should be greater than 2. This could explain that for 20 mW (I = 6.37 mW/cm^2, s_0 = 2.49) the number of trapped atoms is significantly larger than for 15 mW (I = 4.77 mW/cm^2, s_0 = 1.86).

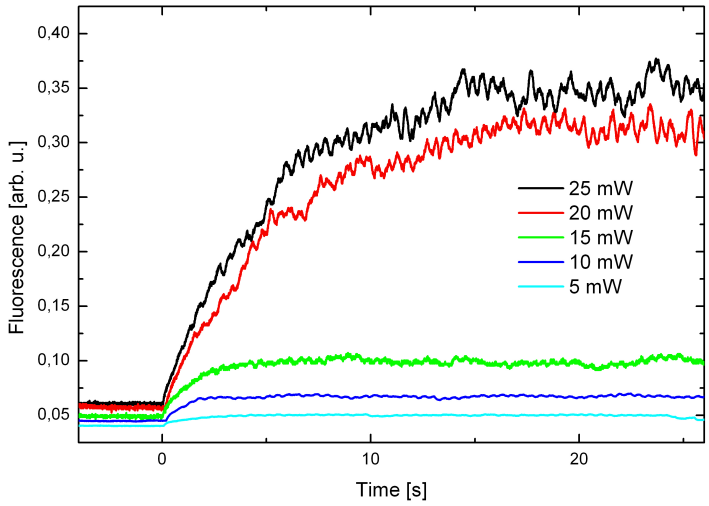

Figure 7.4: Number of trapped atoms (fluorescence) versus loading time for different laser powers at a dispenser current of 6.5 A.

In the final set-up the MOT will be loaded from a Zeeman slowed atomic beam which has a lot of advantages compared to the use of a dispenser. As calculated in Section 6.4.2 the flux of trappable atoms from the Zeeman slower within the trapping region is estimated to be Φ_{trap} = 1.328·10^8 atoms/s, which should lead to a substantially higher loading rate and, thus, to a larger total atom number in the trap. Apart from delivering a considerably increased flux of slow atoms, the atomic beam from the slower can also be switched on and off very fast by a pneumatic shutter. This is important for the lifetime of the atoms in the trap and it also prevents unwanted contamination of the vacuum chamber during the experimental cycle. Since the multi-channel plate detectors which will be installed in the set-up are very sensitive, contamination with Li vapour is highly undesirable. Furthermore, the ceramic isolators of the extraction electrodes could become conducting from condensing Li atoms. Through its high reactivity, Li can also destroy the optical viewports or make them opaque. A fortiori, as little unused lithium vapour as possible should be introduced to the main vacuum chamber making it necessary to be able to rapidly switch off the Li supply if not needed. Since the evaporation rate of the dispenser depends on its temperature, it cannot be controlled very fast. Figure 7.5 shows measurements of the MOT's fluorescence with the dispenser being switched on and off, respectively.

7.1.2 Absolute Atom Number

In order to determine the absolute number of trapped atoms, a simple estimation was made. By shining the light from the master diode laser onto the photo diode with known intensity, the signal from the diode could be calibrated. At 400 nW the photo diode

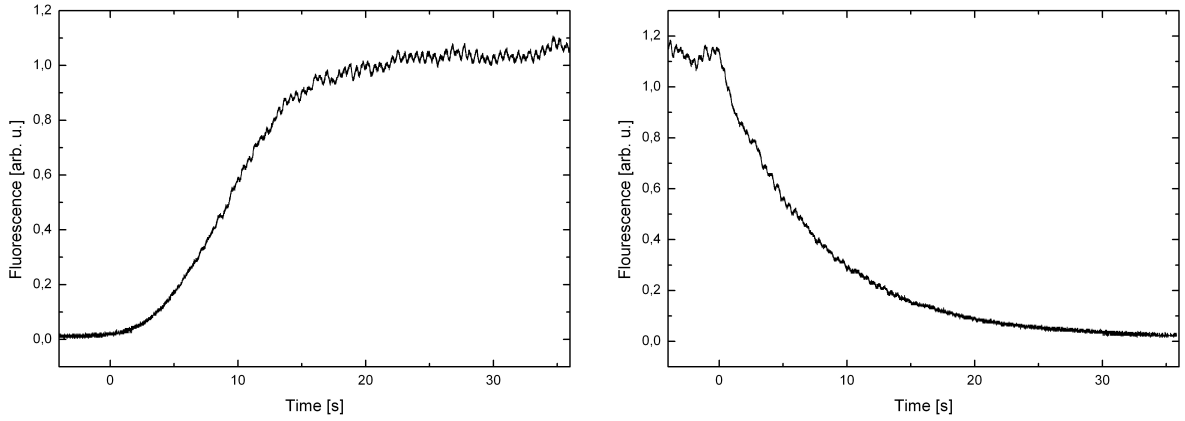

Figure 7.5: Left: fluorescence signal from the MOT with the dispenser switched on to 8 A at t = 0 s. Right: MOT fluorescence after switching off the dispenser at t = 0 s.

measured a voltage of 1 V. A photon with the wavelength $\lambda = 671$ nm carries an energy of $E_\nu = h \cdot c/\lambda \approx 2.96{\cdot}10^{-19}$ J. Thus, 400 nW of optical power corresponds to one 671 nm photon every $7.4{\cdot}10^{-13}$ s. Since the lifetime of the excited state of the lithium atom is τ = 27 ns, this should also give the rate of isotropically scattered photons at saturation intensity. The optical power emitted from a cloud of N_a atoms into a solid angle Ω can then be estimated by

$$P = N_a \cdot \frac{E_\nu}{\tau} \cdot \frac{\Omega}{4\pi} \approx N_a \cdot 1.1 \cdot 10^{-11}\ W \cdot \frac{\Omega}{4\pi}$$

The area of the photo diode and its distance to the atomic cloud gives the observation solid angle $\Omega = A_{PD}/d \approx 7.86{\cdot}10^{-3}$ sterad. Therefore, if the signal of the photo diode is 1 V the number of atoms in the cloud is approximately $N_a \approx 4.7{\cdot}10^6$ atoms. This value is close enough to the expected number, although atom numbers of up to 10^8 should be possible. This estimation is quite crude since it does not take into account the strengths of the different hyperfine transitions which are driven by the laser.

7.1.3 Size of the MOT

In order to determine the size of the MOT, pictures of the atomic cloud were taken with a CCD camera. The CCD bitmap was calibrated by taking simultaneously a picture of a ruler with the same settings of the camera's lens. Figure 7.6 shows the CCD pictures of the MOT and the ruler.

As concluded from the CCD pictures, the calibration was determined to be 8 pixels/mm. The size of the MOT in the CCD image shown in Figure 7.6 is $22{\times}16$ pixels^2 which corresponds to $2.75{\times}2$ mm^2. Assuming that the three-dimensional shape of the cloud is that of an ellipsoid with a long axis x = 2.75 mm and a short axis y = 2 mm the

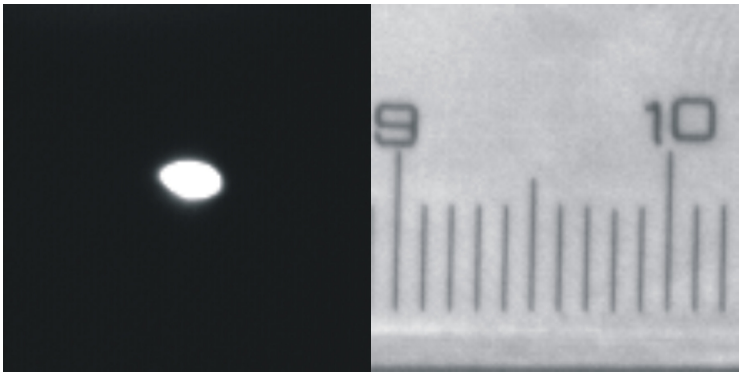

Figure 7.6: CCD pictures of the MOT and of a ruler taken to determine the size of the atomic cloud. Both pictures are zoomed to an area of 110×110 pixels^2.

volume is given by

$$V_{MOT} = \frac{\pi}{6} x \cdot y^2 = 5.76 \text{ mm}^3.$$

With the absolute atom number obtained in Section 7.1.2, the density of the MOT amounts to $\rho_{MOT} = N_a/V_{MOT}$ = 8.16·10^8 atoms/cm^3. The area density of the MOT which is an important property of a target in scattering experiments is given by $\sigma_{MOT} = N_a/A_{MOT}$ = 3.42·10^8 atoms/cm^2.

7.1.4 Release-Recapture

As already mentioned in Chapter 3, the fields of the MOT have to be switched off and on very rapidly during data acquisition. To be able to perform as many experimental cycles as possible without having to reload the trap, as few atoms as possible should get lost during this process. In the presented release-recapture measurements only the laser beams of the MOT were turned off and on by the AOMs. The switches for the field coils were not available yet and, therefore, the magnetic field was unchanged during the measurements. The Li dispenser was running continuously during the measurements at a current of 6 A. The vacuum pressure in the main chamber was at p = 1.3·10^{-9} mbar.

In a first series of measurements, the lasers were switched with different off-times and the fluorescence of the MOT was measured with a photo diode. The measurements are shown in Figure 7.7. Here, the trapping lasers were first switched off for 4 s (time interval a) and then, after the MOT was loaded again, the lasers were switched off for 1, 5, 15, 20 and 25 ms, respectively.

For a single release-recapture cycle, no change in the fluorescence is found for an off-time of 1 ms. For off-times of 5 ms and more, a decrease of the fluorescence signal can be observed. The fraction of recaptured atoms can be determined from the change

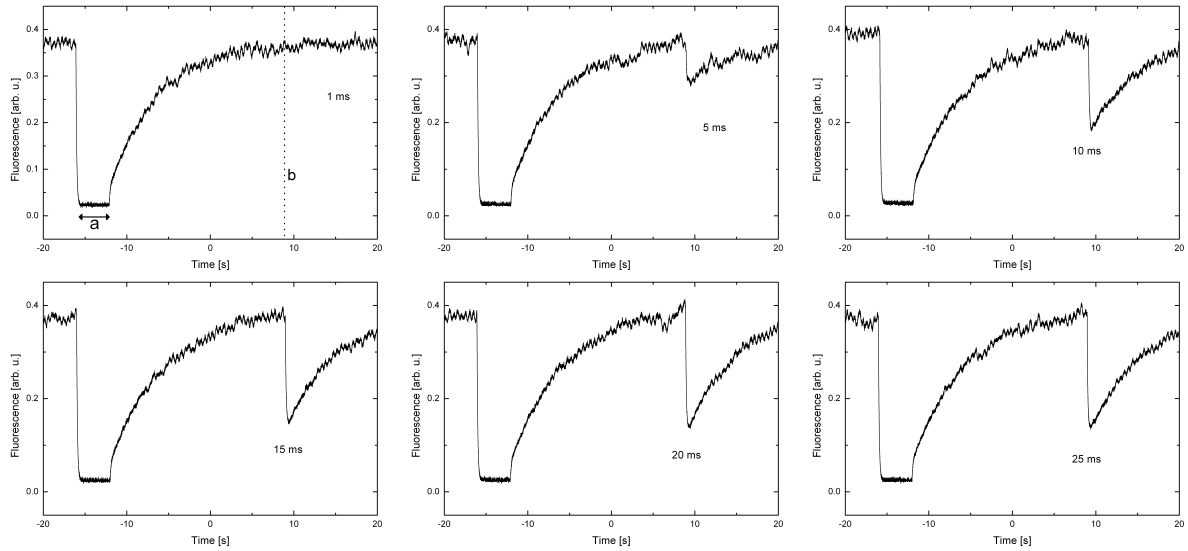

Figure 7.7: Single-cycle release-recapture measurements with laser off-times t_{off} of 1, 5, 10, 15, 20 and 25 ms, respectively. First the lasers are off for 4 s at -25 s. Then, the MOT is reloaded until the lasers are switched off for t_{off} at +10 s indicated by the broken line b.

of the fluorescence signal and compared to the theoretical prediction which is given by [Fri99]

$$N_r(t_{off}) = \mathrm{erf}\left(\frac{\frac{r_c}{t_{off}}}{\sqrt{\frac{2k_BT}{M}}}\right) - \frac{2}{\sqrt{\pi}}\frac{\frac{r_c}{t_{off}}}{\sqrt{\frac{2k_BT}{M}}}\exp\left[-\frac{\frac{r_c}{t_{off}}}{\sqrt{\frac{2k_BT}{M}}}\right]^2, \tag{7.1}$$

where "erf" is the error function, r_{cap} is the capture radius of the MOT, k_B is the Boltzmann constant, T is the temperature of the cloud and M is the atomic mass. In this equation it is assumed that all atoms are at the central point of the trap and expand with thermal velocities according to the temperature T. After an off-time t_{off}, only those atoms are captured, which are inside the capture radius r_{cap}, basically given by the diameter of the trapping lasers (2 cm). Using the measurements shown in Figure 7.7 one can get an estimation of the temperature of the trapped atoms by plotting the fraction of recaptured atoms versus the off-time and fitting with Equation 7.1. The result which is displayed in Figure 7.8 yields a temperature of (500±136) µK if a capture radius of 9 mm is used as a fitting parameter. However, large discrepancies between the measured points and the fitted curve are found and, thus, the used equation does not seem to describe the observed release-recapture process very well.

In the real experiment the trapping fields will be switched off and on a few hundred times before the trap will be reloaded again, as discussed in Section 1.3. Using Equation 7.1, the fraction of atoms left in the trap after several release-recapture cycles can be calculated and plotted as a function of the off-time [Spi05]. The resulting curves for 1,

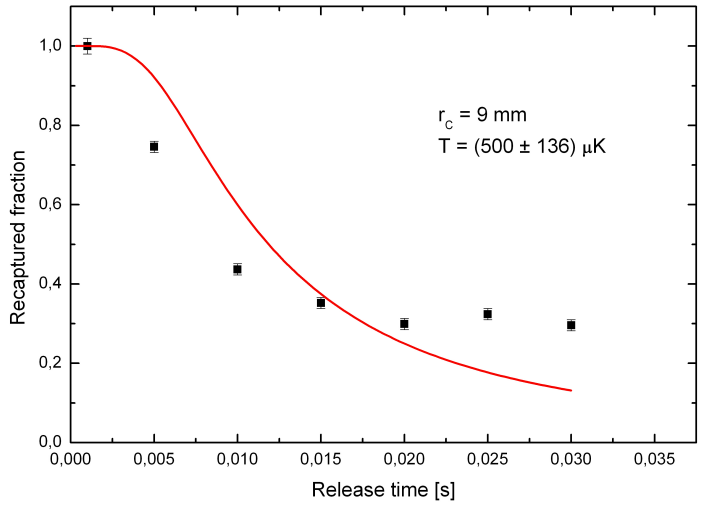

Figure 7.8: Recaptured fraction of atoms taken from Figure 7.7 and plotted against the off-time. Red line: Equation 7.1 fitted to the data with r_c = 9 mm and T = (500±136) µK.

10, 100, 500 and 1000 cycles, respectively, are plotted in Figure 7.9 for a temperature of 142 µK. The finite lifetime of the MOT (mainly caused by collisions with background gas from the dispenser or with fast atoms from the atomic beam once the Zeeman slower will be used) is considered by adding another factor $\exp[-t_{off}/\tau]$ with τ being the lifetime (empirically around $\approx$ 3 s). It can be seen that even after 500 cycles of release and recapture only a small fraction of atoms is lost if the release time is not greater than $\approx$ 1 ms. The fraction of recaptured atoms strongly depends on the capture radius.

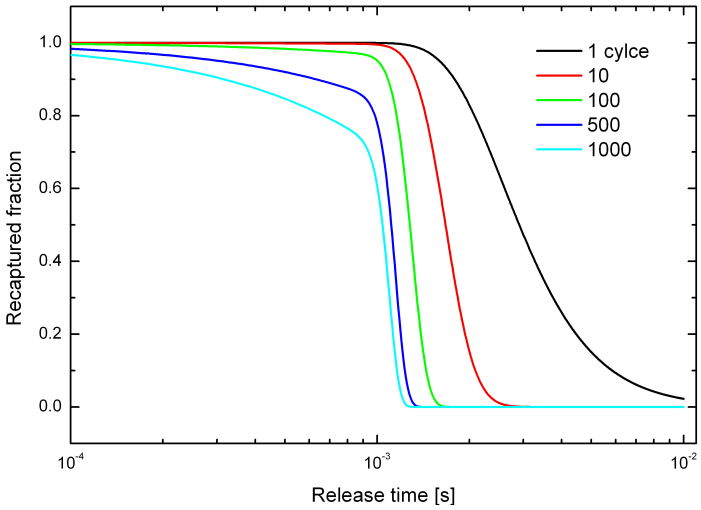

Figure 7.9: Recaptured fraction of atoms versus release time for 1, 10, 100, 500 and 1000 cycles for a capture radius of 10 mm and a temperature of 142 µK.

For the purpose of investigating the behaviour of the real atomic cloud and to determine the fraction of atoms that are left in the trap after many release-recapture cycles, a function generator is used to switch the trapping lasers with variable parameters which are listed in Table 7.1. Each switching sequence lasts for 2 s and is started after the MOT is loaded.

Table 7.1: Parameters used in the release-recapture measurements. All experiments were performed at a pressure of $1.5 \cdot 10^{-9}$ mbar, a dispenser current of 6 A and a field current of 55 A

Index	Cycles	On-time [ms]	Off-time [ms]	Frequency [Hz]
a		∞	0	
b	1000	1	1	500
c	1000	0.9	1.1	500
d	1000	0.8	1.2	500
e	1000	0.7	1.3	500
f	1000	0.6	1.4	500
g	1000	0.5	1.5	500
h	1000	0.4	1.6	500
k	1200	1	0.67	600
m	1400	1	0.43	700
n	1600	1	0.25	800
o	1800	1	0.11	900

The behaviour of the MOT during fast switching of the trapping lasers is illustrated by CCD images of the atomic cloud taken during each sequence. After the MOT is loaded (as shown in Figure 7.10.a for continuous operation), the fields are switched as described above leading to a blurring and expansion of the atomic cloud. Figure 7.10 shows time averaged images of the cloud taken during the switching mode of the trapping lasers. When the switching sequence is finished and the lasers are on again, the cloud instantly reappears. In order to get time resolved information and to determine which fraction of atoms is left in the trap after a whole sequence, the fluorescence was also measured with a photo diode, plotted in Figure 7.11. The fraction of atoms that are left inside the trap after each measurement is given by comparing the fluorescence signal before and after the switching sequence which lasts for 2 s in all of the measurements shown in Figure 7.11. Due to the fact that the lasers are switched very fast, the plotted signal going to zero for laser off and up again for laser on, covers a black area. A zoom into that black area shows the periodical variation of the fluorescence with the switching time (Figure 7.11.p). As seen in the different plots, most atoms are recaptured into the trap if the off-time is not too long. Only for t_{off} = 1.6 ms significant losses can be found. Therefore, an off-time t_{off} = 1.5 ms is possible without loosing too many atoms. Plots k - o show that the on-time of the trapping lasers can be reduced to t_{on} = 0.25 ms while even increasing the number of cycles, without increasing the loss factor significantly. However, the size of the cloud becomes larger (Figure 7.10.g, h) and, therefore, the density is reduced.

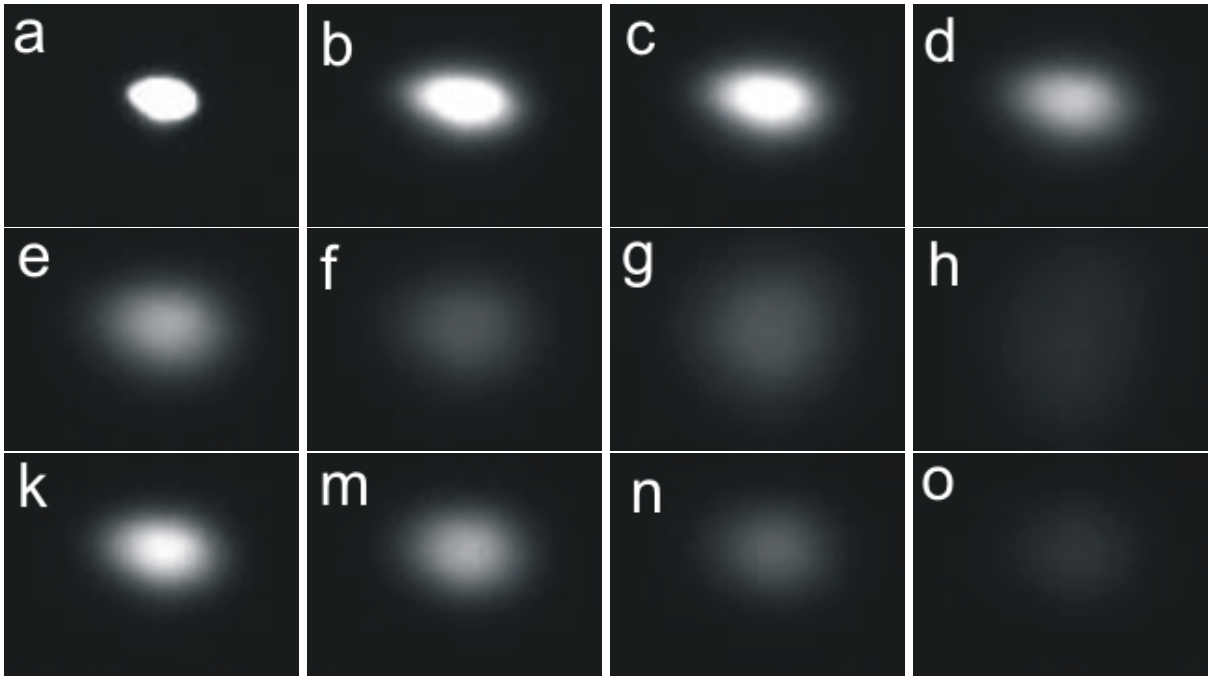

Figure 7.10: CCD images of the MOT for continuous operation (a), and different combinations of (on, off)-times. The parameters used in the measurements are listed in Table 7.1.

Concluding from the measurements, a combination of t_{on} = 0.25 ms and t_{off} = 1.5 ms with about 1000 cycles seems to be a reasonable choice for the future ionisation experiments provided that the corresponding target density is still sufficient. If one accounts about 200 µs for the switching of the magnetic field, a total time interval of 1.1 ms would be left for data acquisition. At an expected reloading time for the MOT of 2 s, a total cycle would last 3.75 s including a total of 1.1 s for data acquisition corresponding to a duty cycle of 30 % which is much better than the originally expected 10 % (see Section 1.3 or [Spi05]). In this estimation the magnetic fields are switched during the off-time of the trapping lasers. This way the effects of decreasing and increasing magnetic fields on the trap during switching can be neglected.

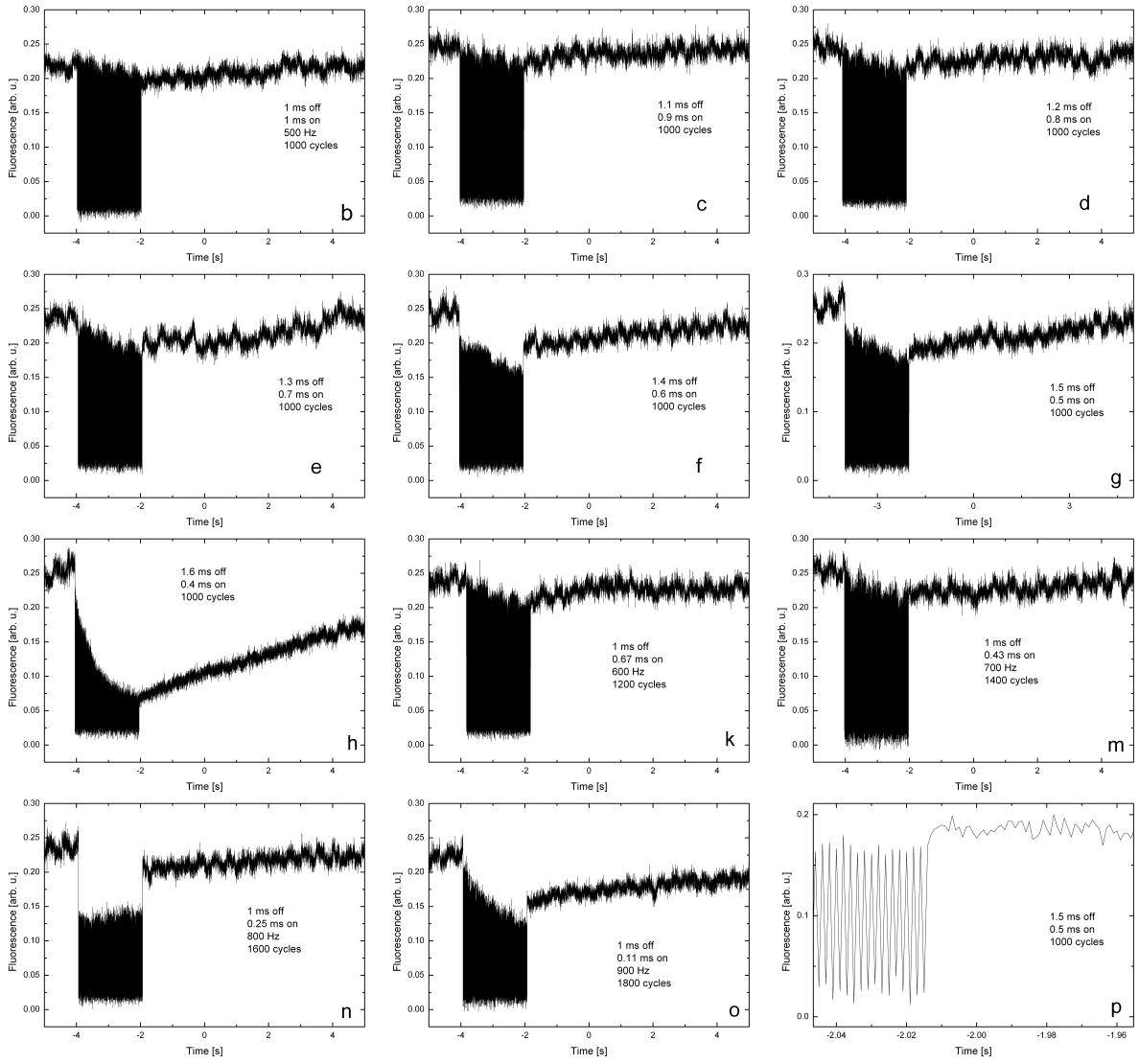

Figure 7.11: Fluorescence signals from the MOT measured with a photo diode during the release-recapture sequences with the parameters given in Table 7.1 and indicated in the figure. The last graph shows a zoom where the distinctive "on" and "off" peaks can be seen.

Summary

In this work a Li magneto-optical trap as a target for a reaction microscope was set up and characterised. This included the design and operation of a diode laser system and a dye-laser as well as the assembly of a vacuum chamber which will also contain the spectrometer including all detectors. For efficient loading of the magneto-optical trap from a cold atomic beam, a Zeeman slower was designed, simulated and assembled and calculations characterising the atomic beam were performed. Since it was not possible to use the Zeeman slower, because the necessary power supplies were not available yet, the magneto-optical trap was loaded from a lithium dispenser.

From the measurements with the diode laser system compared to the later used dye-laser system it could be concluded that, on the basis of present technology, the latter has important advantages which are essential for the future experiment. The long term stability of the dye-laser allows the stable operation of the set-up for many hours. This stability is required to gain sufficient statistics since the cross section for triple ionisation of lithium is very small compared to single and double ionisation (Table 1.4). Although the results for injection locking from [Pra98] could be reproduced with the presented diode laser system, the mechanical stability and total output power was found to be crucial, yet not satisfactory and will be improved in the future. Provided that the development of tapered amplifier chips for the Li wavelength progresses as anticipated, a high power diode laser system with high stability and good beam shape can be set up with the existing master lasers.

The measurements on the magneto-optical trap demonstrated that it will be possible to use magneto-optically trapped atoms as a target for a reaction microscope. The achieved number of trapped atoms of a few 10^6 and corresponding target density of a few 10^8 atoms/cm^2 after a loading time of a few seconds are expected to be high enough for a large variety of ionisation and capture measurements using single photons, high-intensity laser pulses, electrons or highly charged ions. By loading the trap from the Zeeman slower, faster loading rates and, therefore, higher atom numbers and target densities are possible. For experiments using intense short laser pulses it may be an advantage to directly use the slow and cold atomic beam as a target, thus being able to avoid the switching of the MOT fields. The feasibility of a fast switching trap in the kHz range could be demonstrated by switching the trapping lasers off and on with different time intervals. In the real experiment, the lasers could even be left on while the magnetic

field of the magneto-optical trap is switched. In this case, it is expected that the fraction of recaptured atoms will increase since Doppler cooling from the lasers would decrease the loss rate.

Appendix A

Physical Constants

Table A.1: Physical constants. The 1-σ uncertainties in the last digits are given in parentheses after the values [Gro00]

Quantity	**Symbol**	**Value**	**Unit**
Avogadro constant	N_A	6.022 136 7(36)	10^{23} mol^{-1}
Boltzmann constant	k_B	8.617 385(73)	10^{-5} eV K^{-1}
Speed of light in vacuum	c	299 762 458	m s^{-1}
Planck constant	h	6.626 068 76(52)	10^{-34} J s
Planck constant, reduced	$\hbar$	6.582 122 0(20)	10^{-16} eV s
Electron charge	e	1.602 177 33(49)	10^{-19} C
Electron mass	m_e	0.510 999 06(15)	MeV c^{-2}
Atomic mass unit	u	931.494 32(28)	MeV c^{-2}
Fine structure constant	α	1/137.035 989 5(61)	
Rydberg energy	hcR_∞	13.605 698 1(40)	eV
Bohr magneton	μ_B	5.788 382 63(52)	10^{-11} MeV T^{-1}
Permittivity of free space	ϵ_0	8.854 187 817	10^{-12} F m^{-1}
Permeability of free space	μ_0	4π	10^{-7} N A^{-2}

Appendix B

Atomic Units

In atomic physics it is common to use atomic units. The units for length, mass, charge and velocity of this system are based on the values for an electron in the hydrogen ground state. The base quantities and fundamental constants thus are are lilsted in Table B.1. Conversion factors are given in Table B.2.

Table B.1: Physical constants corresponding to one atomic unit (1 a.u.)

Name	**Symbol**	**Value**	**Unit**
Bohr radius	r_e	0.529 177 208 3(19)	10^{-10} m
Velocity of first Bohr orbit	v_e	2.187 691	10^{6} m s^{-1}
Electron charge	e	1.602 177 33(49)	10^{-19} C
Electron rest mass	m_e	0.510 999 06(15)	MeV c^{-2}
Angular momentum quantum	$\hbar = m_e v_e r_e$	6.582 122 0(20)	10^{-16} eV s
Speed of light	c	299 762 458	m s^{-1}

Table B.2: Conversion factors for common units

Name	**Conversion factor**
Energy	E [eV] = 27.2 E [a.u.]
Momentum	p [kg m s^{-1}] = 1.995 $\cdot 10^{-24} \cdot p$ [a.u.]
Velocity	v [m s^{-1}] = 2.1877 $\cdot 10^{6} \cdot v$ [a.u.]

Appendix C

Workshop Drawings

In this chapter the workshop drawings of the parts designed by the author are printed. These include the drawings for the Zeeman slower with the cooling discs, the oven for the atomic beam and the optics mounts that can be fixed to CF63 windows and are very useful to mount the MOT optics to the vacuum chamber. All parts were manufactured at the MPI-K mechanical workshop. For the support, helpful comments and manufacture the author owes many thanks to all members of the mechanical workshop.

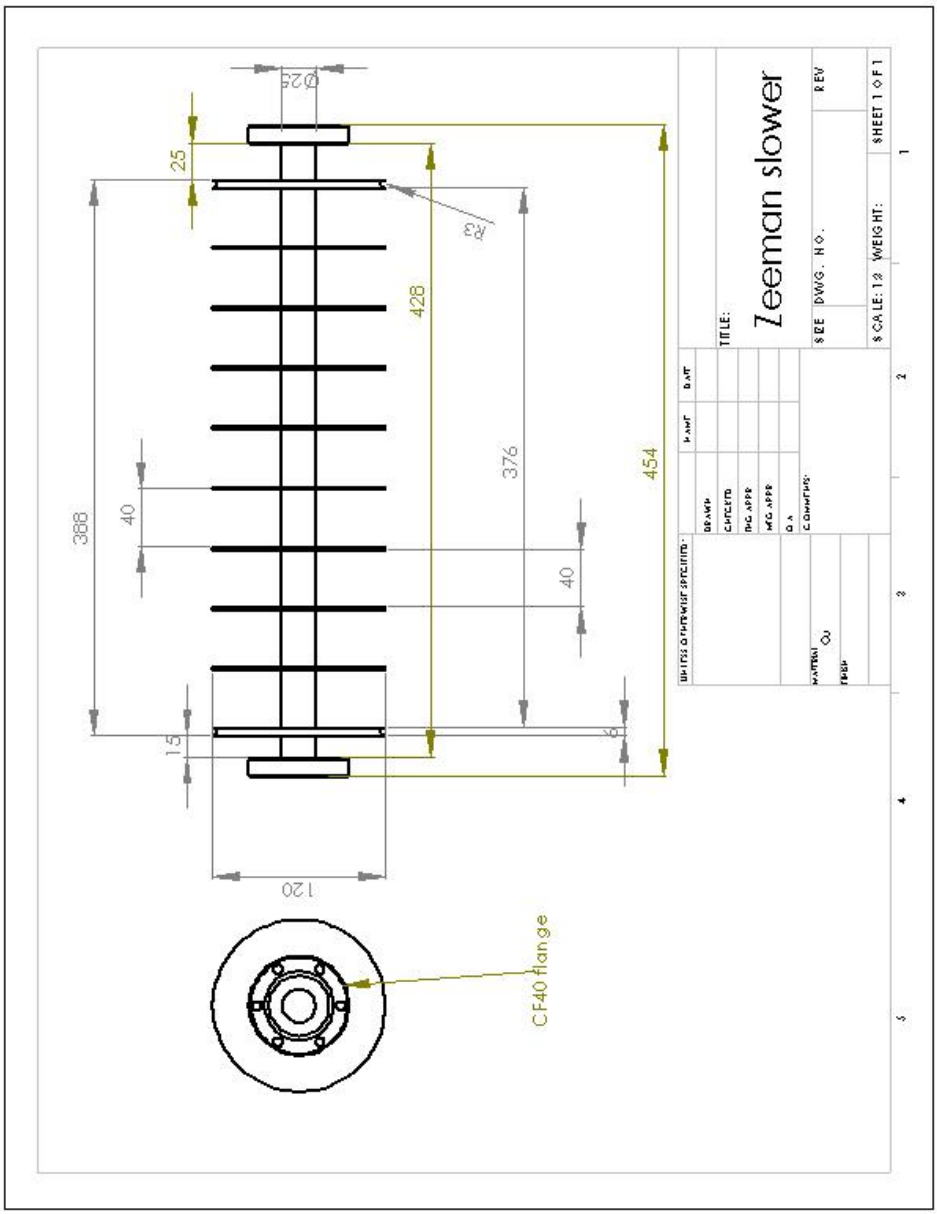

Figure C.1: Drawing of the assembled Zeeman slower.

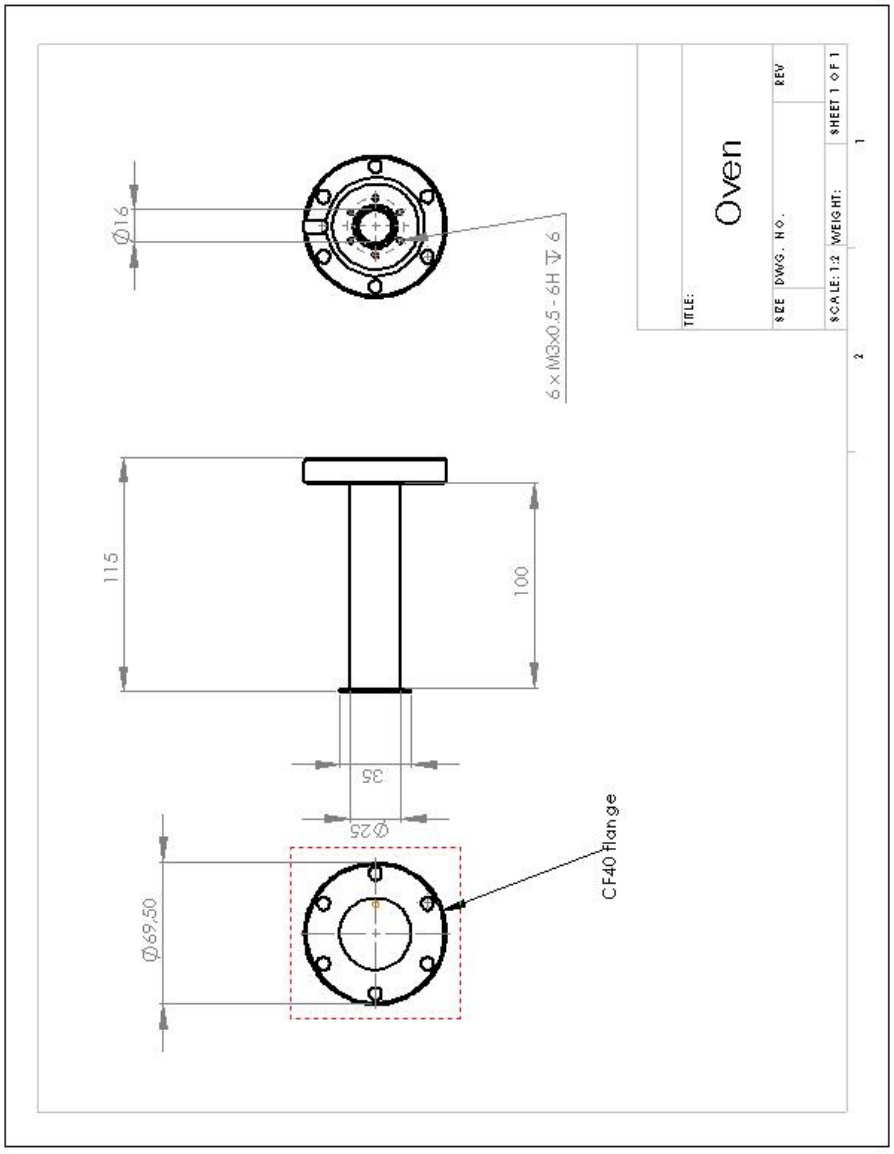

Figure C.2: Drawing of the atomic oven.

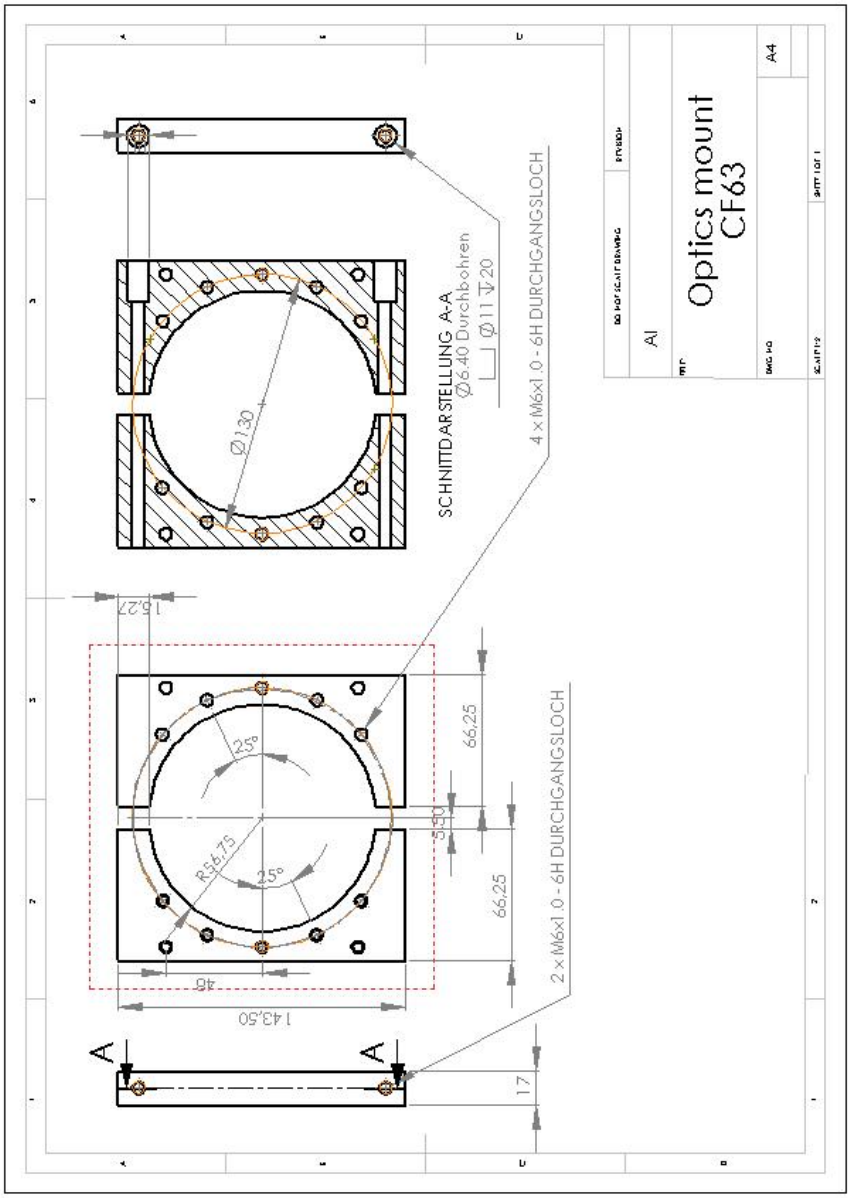

Figure C.3: Drawing of the optics mount for CF63 windows.

Bibliography

[And94] Brian P. Anderson, Mark A. Kasevich. “Enhanced loading of a magneto-optical trap from an atomic beam”. *Phys. Rev. A* 50(5):R3581–R3584, November 1994

[Ash70] A. Ashkin. “Acceleration and trapping of particles by radiation pressure”. *Phys. Rev. Lett.* 24(4):156–159, January 1970

[Bla01] Eric D. Black. “An introduction to Pound-Drever-Hall laser frequency stabilization”. *Am. J. Phys.* 69(1):79–87, January 2001

[Boe96] A. C. Fey den Boer. “Optical injection and feedback in broad-area didoe lasers”. Technical report, TU Eindhoven, 1996

[Boe97] A. C. Fey den Boer, H. C. W. Beijerinck, K. A. H. van Leeuwen. “High-power broad-area diode lasers for laser cooling”. *Appl. Phys. B* 64:415–417, 1997

[Bra96] Igor Bray, Dmitry V. Fursa. “Convergent Close-Coupling Method: A "Complete Scattering Theory"?” *Phys. Rev. Lett.* 76(15):2674, April 1996

[Bra97] C. C. Bradley, C. A. Sackett, R. G. Hulet. “Bose-Einstein Condensation of Lithium: Observation of Limited Condensate Number”. *Phys. Rev. Lett.* 79(6):985–989, February 1997

[Bra02] Igor Bray. “Close-Coupling Approach to Coulomb Three-Body Problems”. *Phys. Rev. Lett.* 89(27):273201, December 2002

[Bre03] R. Bredy, H. Nguyen, H. Camp, X . Fléchard, B.D. DePaola. “MOTRIMS as a generalized probe of AMO processes”. *Nucl. Instr. and Meth. in Phys. Res. B* 205:191–195, 2003

[Cam05] Gretchen K. Campbell, Aaron E. Leanhardt, Jongchul Mun, Micah Boyd, Erik W. Streed, Wolfgang Ketterle, David E. Pritchard. “Photon Recoil Momentum in Dispersive Media”. *Phys. Rev. Lett.* 94(17):170403, May 2005

[Chu85] S. Chu, L. Hollberg, J. E. Bjorkholm, A. Cable, A. Ashkin. “Three-Dimensional Viscous Confinement and Cooling of Atoms by Resonance Radiation Pressure”. *Phys. Rev. Lett.* 55(1):48–51, July 1985

[Chu98] Steven Chu. "The manipulation of neutral particles". *Rev. Mod. Phys.* 70(3):685–706, July 1998

[Col01a] J. Colgan, M. S. Pindzola, D. M. Mitnik, D. C. Griffin. "Total integral and ejected-energy differential cross sections for the electron-impact ionization of lithium". *Phys. Rev. A* 63:062709, 2001

[Col01b] J. Colgan, M. S. Pindzola, D. M. Mitnik, D. C. Griffin, I. Bray. "Benchmark Nonperturbative Calculations for the Electron-Impact Ionization of Li(2s) and Li(2p)". *Phys. Rev. Lett.* 87(21):213201, November 2001

[Con00] R. S. Conroy, A. Carleton, A. Carruthers, B. D. Sinclair, C. F. Rae, K. Dholakia. "A visible extended cavity diode laser for the undergraduate laboratory". *Am. J. Phys.* 68(10):925–931, October 2000

[Coo99] John W. Cooper. "Asymptotic ratios of single, double and triple photoionization for lithium at high energies". *Phys. Rev. A* 59(6):4825–4828, June 1999

[CT98] Claude N. Cohen-Tannoudji. "Manipulating atoms with photons". *Rev. Mod. Phys.* 70(3):707–719, July 1998

[Ded01] C. J. Dedman, K. G. H. Baldwin, M. Colla. "Fast switching of magnetic fields in a magneto-optic trap". *Rev. Sci. Instrum.* 72(11):4055–4058, November 2001

[Dem81] Wolfgang Demtröder. Laser Spectroscopy. Springer-Verlag, 3rd edition, 1981

[Dem96] Wolfgang Demtröder. Experimentalphysik 3. Springer-Verlag, 2nd edition, 1996

[DeM99] B. DeMarco, H. Rohner, D. S. Jin. "An enriched ^{40}K source for fermionic atom studies". *Rev. Sci. Instrum.* 70(4):1967–1969, April 1999

[Dha96] A. N. Dharamsi. "A theory of modulation spectroscopy with applications of higher harmonic detection". *J. Phys. D: Appl. Phys.* 29:540–549, 1996

[Die98] K. Dieckmann, R. J. C. Spreeuw, M. Weidemüller, J. T. M. Walraven. "Two-dimensional magneto-optical trap as a source of slow atoms". *Phys. Rev. A* 58(5):3891–3895, November 1998

[Dor01a] A. Dorn, A. Kheifets, C. D. Schröter, B. Najjari, C. Höhr, R. Moshammer, J. Ullrich. "Double Ionization of Helium by Electron-Impact: Complete Pictures of the Four-Body Breakup Dynamics". *Phys. Rev. Lett.* 86(17):3755–3758, April 2001

[Dör01b] R. Dörner, H. Giessen, R. Moshammer, H. Rottke. "Wenn Licht Atome in Stücke reißt." *Phys. Blätt.* 57(4):49–52, 2001

[Emm04] Agapi Emmanouilidou, Jan M. Rost. "Triple photoionizayion of Lithium near theshold". *submitted* September 2004

[Eng97] Hans Engler. "Aufbau eines Zeeman-Abbremsers und Inbetriebnahme einer magnetooptischen Falle für Lithium-Atome". Master's thesis, Ruprecht-Karls-Universität Heidelberg, 1997

[Fis02] D. Fischer, B. Feuerstein, R. D. DuBois, R. Moshammer, J. R. Crespo Lopez-Urrutia, I. Draganic, H. Lörch, A. N. Perumal, J. Ullrich. "State Resolved Measurement of Single Electron Capture in Slow Ne^{7+} and Ne^{8+} - Helium Collisions". *J. Phys. B* 35:1369, 2002

[Fle01] X. Flechard, H. Nguyen, E. Wells, I. Ben-Itzhak, B. D. DePaola. "Kinematically Complete Charge Exchange Experiment in the $Cs^+ + Rb$ Collision System Using a MOT Target". *Phys. Rev. Lett.* 87(12):123203, September 2001

[Fle02] C. S. Fletcher, J. E. Lye, N. P. Robins, J. D. Close. "A Self-Locked Magneto Optic Trap". *Preprint* March 2002

[For98] C. Fort, A. Bambini, L. Cacciapuoti, F. S. Cataliotti, M. Prevedelli, G. M. Tino, M. Inguscio. "Cooling mechanisms in potassium magneto-optical traps". *Eur. Phys. J. D* 3:113–118, 1998

[Fri99] Tobias Fritz. "Setup of a Magneto-Optical Trap for Lithium as a Part of a Combined Na-Li MOT". Master's thesis, Technische Universität Graz, February 1999

[Ger98] V. P. Gerginov, Y. V. Dancheva, M. A. Taslakov, S. S. Cartaleva. "Frequency tunable monomode diode laser at 670 nm for high resolution spectroscopy". *Opt. Commun.* 149:162–169, April 1998

[Ger99] M. Gertsvolf, M. Rosenbluh. "Injection locking of a diode laser locked to a Zeeman frequency stabilized laser oscillator". *Opt. Commun.* 170:269–274, November 1999

[Ger01] V. Gerginov, B. Laughman, D. DiBerardino, R. J. Rafac, S. T. Ruggiero, C. E. Tanner. "Diode lasers for fast-beam laser experiments". *Opt. Commun.* 187:219–230, January 2001

[Gol88] L. Goldberg, M. K. Chun. "Injection locking characteristics of a 1 W broad stripe laser diode". *Appl. Phys. Lett.* 53(20):1900–1902, November 1988

[Gon05] Antonio Javier González Martínez. "Quantum interference in the dielectronic recombination of heavy highly charged ions". Ph.D. thesis, Ruperto-Carola-University, Heidelberg, 2005

[Gri00] R. Grimm, M. Weidemüller, Y. B. Ovchinnikov. "Optical Dipole Traps for Neutral Atoms". *Adv. At. Mol. Opt. Phys.* 42(95), 2000

[Gro00] Particle Data Group. "Particle Physics Booklet". Springer, 2000

[Gwi02] Gerald Gwinner. Experimentelle Methoden der Atomphysik. Vorlesung an der Universität Heidelberg. Max-Planck-Institut für Kernphysik, Heidelberg, 2001/2002

[Hän75] T. W. Hänsch, A. L. Schawlow. "Cooling of gases by laser radiation". *Opt. Comm.* 13:68, 1975

[Har98] H. W. van der Hart, C. H. Greene. "Double and Triple Photoionization of Ground-State Lithium". *Phys. Rev. Lett.* 81(20):4333–4336, November 1998

[Har03] Margaret Lynn Harris. "Design and Construction of an Improved Zeeman Slower". Master's thesis, Trinity College, Duke University, 2003

[Haw01] C. J. Hawthorn, K. P. Weber, R. E. Scholten. "Littrow configuration tunable external cavity diode laser with fixed direction output beam". *Rev. Sci. Instrum.* 72(12):4477–4479, December 2001

[Hof96] T. Hof, D. Fick, H. J. Jänsch. "Application of diode lasers as a spectroscopic tool at 670 nm". *Opt. Commun.* 124:283–286, March 1996

[Hof01] Sebastian Hofferberth. "Construction of a tunable and stabilized 640 nm Diode Laser System". Technical report, TU Eindhoven, November 2001

[Hoo94] M. D. Hoogerland, H. F. P. de Bie, H. C. W. Beijerinck, K. A. H. van Leeuwen, P. van der Straten, E. J. D. Vredenbregt, H. J. Metcalf. "Force and Diffusion Measurements in Sub-Doppler Laser Cooling". *Phys. Rev. Lett.* 72(21):3332–3335, May 1994

[Hua99] M.-T. Huang, R. Wehlitz, Y. Azuma, L. Pibida, I. A. Sellin, J. W. Cooper, M. Koide, H. Ishijima, T. Nagata. "Single and double photoionization of lithium". *Phys. Rev. A* 59(5):3397–3401, May 1999

[Hua02] M.-T. Huang, L. Zhang, S. Hasegawa, S. H. Southworth, L. Young. "Measurements of the electron-impact double-to-single ionization ratio using trapped lithium". *Phys. Rev. A* 66:012715, 2002

[Hua03] M.-T. Huang, W. W. Wong, M. Inokuti, S.H. Southworth, L. Young. "Triple Ionization of Lithium by Electron Impact". *Phys. Rev. Lett.* 90(16):163201, April 2003

[Hum79] J. Humlíček. "An efficient method for evaluation of the complex probability function: The Voigt function and its derivatives". *J. Quant. Spectrosc. Radiat. Transfer* 21:309–313, 1979

[Jia02] Xiang-Fu Jia. "Structure in differential cross sections for electron-impact ionization of $Li^+(1s^2)$ in the coplanar equal-energy-sharing geometry". *Phys. Rev. A* 66:062708, 2002

[Kad03] A. S. Kadyrov, A. M. Mukhamedzhanov, A. T. Stelbovics, I. Bray. "Integral Representation for the Electron-Atom Ionization Amplitude which is Free of Ambiguity and Divergence Problems". *Phys. Rev. Lett.* 91(25):253202, December 2003

[Ket92] W. Ketterle, A. Martin, M. A. Joffe, D. E. Pritchard. "Slowing and Cooling of Atoms in Isotropic Laser Light". *Phys. Rev. Lett.* 69(17):2483–2486, October 1992

[Ket93] W. Ketterle, K. B. Davis, M. A. Joffe, A. Martin, D. E. Pritchard. "High Densities of Cold Atoms in a Dark Spontaneous-Force Optical Trap". *Phys. Rev. Lett.* 70(15):2253–2256, April 1993

[Kno03] S. Knoop, J. W. Turkstra, R. Morgenstern, R. E. Olson, R. Hoekstra. "Multi-electron processes in slow He^{2+}-Na collisions measured with MOTRIMS". *Nucl. Instr. and Meth. in Phys. Res. B* 205:560–567, 2003

[Kol97] H. Kollmus, W. Schmitt, R. Moshammer, M. Unverzagt, J. Ullrich. "A high resolution 4π multi-electron spectrometer for soft electrons". *Nucl. Instr. and Meth. in Phys. Res. B* 124:377–380, 1997

[Kra01] Stephan Kraft. "Sympathetische Kühlung in einem Gemisch aus ultrakaltem Lithium und Cäsium". Master's thesis, Ruprecht-Karls-Universität Heidelberg, 2001

[Kro02] Sven Kroboth. "Laserkühlung von Ytterbiumatomen". Master's thesis, Universität Stuttgart, October 2002

[Lan84] L. D. Landau, E. M. Lifschitz. Electrodynamics of Continuous Media. Course of Theoretical Physics. Oxford University Press, 2 edition, 1984

[Let88] P. D. Lett, R. N. Watts, C. I. Westbrook, W. D. Phillips, P. L. Gould, H. J. Metcalf. "Observation of Atoms Laser Cooled below the Doppler Limit". *Phys. Rev. Lett.* 61(2):169–172, July 1988

[Lu01] W. Lu, M. D. Hoogerland, D. Milic, K. G. H. Baldwin, S. J. Buckman. "A bright metastable atom source at 80 K". *Rev. Sci. Instrum.* 72(6):2558–2561, June 2001

[Mal97] A. W. Malcherek, J. M. Rost, J. S. Briggs. "Complete photofragmentation of the lithium atom". *Phys. Rev. A* 55(6):3979–3982, June 1997

[McA96] W. I. McAlexander, E. R. I. Abraham, R. G. Hulet. "Radiative lifetime of the ^{2}P state of lithium". *Phys. Rev. A* 54(1):5–8, July 1996

[Mer00] M. Merimaa, H. Talvitie, P. Laakkonen, M. Kuittinen, I. Tittonen, E. Ikonen. "Compact external-cavity diode laser with a novel transmission geometry". *Opt. Comm.* 174:175–180, January 2000

[Mer01] M. Merimaa, P. Kokkonen, K. Nyholm, E. Ikonen. "Portable laser frequency standard at 633 nm with compact external-cavity diode laser". *Metrologia* 38:311–318, 2001

[Met94] H. J. Metcalf, P. van der Straten. "Cooling and trapping of neutral atoms". *Phys. Rep.* 244(4-5):203–286, August 1994

[Met99] H. J. Metcalf, P. van der Straten. Laser Cooling and Trapping. Springer-Verlag, 1999

[Mew99] M. O. Mewes, G. Ferrari, F. Schreck, A. Sinatra, C. Salomon. "Simultaneous magneto-optical trapping of two lithium isotopes". *Phys. Rev. A* 61:011403, 1999

[Mil97] D. Milic, W. Lu, M. D. Hoogerland, M. Blacksell, K. G. H. Baldwin, S. J. Buckman. "Improved spectral properties of diode lasers". *Rev. Sci. Instrum.* 68(10):3657–3659, October 1997

[Mil01] D. Milic, M. D. Hoogerland, K. G. H. Baldwin, S. J. Buckman. "Mirror design for two-dimensional magneto-optic lenses and compressors". *Appl. Opt.* 40(12):1907–1910, April 2001

[MK97] Theo Mayer-Kuckuk. Atomphysik: eine Einfuehrung. Teubner Studienbücher : Physik. Teubner, Stuttgart, 5th edition, 1997

[Mol97] P. A. Molenaar, P. van der Straten, H. G. M. Heideman, H. J. Metcalf. "Diagnostic technique for Zeeman-compensated atomic beam slowing: Technique and result". *Phys. Rev. A* 55(1):605–614, January 1997

[Mon90] C. Monroe, W. Swann, H. Robinson, C. Wieman. "Very Cold Trapped Atoms in a Vapor Cell". *Phys. Rev. Lett.* 65(13):1571–1574, September 1990

[Mos94] R. Moshammer, J. Ullrich, M. Unverzagt, W. Schmidt, P. Jardin, R. E. Olson, R. Mann, R. Dörner, V. Mergel, U. Buck, H. Schmidt-Böcking. "Low-Energy Electrons and Their Dynamical Correlation with Recoil Ions for Single Ionization of Helium by Fast, Heavy-Ion Impact". *Phys. Rev. Lett.* 73(25):3371–3374, December 1994

[Mos96] R. Moshammer, M. Unverzagt, W. Schmitt, J. Ullrich, H. Schmidt-Böcking. "A 4π recoil-ion electron momentum analyzer: a high-resolution "microscope" for the investigation of the dynamics of atomic, molecular and nuclear reactions". *Nucl. Instr. and Meth. in Phys. Res. B* 108:425–445, 1996

[Nav05] Carl Nave. HyperPhysics. Department of Physics and Astronomy, Georgia State University, Atlanta, http://hyperphysics.phy-astr.gsu.edu/hbase/hph.html, 2005

[Nes63] A. N. Nesmeyanov. Vapor Pressure of the Chemical Elements. Elsevier Publishing Company, National Bureau of Standards, Washington D.C., 1963

[Ngu04] H. Nguyen, X. Fléchard, R. Brédy, H. A. Camp, B. D. DePaola. "Recoil ion momentum spectroscopy using magneto-optically trapped atoms". *Rev. Sci. Instum.* 75(8):2638–2647, August 2004

[Orl04] D. A. Orlov, U. Weigel, D. Schwalm, A. S. Terekhov, A. Wolf. "Ultra-cold electron source with a GaAs-photocathode". *Nucl. Instr. and Meth. in Phys. Res. A* 532:418–421, 2004

[Phi82] William D. Phillips, Harold Metcalf. "Laser Deceleration of an Atomic Beam". *Phys. Rev. Lett.* 48(9):596–599, March 1982

[Phi98] William D. Phillips. "Laser cooling and trapping of neutral atoms". *Rev. Mod. Phys.* 70(3):721, July 1998

[Phi01] D. F. Phillips, A. Fleischhauer, A. Mair, R. L. Walsworth, M. D. Lukin. "Storage of Light in Atomic Vapor". *Phys. Rev. Lett.* 86(5):783–786, January 2001

[Poe01] M. van der Poel, C. V. Nielsen, M.-A. Gearba, N. Andersen. "Fraunhofer Diffraction of Atomic Matter Waves: Electron Transfer Studies with a Laser Cooled Target". *Phys. Rev. Lett.* 87(12):123201, Seotember 2001

[Pra98] M. Praeger, V. Vuletic, T. Fischer, T. W. Hänsch, C. Zimmermann. "A broad emitter diode laser system for lithium spectroscopy". *Appl. Phys.B* 67:163–166, 1998

[Pro85] J. Prodan, A. Migdall, W. D. Phillips, I. So, H. J. Metcalf, J. Dalibard. "Stopping Atoms with Laser Light". *Phys. Rev. Lett.* 54(10):992–995, March 1985

[Qu98] L. Qu, Z. Wang, B. Li. "Theory of oscillator strength of the lithium isoelectronic sequence". *J. Phys. B: At. Mol. Opt. Phys.* 31:3601–3607, 1998

[Raa87] E. L. Raab, M. Prentiss, Alex Cable, Steven Chu, D. E. Pritchard. "Trapping of Neutral Sodium Atoms with Radiation Pressure". *Phys. Rev. Lett.* 59(23):2631–2634, December 1987

[Rad95] L. J. Radziemski, R. Engleman, J. W. Brault. "Fourier-transform-spectroscopy measurements in the spectra of neutral lithium, ^{6}Li I and ^{7}Li I (Li I)". *Phys. Rev. A* 52(6):4462–4470, December 1995

[Ram56] Norman F. Ramsey. Molecular Beams. Oxford University Press, 1956

[Ran03] J. Rangama, D. Hennecart, N. Stolterfoht, J. A. Tanis, B. Sulik, F. Frémont, X. Husson, J.-Y. Chesnel. "Identification and characterization of the dielectric process in the formation of two K-shell vacancies in atomic Li by fast electron impact". *Phys. Rev. A* 68:040701, 2003

[Res99] T. N. Rescigno, M. Baertschy, W. A. Isaacs, C. W. McCurdy. "Collisional Breakup in a Quantum System of Three Charged Particles". *Science* 286(5449):2474–2479, December 1999

[Ric95] L. Ricci, M. Weidemüller, T. Esslinger, A. Hemmerich, C. Zimmermann, V. Vuletic, W. König, T. W. Hänsch. "A compact grating-stabilized diode laser system for atomic physics". *Opt. Commun.* 117:541–549, June 1995

[Rii90] E. Riis, D. S. Weiss, K. A. Moler, S. Chu. "Atom Funnel for the Production of a Slow and High-Density Atomic Beam". *Phys. Rev. Lett.* 64(14):1658–1661, April 1990

[Rit95] N. W. M. Ritchie, E. R. I. Abraham, Y. Y. Xiao, C. C. Bradley, R. G. Hulet, P. S. Julienne. "Trap-loss collisions of ultracold lithium atoms". *Phys. Rev. A* 51(2):890–893, February 1995

[Sam90] James A. Samson. "Proportionality of Electron-Impact Ionization to Double Photoionization". *Phys. Rev. Lett.* 65(23):2861–2864, December 1990

[San95] C. J. Sansonetti, B. Richou, R. Engleman, L. J. Radziemski. "Measurements of the resonance lines of ^{6}Li and ^{7}Li by Doppler-free frequency-modulation spectroscopy". *Phys. Rev. A* 52(4):2682–2688, October 1995

[Sav98] Thomas Alan Savard. "Raman Induced Resonance Imaging of Trapped Atoms". Ph.D. thesis, Trinity College, Duke University, 1998

[Sch94] Ulrich Schünemann. "Ein Diodenlasersystem für das lasergekühlte Lithiumtarget am Heidelberger TSR". Master's thesis, Ruprecht-Karls-Universität Heidelberg, 1994

[Sch96] U. Schünemann, I. Manek, R. Grimm, D. Habs, D. Schwalm. "Laser-cooled and trapped atoms as a precision target for heavy ion beams". *Hyp. Int.* 99(127-133), 1996

[Sch97] Ulrich Schünemann. "Magnetooptischer Einfang von Lithiumatomen mit Halbleiterlasern". Ph.D. thesis, Ruprecht-Karls-Universität Heidelberg, 1997

[Sch98] U. Schünemann, H. Engler, M. Zielonkowski, M. Weidemüller, R. Grimm. "Magneto-optic trapping of lithium using semiconductor lasers". *Opt. Comm.* 158:263–272, December 1998

[Sch99] R. Schumann, C. Schubert, U. Eichmann, R. Jung, G. von Oppen. "Laser cooling of metastable He atoms in an inhomogeneous electric field". *Phys. Rev. A* 59(3):2120–2125, March 1999

[Sch00] M. Schulz, R. Moshammer, W. Schmitt, H. Kollmus, R. Mann, S. Hagmann, R. E. Olson, J. Ullrich. "Correlated three-electron continuum states in triple ionization by fast heavy-ion impact". *Phys. Rev. A* 61(2):022703, February 2000

[Sch02] S. Schippers, S. Kieslich, A. Müller, G. Gwinner, M. Schnell, A. Wolf, A. Covington, M. E. Bannister, L.-B. Zhao. "Interference effects in the photorecombination of argonlike Sc^{3+} ions: Storage-ring experiment and theory". *Phys. Rev. A* 65(042723):1–10, April 2002

[Sch03a] Ulrike Schlöder. "Heteronukleare Photoassoziation in einem kalten ^{6}Li/^{7}Li-Gemisch". Ph.D. thesis, Eberhard-Karls-Universität Tübingen, 2003

[Sch03b] M. Schulz, R. Moshammer, D. Fischer, H. Kollmus, D. H. Madison, S. Jones, J. Ullrich. "Three-dimensional imaging of atomic four-body processes". *Nature* 422:48–50, March 2003

[Sco88] Giacinto Scoles, editor. Atomic and Molecular Beam Methods, volume I. Oxford University Press, New York, 1988

[Sha90] S.-Q. Shang, B. Sheehy, P. van der Straten, H. J. Metcalf. "Velocity-Selective Magnetic-Resonance Laser Cooling". *Phys. Rev. Lett.* 65(3):317–320, July 1990

[Shv00] I. Shvarchuck, K. Dieckmann, M. Zielonkowski, J. T. M. Walraven. "Broad-area diode-laser system for a rubidium Bose-Einstein condensation experiment". *Appl. Phys. B* 71:475–480, August 2000

[Sla71] V. J. Slabinski, R. L. Smith. "Lithium Vapor Cell and Discharge Lamp Using MgO Windows". *Rev. Sci. Instrum.* 42(9):1334–1338, September 1971

[Spi05] F. M. Spiegelhalder, J. Steinmann, A. Dorn, J. Ullrich. "A Lithium MOT Combined with a Reaction Microscope". J. Ullrich, J. M. Rost, editors, "26. Arbeitsbericht Energiereiche Atomare Stösse", MPIKS Dresden, 2005

[Tem02] J. G. C. Tempelaars, R. J. W. Stas, P. G. M. Sebel, H. C. W. Beijerinck, E. J. D. Vredenbregt. "An intense and slow and cold beam of metastable Ne(3s) $^3P_2$ atoms". *Eur. Phys. J. D* 18:113–121, 2002

[Top02] Toptica. DL 100 Diode Laser System Manual. Toptica Photonics AG, Martinsried, August 2002

[Tur01] J. W. Turkstra, R. Hoekstra, S. Knoop, D. Meyer, R. Morgenstern, R. E. Olson. "Recoil Momentum Spectroscopy of Highly Charged Ion Collisions on Magneto-Optically Trapped Na". *Phys. Rev. Lett.* 87(12):123202, September 2001

[Tur02] L. D. Turner, K. P. Weber, C. J. Hawthorn, R. E. Scholten. "Frequency noise characterisation of narrow linewidth diode lasers". *Opt. Commun.* 201:391–397, January 2002

[Ull97] J. Ullrich, R. Moshammer, R. Dörner, O. Jagutzki, V. Mergel, H. Schmidt-Böcking, L. Spielberger. "Recoil-ion momentum spectroscopy". *J. Phys. B* 30:2917–2974, 1997

[Ull03] J. Ullrich, V. P. Shevelko. Many-Particle Quantum Dynamics in Atomic and Molecular Fragmentation. Springer, 2003

[Vál77] L. Vályi. Atom and Ion Sources. Wiley, New York, 1977

[Vre03] E. J. D. Vredenbregt, K. A. H. van Leeuwen. "Laser cooling and trapping visualized". *Am. J. Phys.* 71(8):760–765, August 2003

[Weh98] R. Wehlitz, M.-T. Huang, B. D. DePaola, J. C. Levin, I. A. Sellin, T. Nagata, J. W. Cooper, Y. Azuma. "Triple Photoionization of Lithium". *Phys. Rev. Lett.* 81(9):1813–1816, August 1998

[Weh99] C. T. Wehlan. "Fragmentation Processes in Atomic Collisions". *Science* 286(5449):2457, December 1999

[Weh00] R. Wehlitz, T. Pattard, M.-T. Huang, I.A. Sellin, J. Burgdörfer, Y. Azuma. "Near-threshold triple-photoionization cross section of lithium". *Phys. Rev. A* 61:030704, February 2000

[Wie91] C. E. Wieman, L. Hollberg. "Using diode lasers for atomic physics". *Rev. Sci. Instrum.* 62(1):1–20, January 1991

[Wil55] W. C. Wiley, I. H. McLaren. "Time-of-Flight Mass Spectrometer with Improved Resolution". *Rev. Sci. Instrum.* 26(12):1150–1157, December 1955

[Win75] D. J. Wineland, H. Dehmelt. "Proposed 10^{14} $\Delta\nu < \nu$ laser fluorescence spectroscopy on TI^{+} mono-ion oscillator III". *Bull. Am. Phys. Soc.* 20:637, 1975

[Wol00] Steffen Wolf, Hanspeter Helm. "Ion-recoil momentum spectroscopy in a laser-cooled atomic sample". *Phys. Rev. A* 62(4):043408, October 2000

[Wyn92] R. Wynands, F. Diedrich, D. Meschede, H. R. Telle. "A compact tunable 60-dB Faraday optical isolator for the near infrared". *Rev. Sci. Instrum.* 63(12):5586–5590, December 1992

List of Figures

List of Tables

Acknowledgements

Die erfolgreiche Durchführung einer Diplomarbeit wäre nicht möglich ohne die Zusammenarbeit, Hilfe und Unterstützung Vieler. An dieser Stelle möchte ich allen danken, die mir während meiner Zeit als Diplomand behilflich waren und mich unterstützt haben - vor allem den Mitarbeitern der AG Ullrich. Es herrschte ein sehr angenehmes und freundliches Arbeitsklima in der Gruppe.

An erster Stelle danke ich Prof. Joachim Ullrich für die Aufnahme in die Arbeitsgruppe und besonders für das kritische Korrekturlesen dieser Arbeit.

Meinem Betreuer, Alexander Dorn, danke ich für viele erfolgreiche und lehrreiche Stunden im Labor, dafür dass er mich weitestgehend selbstständig hat arbeiten lassen und für seine genialen praktischen Lösungen und Ideen, die oft viel Arbeit und Zeit gespart haben, sowie für interessante Diskussionen und Denkanstösse. Nicht zuletzt danke ich ihm für das Korrekturlesen dieser Arbeit.

Ganz besonderer Dank gebührt Sascha Reinhardt, der uns seinen Farbstofflaser zur Verfügung gestellt hat und Stunden damit verbrachte, diesen für unsere Bedürfnisse umzubauen und zu justieren. Ohne seine Hilfe wäre diese Arbeit zu keinem befriedigenden Ergebnis gekommen. An dieser Stelle danke ich auch Helga Krieger für die freundliche Unterstützung in allen Laserangelegenheiten - insbesondere für ihr großes Engagement bei der Inbetriebnahme des Farbstofflasers.

Claus-Dieter Schröter danke ich für seine stete Hilfsbereitschaft. Von seiner immensen praktischen Erfahrung habe ich viel profitieren können. Außerdem danke ich Jochen Steinmann, der als Doktorand am Lithium-MOT Reaktionsmikroskop arbeitet.

Den technischen Mitarbeitern des MPI-K, ohne deren Hilfe und Erfahrung der Aufbau eines Experiments wohl unmöglich wäre, danke ich für die rasche Ausführung der Arbeiten. Insbesondere möchte ich mich bei den Mitarbeitern von der Elektronikwerkstatt und der feinmechanischen Werkstatt sowie von den Ausbildungswerkstätten bedanken, die immer hilfsbereit waren und wichtige Ratschläge geben konnten.

Me gustaría agradecer especialmente a mi compañera de oficina Rosario Soria Orts por su apoyo moral, traducciones al español, la ayuda durante la escritura de esta tesis y por esos deliciosos cafés. He pasado buenos ratos trabajando a tú lado además de comerme tus Gummibärchen. Te deseo buena suerte en la etapa final de tu tesis!

Espero verte de nuevo en la celebración!

Quiero agradecer a Antonio J. González Martínez por haberme ayudado mucho con ORIGIN, especialmente con los ajustes para las funciones de Voigt. Creo que hemos llegado a ser buenos amigos. Disfrute mucho haciendo de camarero contigo en Riezlern y en los cafes despues de la comida. Mucha suerte y exito en el futuro, y espero volver a verte alguna vez en España...

Meinem Freund und Kommilitonen, Daniel Gallego Garcia, der meine Zeit an der Universität Heidelberg wesentlich geprägt hat, danke ich für seine Hilfe bei diversen Übungszetteln, bei der Prüfungsvorbereitung und beim Schreiben dieser Arbeit.

For last corrections I want to thank Mike Froese.

Zuletzt gilt mein Dank vor allem meinen Eltern, ohne deren materielle und moralische Unterstützung während meines gesamten Studiums diese Arbeit wohl nie zustande gekommen wäre.

Erklärung

Ich versichere, daß ich diese Arbeit selbständig verfaßt und keine anderen als die angegebenen Quellen und Hilfsmittel benutzt habe.

Heidelberg, den 28. Juli 2005

Frederik M. Spiegelhalder